Valentin Zauner, BSc

Time Evolution of a Comoving Window:
Simulation of Local Signals on Infinite One-Dimensional Spin Chains

MASTER THESIS

for obtaining the academic degree
Diplom-Ingenieur

Master Programme of
Technical Physics

Graz University of Technology

Supervisor:
Ao.Univ.-Prof. Dr. Hans Gerd Evertz
Institut für Theoretische Physik - Computational Physics, TU Graz

in cooperation with:
Dept. of Physics, Graduate School of Sciences, Kobe University

Graz, October 24, 2011

to Mirjam,
of course!

Abstract

The propagation of local signals on one-dimensional systems has been of long standing interest, even more so over the recent years with the invention of efficient numerical methods based on Matrix Product States. Existing algorithms for infinite systems however cannot simulate the evolution of local signals, whereas finite size algorithms suffer from finite size effects. The present work introduces a method that is able to simulate the propagation of local signals on a system of infinite size by removing finite size effects while still working on a finite system at all times. This finite system, conceptually a part of the infinite system, follows the propagation of a locally induced signal by moving along with its signal front and is thus called a Comoving Window.

The new method has been tested by investigating several types of locally induced signals on infinitely large chains of the XX, XXZ and Transverse Ising spin chain models. These models can also be interpreted as describing interacting spinless fermions. It has been shown that the new method is indeed able to follow signal fronts of locally induced signals and to remove finite size effects, such that the propagation of signal fronts can be studied up to very large simulation times without the distortion by finite size effects.

The computational effort of Matrix Product State simulations is very sensitive to the entanglement entropy present in the system. Around the origin of locally induced signals, entanglement entropy however often grows rapidly, whereas around the signal front it generally grows modestly. By moving along with the signal front and thus moving away from areas with high entanglement entropy – which are not of interest – the computational effort for an accurate simulation is significantly reduced.

Kurzfassung

Die Ausbreitung von lokalen Signalen auf unendlichen, eindimensionalen Systemen ist schon seit langem Gegenstand großen Interesses, speziell seit der Entwicklung leistungsfähiger, auf Matrixproduktzuständen basierender numerischer Methoden. Bestehende Algorithmen für unendliche System sind jedoch nicht in der Lage, die Zeitentwicklung lokaler Signale zu simulieren. Algorithmen für endliche Systeme stehen andererseits vor dem Problem, dass durch die Endlichkeit des Systems Randeffekte auftreten, welche das Signal beeinflussen. Die vorliegende Arbeit stellt nun eine Methode vor, die durch Eliminieren dieser Randeffekte in der Lage ist, die Ausbreitung lokaler Signale auf unendlichen Systemen zu simulieren, während das tatsächlich simulierte System nach wie vor endlich ist. Dieses System endlicher Ausdehnung, konzeptionell ein Ausschnitt des unendlichen Systems, folgt der Ausbreitung eines lokal angeregten Signals, indem es sich mit dessen Signalfront mitbewegt. Wegen dieser Eigenschaft wird es “Comoving Window” oder “Mitbewegtes Fenster” genannt.

Die neue Methode wurde getestet, indem verschiedene Signaltypen auf unendlichen Ketten des XX, XXZ und des Transversalen Ising Spin Modells untersucht wurden. Diese Modelle können auch so interpretiert werden, dass sie wechselwirkende, spinlose Fermionen beschreiben. Es wurde gezeigt, dass die neue Methode in der Tat in der Lage ist, Signalfronten lokal angeregter Signale zu folgen und Randeffekte zu eliminieren. Die Ausbreitung und Entwicklung von Signalfronten kann dadurch ungestört bis zu sehr großen Zeiten untersucht werden.

Der Rechenaufwand für auf Matrixproduktszuständen basierende numerische Methoden ist empfindlich von der im System vorhandenen Verschränkungsentropie abhängig. In der Umgebung des Signalursprungs steigt diese für gewöhnlich sehr stark an, während der Anstieg in der Umgebung der Signalfront in der Regel beschränkt ist. Durch das Mitbewegen rücken Bereiche großer Verschränkungsentropie – die hier nicht von Interesse sind – aus dem Simulationsfenster. Der Rechenaufwand für eine präzise Simulation wird daher entscheidend verringert.

Contents

1. Introduction

Ever since the advent of the age of quantum mechanics and its wondrous and often seemingly strange consequences, many phenomena that could not be understood in classical physics have been explained on a quantum mechanical level. Especially phenomena stemming from strong correlation effects between particles in condensed matter, such as (anti)ferromagnetism or superconductivity, have been understood by means of many body quantum mechanics. Not only low energy or finite temperature properties, but also dynamics of quantum systems have always been of particular interest.

The nature and complexity of many body systems however makes it impossible in most cases to solve the underlying many body Schrödinger equation exactly. A variety of approximations and restricted solutions, both on the analytical and numerical level, have been proposed over the last decades. Many of these approximations, relying on perturbation theory, however cannot describe strongly correlated systems adequately. Numerical methods have helped much in the understanding of these systems, among them are e.g. Exact Diagonalization methods, Quantum Monte Carlo methods, Series Expansions or Coupled Cluster methods. Many of these methods however are severely limited by systems sizes as their computational increases very quickly with system size.

One numerical method, that has had enormous success in the description of one-dimensional, strongly correlated quantum systems is the Density Matrix Renormalization Group (DMRG) [1] and derivatives thereof. In particular, it has been extended to allow for studying time evolutions of these systems, with methods such as Time Evolving Block Decimation (TEBD) [2] and time dependent DMRG (tDMRG) [3]. The power of these methods lies in the ability to describe strongly correlated systems of very large sizes with very high accuracy, where other methods fail. This ability is due to the special class of quantum states being used in the DMRG framework, known as Matrix Product States (MPS) [4] and the entanglement structure of one-dimensional systems.

In recent years it has become possible to realize strongly correlated quantum systems also experimentally as ultra cold atomic gases in optical lattices [5]. These systems show extraordinarily long coherence times and – due to the experimental design – a complete absence of crystal impurities and undesired interactions, thus enabling an almost dissipationless study of quantum systems and the investigation of many theoretical models and their properties on an experimental level. Careful experimental design even make systematic external manipulations of individual particles by external fields possible. The success of experimental realizations of such systems (cf. e.g. [6]) not only enables a better understanding of the foundations of nature, but also gives rise to many practical applications in quantum computing, data storage, cryptography, communications, etc.

Of particular interest is the emergence of quasi particles as elementary excitations of the many body system, such as spin excitations in spin-spin interaction systems, their properties and especially their evolution over time. For example spin excitations as quasi particles can propagate as spin waves, their dispersions and propagation properties strongly depending on the underlying system. A promising application exploiting propagation properties of spin waves is the field of Spintronics (cf. e.g. [7]).

When investigating the propagation of quasi particles as signals, one is usually interested in the bulk properties of this propagation, thus describing the signal on a system in the thermodynamic limit. Despite the fact that time evolution in the MPS framework is able to efficiently simulate very large systems, finite size effects are always present when simulating systems of finite size. Existing MPS methods for the thermodynamic limit however do not allow for local signals, which would break the required translational invariance. On the following pages, an adaption to the MPS time evolution framework is introduced that is able to simulate the propagation of local spin signals on infinitely large systems, thus removing finite size effects. The actual simulation is performed on a finite system, which is conceptually a part of the underlying infinite system. This finite system moves along with the signal's propagation front and the method will thus be called the Comoving Window (CMW) method.

Chapter 2 gives a short overview of the spin chain models that have been investigated, their properties and (if possible) their solutions and time evolutions. In Chapters 3 and 4 the underlying MPS framework and MPS methods for time evolution and ground state search both for finite systems and the thermodynamic limit are explained. In Chapter 5 the CMW method as an extension to ordinary MPS time evolution is introduced. Chapter 6 then shows application results of the CMW method and the investigation of the properties of various signal types at large times on spin chain models is explained in Chapter 2. A summary, conclusion and outlook can be found in Chapter 7.

2. Quantum Spin Chain Models

The Quantum Models that have been investigated are all special cases of the general one-dimensional L-site spin-$\frac{1}{2}$ XYZ chain with nearest neighbor interactions and an external magnetic field, described by the general Hamiltonian

$$\hat{H}_{XYZ} = -\sum_{j=1}^{L-a} J^x \hat{S}^x_j \hat{S}^x_{j+1} + J^y \hat{S}^y_j \hat{S}^y_{j+1} + J^z \hat{S}^z_j \hat{S}^z_{j+1} - \sum_{j=1}^{L} \mathbf{h} \cdot \hat{\mathbf{S}}_j, \tag{2.1}$$

where J^x, J^y and J^z control the spin-spin interaction strengths, $\mathbf{h} = (h^x, h^y, h^z)$ is the magnetic field strength along the three spatial dimensions and $\hat{\mathbf{S}}_j = (\hat{S}^x_j, \hat{S}^y_j, \hat{S}^z_j)$ is the vector of spin operators at site j. In general, all six parameters can be position dependent as well.

For open boundary conditions (obc) $a = 1$, for periodic boundary conditions (pbc) $a = 0$ and $L + 1 \equiv 1$.

2.1. The Jordan-Wigner Transformation to Interacting Fermions

One-dimensional spin models can be mapped onto systems of spinless fermions by means of the Jordan-Wigner (JW) transformation [8]. In the particle picture one can interpret a site in spin up state as a particle sitting on this site, if in spin down state, there is no particle at this site. A straight forward mapping then would be to interpret the spin ladder operators $\hat{S}^+_j$ and $\hat{S}^-_j$ as particle creation and annihilation operators at site j. While they fulfill the fermionic anticommutator rules on the same site, they do not on different sites, where they in fact fulfill bosonic commutator rules. Therefore they neither describe fermions nor bosons. This can be fixed by introducing a preceding phase factor for the ladder operators, yielding the JW transformation

$$\begin{aligned} c^\dagger_j &= e^{-i\pi \sum_{n<j} \hat{S}^+_n \hat{S}^-_n} \hat{S}^+_j = \prod_{n<j} \left(-2\hat{S}^z_n\right) \hat{S}^+_j \\ c_j &= e^{i\pi \sum_{n<j} \hat{S}^+_n \hat{S}^-_n} \hat{S}^-_j = \prod_{n<j} \left(-2\hat{S}^z_n\right) \hat{S}^-_j . \end{aligned} \tag{2.2}$$

The preceding product of $\hat{S}^z$ operators effectively counts the number N of particles left of site j and yields a sign $(-1)^N$. By introducing this sign, the JW creation and annihilation operators $c^\dagger_j$ and c_j now fulfill the fermionic anticommutator rules

$$\left\{c_i, c^\dagger_j\right\} = \delta_{ij} \qquad \left\{c_i, c_j\right\} = 0 \qquad \left\{c^\dagger_i, c^\dagger_j\right\} = 0. \tag{2.3}$$

and can be interpreted as describing interacting spinless fermions.

Exploiting the properties of spin operators, one can derive the following useful identities

$$\begin{aligned} &\hat{S}^+_j\hat{S}^+_{j+1} = c^\dagger_j c^\dagger_{j+1} \qquad \hat{S}^+_j\hat{S}^-_{j+1} = c^\dagger_j c_{j+1} \qquad \hat{S}^z_j = \hat{n}_j - \frac{1}{2} = c^\dagger_j c_j - \frac{1}{2} \\ &\hat{S}^-_j\hat{S}^+_{j+1} = -c_j c^\dagger_{j+1} \qquad \hat{S}^-_j\hat{S}^-_{j+1} = -c_j c_{j+1}. \end{aligned} \tag{2.4}$$

The inverse transformation then reads

$$\begin{aligned} \hat{S}^+_j &= e^{i\sum_{n<j} c^\dagger_n c_n} c^\dagger_n = \prod_{n<j}\left(1 - 2c^\dagger_n c_n\right) c^\dagger_j \\ \hat{S}^-_j &= e^{-i\sum_{n<j} c^\dagger_n c_n} c_n = \prod_{n<j}\left(1 - 2c^\dagger_n c_n\right) c_j. \end{aligned} \tag{2.5}$$

We will always use $\hbar = 1$, as well as the representation of spin operators $\hat{S}^x_j$, $\hat{S}^y_j$, $\hat{S}^z_j$ and the spin ladder operators $\hat{S}^\pm_j = \hat{S}^x_j \pm i\hat{S}^y_j$ in the z basis, expressed in terms of Pauli matrices $S^\alpha = \frac{1}{2}\sigma^\alpha$, with

$$\sigma^x = \begin{pmatrix} 0 & 1 \\ 1 & 0 \end{pmatrix}, \qquad \sigma^y = \begin{pmatrix} 0 & -i \\ i & 0 \end{pmatrix}, \qquad \sigma^z = \begin{pmatrix} 1 & 0 \\ 0 & -1 \end{pmatrix} \tag{2.6}$$

With the above transformation to interacting spinless fermions, the general XYZ Hamiltonian (2.1) becomes (in the special case $h^x = h^y = 0$)

$$\begin{aligned} \hat{H}_{XYZ} = &- \frac{J^x - J^y}{4}\sum_j c^\dagger_j c^\dagger_{j+1} - c_j c_{j+1} - \frac{J^x + J^y}{4}\sum_j c^\dagger_j c_{j+1} + c^\dagger_{j+1} c_j \\ &- J^z \sum_j \hat{n}_j \hat{n}_{j+1} + (J^z - h^z)\sum_j \hat{n}_j - \frac{L}{4}\left(J^z - 2h^z\right) \end{aligned} \tag{2.7}$$

In the particle picture, this Hamiltonian now describes a system of interacting spinless fermions with a hopping term controlled by the hopping parameter $\frac{J^x+J^y}{4}$ and a particle-particle interaction term controlled by J^z, which can be positive or negative, i.e. the interaction can be attractive or repulsive. We also have a chemical potential $\mu = J^z - h^z$, an energy offset $E_{off} = -\frac{L}{4}\left(J^z - 2h^z\right)$ and a term that changes particle number, controlled by the parameter $\frac{J^x-J^y}{4}$. From this we can immediately see that whenever $J^x = J^y$ the total number of particles is conserved. The above Hamiltonian holds strictly only for obc, for pbc see Section 2.2.

2.2. The XX Model without Magnetic Field: Free Fermions

This model is a special case of the above Hamiltonian with $J^x = J^y = J$ and $J^z = 0$ in the homogeneous case and no external field, i.e. $\mathbf{h} = \mathbf{0}$. This turns (2.1) into

$$\hat{H}_{XX} = -J\sum_j \hat{S}^x_j\hat{S}^x_{j+1} + \hat{S}^y_j\hat{S}^y_{j+1} = -\frac{J}{2}\sum_j \hat{S}^+_j\hat{S}^-_{j+1} + \hat{S}^-_j\hat{S}^+_{j+1}. \tag{2.8}$$

The XX model can be solved exactly very easily by performing a JW transformation and a subsequent Fourier transformation of the JW fermion operators.

Before solving the model, we will look at a few symmetries of the Hamiltonian (2.8). As we have $[\hat{H}_{XX}, \hat{S}^z] = 0$, with $\hat{S}^z = \sum_j \hat{S}^z_j$ the total magnetization in z, there is complete rotational symmetry around the z axis. $\hat{S}^z$ is therefore a constant of motion and its eigenvalues thus good quantum numbers. In the particle picture the total magnetization in z corresponds to the total number operator $\hat{N} = \sum_j \hat{n}_j$ via $\hat{S}^z = \sum_j \left(\hat{n}_j - \frac{1}{2}\right) = \hat{N} - \frac{L}{2}$ using (2.4), which is then also a conserved quantity.

Next consider a system with L even and a rotation by π about the z axis of every other spin. This unitary transformation transforms the spin operators $\hat{S}^{x,y}_{2j} \to -\hat{S}^{x,y}_{2j}$ and effectively $\hat{H}_{XX} \to -\hat{H}_{XX}$ or $\hat{H}_{XX}(J) \to \hat{H}_{XX}(-J)$. On the consequences of this for the time evolution of certain signal types, see Section 6.1.

We will now transform to spinless fermions using a JW transformation. Using the identities (2.4) we get

$$H_{XX} = -\frac{J}{2} \sum_j c^\dagger_j c_{j+1} + c^\dagger_{j+1} c_j + K, \tag{2.9}$$

where for open boundaries $K = 0$. However for periodic boundary conditions $K \neq 0$ stemming from the fact, that

$$\hat{S}^+_L \hat{S}^-_1 = \prod_{n=1}^{L-1} \left(-2\hat{S}^z_n\right) c^\dagger_L c_1 \neq c^\dagger_L c_1 \tag{2.10}$$

$$\hat{S}^-_L \hat{S}^+_1 = -\prod_{n=1}^{L-1} \left(-2\hat{S}^z_n\right) c^\dagger_1 c_L \neq -c_L c^\dagger_1 \tag{2.11}$$

Multiplying both equations by $-2\hat{S}^z_L$ from the left using $2\hat{S}^z \hat{S}^\pm = \pm \hat{S}^\pm$ then gives

$$\hat{S}^+_L \hat{S}^-_1 = -\prod_{n=1}^{L} \left(-2\hat{S}^z_n\right) c^\dagger_L c_1 = (-1)^{N+1} c^\dagger_L c_1 \tag{2.12}$$

$$\hat{S}^-_L \hat{S}^+_1 = -\prod_{n=1}^{L} \left(-2\hat{S}^z_n\right) c^\dagger_1 c_L = (-1)^{N+1} c^\dagger_1 c_L, \tag{2.13}$$

where N is the total number of particles in the system. For the correction factor we then get

$$K = -\frac{J}{2} \left(c^\dagger_L c_1 + c^\dagger_1 c_L\right) \left((-1)^{N+1} - 1\right). \tag{2.14}$$

As we can see it is a constant of motion since the particle number N is conserved and it vanishes if N odd, corresponding to true periodic boundary conditions. However if N even, it takes the value of $J\left(c^\dagger_L c_1 + c^\dagger_1 c_L\right)$. This term then actually changes the sign of the hopping parameter between sites L and 1, which corresponds to antiperiodic boundary conditions, i.e. each particle hopping between sites L and 1 does so with a hopping amplitude of opposite sign. For this case the correction term is however of the order $\mathcal{O}\left(\frac{1}{L}\right)$ and therefore negligible for $L \to \infty$ [9, 10].

By comparing (2.9) with the general Hamiltonian (2.7), we see that only the hopping term controlled by J remains, all other terms vanish. The XX model therefore describes *free* spinless fermions. The fact that total particle number N is conserved is also immediately evident in this form.

2.2.1. Exact Solution

In the following we will solve the problem for periodic boundary conditions and neglect the correction term. A subsequent Fourier transformation of the JW fermion operators

$$c_j = \frac{1}{\sqrt{L}} \sum_k c_k e^{ikj} \qquad c_j^\dagger = \frac{1}{\sqrt{L}} \sum_k c_k^\dagger e^{-ikj}, \tag{2.15}$$

with $k = \frac{2\pi m}{L}$ and $m = -\frac{L}{2}, \dots, \frac{L}{2} - 1$ if L even or $m = -\frac{L-1}{2}, \dots, \frac{L-1}{2}$ if L odd then diagonalizes the Hamiltonian, using

$$\begin{aligned} \sum_j c_j^\dagger c_{j+1} &= \frac{1}{L} \sum_{jkk'} c_k^\dagger c_{k'} e^{-i(k-k')} e^{ik'} = \sum_k c_k^\dagger c_k e^{ik} \\ \sum_j c_{j+1}^\dagger c_j &= \frac{1}{L} \sum_{jkk'} c_k^\dagger c_{k'} e^{-i(k-k')} e^{-ik} = \sum_k c_k^\dagger c_k e^{-ik}, \end{aligned} \tag{2.16}$$

to give

$$\hat{H}_{XX} = -\frac{J}{2} \sum_k c_k^\dagger c_k \left(e^{ik} + e^{-ik}\right) = -J \sum_k \cos(k) c_k^\dagger c_k, \tag{2.17}$$

which is clearly diagonal in k-space. JW fermions with momentum k then follow the dispersion relation $\varepsilon_k = -J\cos(k)$. When examining the model in the canonical ensemble with fixed particle number, the ground state can be derived in each particle number subspace. For the grand canonical ensemble, allowing for all possible particle numbers, we notice that the chemical potential is zero (since $J^z = h^z = 0$) and the ground state can be generated out of the vacuum state, which is the all spin down state

$$|0\rangle := \bigotimes_{j=1}^{L} |{\downarrow}\rangle_j\,, \tag{2.18}$$

by generating particles with momentum $|k| < \frac{\pi}{2}$ for $J > 0$ or $\frac{\pi}{2} < |k|$ for $J < 0$, such that $\varepsilon_k < 0$

$$|\psi_0\rangle = \sum_{|k|<\frac{\pi}{2}} c_k^\dagger |0\rangle\,, \quad J > 0 \tag{2.19}$$

$$|\psi_0\rangle = \sum_{|k|>\frac{\pi}{2}} c_k^\dagger |0\rangle\,, \quad J < 0. \tag{2.20}$$

This corresponds to half filling and a total magnetization of $\langle \hat{S}^z \rangle = 0$. The ground state energy per site is $\frac{E_0}{LJ} = -\frac{1}{L}\sum_{|k|\leq\frac{\pi}{2}} \cos(k) \overset{L\to\infty}{\longrightarrow} -\frac{1}{\pi} \approx -0.31831$ in units of J. The vacuum state itself is also an eigenstate of (2.8) with $E_{vac} = 0$. It is the ground state in the zero particle subspace, since it is the only possible zero particle state.

2.2.2. Time Evolution of a Single Spin Flip

The time evolution of the XX-model can easily be described in the Heisenberg picture in terms of the time dependent JW fermion operators. Inserting into the Heisenberg equation of motion for operators gives for the annihilation operator

$$\frac{\partial}{\partial t} c_k = -i[c_k, \hat{H}_{XX}] = iJ \sum_{k'} \cos(k') \underbrace{[c_k, \hat{n}_{k'}]}_{c_k \delta_{kk'}} = iJ\cos(k) c_k. \tag{2.21}$$

The solution to this differential equation is then

$$c_k(t) = c_k e^{itJ\cos(k)} \qquad\qquad c_k^\dagger(t) = c_k^\dagger e^{-itJ\cos(k)}. \tag{2.22}$$

Next we will calculate the time evolution of an initial state where we have generated one quasi-particle at site l out of the vacuum state, i.e. we have flipped one spin from down to up at site l[1]

$$|\psi_0\rangle_l = c_l^\dagger |0\rangle = \frac{1}{\sqrt{L}} \sum_k c_k^\dagger e^{-ikl} |0\rangle. \tag{2.23}$$

The quasi particles in this case are called magnons, the above state is thus a 1-magnon state. We will now derive its expectation value for the magnetization $\langle \hat{S}_j^z(t) \rangle_l$ and start with

$$\begin{aligned}
\langle \hat{n}_j(t) \rangle_l &= \langle \psi_0|_l \, c_j^\dagger(t) c_j(t) \, |\psi_0\rangle_l \\
&= \frac{1}{N^2} \sum_{mnkq} e^{-itJ[\cos(k)-\cos(q)]} e^{-i(k-q)j} e^{-i(n-m)l} \underbrace{\langle 0| c_m c_k^\dagger c_q c_n^\dagger |0\rangle}_{\delta_{mk}\delta_{qn}} \\
&= \frac{1}{N^2} \sum_{kq} e^{-itJ[\cos(k)-\cos(q)]} e^{-i(k-q)(j-l)} \\
&= \frac{1}{N^2} \left| \sum_k e^{-itJ\cos(k)} e^{-ik(j-l)} \right|^2,
\end{aligned} \tag{2.24}$$

to get

$$\langle \hat{S}_j^z(t) \rangle_l = \frac{1}{N^2} \left| \sum_k e^{-it[J\cos(k)+k(j-l)]} \right|^2 - \frac{1}{2}. \tag{2.25}$$

For further insight see also [11, 12].

---

[1] Notice that in this case $\hat{S}_j^+$ and $c_j^\dagger$ are equivalent, as there are no particles left of site j.

2.3. The Transverse Ising Model (TIM)

The Transverse Ising Model (TIM) is more complex than the XX-model, but still a simple example for a quantum spin model and is often referred to as the Quantum Ising model (QIM) as well. It is an extension of the classical Ising model with spin-spin interactions along one spatial direction, including a magnetic interaction along a transverse spatial direction, hence the name.

The L site homogeneous Transverse Ising spin chain is described by the Hamiltonian

$$\begin{aligned}\hat{H}_{TIM} &= -J\sum_j S_j^x S_{j+1}^x - h\sum_j S_j^z \\ &= -\frac{J}{4}\sum_j \left(\hat{S}_j^+ + \hat{S}_j^-\right)\left(\hat{S}_{j+1}^+ + \hat{S}_{j+1}^-\right) - h\sum_j \hat{S}_j^z. \end{aligned} \tag{2.26}$$

Since $\hat{S}^z$ acts as a spin flip in x, the magnetic field can also be interpreted as a general tunneling amplitude in a 2-level quasi-spin system. In fact, in the early 60s, de Gennes [13] and Blinc [14] used the TIM to model the order-disorder transition in 2 level ferroelectric systems. Also, the pseudo-spin mapping of the BCS Hamiltonian for superconductivity yields an XY model in a transverse field. In its mean field treatment, it then becomes like the TIM and also yields the BCS gap equation [15] (cf. [10]).

In one dimension, it can be solved exactly (see below and e.g. [9, 10, 11, 16]) and shows a zero temperature quantum phase transition at $h_c = \frac{J}{2}$. There the order parameter $\langle \hat{S}_j^x \rangle$ in the ground state for pbc, goes to 0 for $h \to h_c$ from below with a critical exponent of $\beta = \frac{1}{8}$ (cf. e.g. [10]). For $J > 0$ this can e.g. be interpreted as follows: The Ising interaction along x tends to order all the spins ferromagnetically, while the tunneling term tends to destroy this ordering and favor paramagnetic ordering. For $h < h_c$ the Ising interaction is still stronger than the tunneling, so one will observe a finite magnetization along x. For $h \geq h_c$ the tunneling overpowers the ordering tendency of the Ising interaction and the magnetization vanishes for all $h \geq h_c$. The TIM is in fact the simplest quantum model showing a zero temperature quantum phase transition. Because of its simplicity, but still exhibiting interesting features, the TIM has been a toy model in the field of quantum computing, quantum information, entanglement, etc. for many years.

2.3.1. Exact Solution

In the following, we will solve the TIM by first applying a JW transformation to fermionic operators, transforming to k-space via a Fourier transformation and applying a Bogoliubov transformation to new fermionic operators, such that the Hamiltonian becomes diagonal. The derivation mainly follows [10, 11, 12], additional information can be found in e.g. [9, 16]. Applying a JW transformation to (2.26), using the identities (2.4), one gets

$$\begin{aligned}\hat{H}_{TIM} &= -\frac{J}{4}\sum_j \left(c_j^\dagger - c_j\right)\left(c_{j+1}^\dagger + c_{j+1}\right) - h\sum_j \left(c_j^\dagger c_j - \frac{1}{2}\right)\\ &= \frac{Lh}{2} - \frac{J}{4}\sum_j \left(c_j^\dagger - c_j\right)\left(c_{j+1}^\dagger + c_{j+1}\right) - h\sum_j c_j^\dagger c_j,\end{aligned} \tag{2.27}$$

where we have again dropped a correction term $\frac{J}{4}\left(c_L^\dagger - c_L\right)\left(c_1^\dagger + c_1\right)\left((-1)^{N+1} - 1\right)$ (cf. Section 2.2) to solve for pbc. This solution becomes exact in the thermodynamic limit only. Due to the presence of terms such as $c_j^\dagger c_{j+1}^\dagger$ and $c_j c_{j+1}$ the total number of fermions an thus the total magnetization $\hat{S}^z = \sum_j \hat{S}_j^z$ is not a conserved quantity. The Hamiltonian also shows Z_2 symmetry, as it is invariant under rotations by π around the x axis. For consequences of this for the thermodynamic limit ground states see Section 6.3.1.

The Hamiltonian (2.27) is still only quadratic in fermionic operators and can be diagonalized in a straight forward way. At first, transform again to momentum space using (2.15) and the results of (2.16)[2] to get

$$\begin{aligned}\hat{H}_{TIM} &= \frac{Lh}{2} - \frac{J}{4}\sum_k e^{-ik} c_k^\dagger c_{-k}^\dagger + e^{-ik} c_k^\dagger c_k - e^{ik} \underbrace{c_k c_k^\dagger}_{1-c_k^\dagger c_k} - e^{ik} c_k c_{-k} - h\sum_k c_k^\dagger c_k\\ &= \frac{Lh}{2} - \sum_k \left(\frac{J}{2}\cos(k) + h\right) c_k^\dagger c_k - \frac{J}{4}\sum_k e^{-ik} c_k^\dagger c_{-k}^\dagger - e^{ik} c_k c_{-k} + \frac{J}{4}\underbrace{\sum_k e^{ik}}_{=0}.\end{aligned}$$

We will now write the sum for $k > 0$ only, exploiting $\sum_k f(k) = \sum_{0<k\leq\pi} f(k) + f(-k)$[3]

$$\begin{aligned}\hat{H}_{TIM} &= \frac{Lh}{2} + \sum_{k>0} \underbrace{\left(-\frac{J}{2}\cos(k) - h\right)}_{:=A_k}\left(c_k^\dagger c_k + \underbrace{c_{-k}^\dagger c_{-k}}_{1-c_{-k}c_{-k}^\dagger}\right)\\ &\quad + i\sum_{k>0} \underbrace{\frac{J}{2}\sin(k)}_{:=B_k}\left(c_k^\dagger c_{-k}^\dagger + \underbrace{c_k c_{-k}}_{-c_{-k}c_k}\right)\\ &= \frac{Lh}{2} + \sum_{k>0} A_k\left(c_k^\dagger c_k - c_{-k}c_{-k}^\dagger\right) + i\sum_{k>0} B_k\left(c_k^\dagger c_{-k}^\dagger - c_{-k}c_k\right) + K,\end{aligned} \tag{2.28}$$

where

$$K = \sum_{k>0} A_k = -\frac{J}{2}\underbrace{\sum_{k>0}\cos(k)}_{=0} - h\underbrace{\sum_{k>0} 1}_{\frac{L}{2}} = -\frac{Lh}{2}, \tag{2.29}$$

---

[2] the calculations for $c_j^\dagger c_{j+1}^\dagger$ and $c_j c_{j+1}$ work similarly.

[3] In the thermodynamic limit $L \to \infty$, the missing terms for $k = 0$ and $k = \pi$ can be neglected (cf. e.g. [10]).

which exactly cancels with the other constant in (2.28) to finally give

$$\hat{H}_{TIM} = \sum_{k>0} A_k \left(c_k^\dagger c_k - c_{-k} c_{-k}^\dagger \right) + i \sum_{k>0} B_k \left(c_k^\dagger c_{-k}^\dagger - c_{-k} c_k \right). \tag{2.30}$$

As we can see, this Hamiltonian is still not diagonal due to the second sum in (2.30). To diagonalize, we will now perform a *Bogoliubov transformation* of the general form

$$\eta_k = a_k c_k + i b_k c_{-k}^\dagger \qquad\qquad \eta_k^\dagger = a_k c_k^\dagger - i b_k c_{-k}, \tag{2.31}$$

where a_k and b_k are real coefficients, which fulfill the following relations

$$a_k = a_{-k} \qquad b_k = -b_{-k} \qquad a_k^2 + b_k^2 = 1. \tag{2.32}$$

These ensure that the new fermionic operators η_k and $\eta_k^\dagger$ again fulfill the fermionic anticommutator rules. The inverse transformation is then

$$c_k = a_k \eta_k - i b_k \eta_{-k}^\dagger \qquad\qquad c_k^\dagger = a_k \eta_k + i b_k \eta_{-k}. \tag{2.33}$$

The straight forward way now would be to insert (2.33) into (2.30) and adjust the coefficients such that the Hamiltonian becomes diagonal. We will however choose a slightly different, but more efficient method to determine a_k and b_k and check that they fulfill (2.32) afterwards. The inverse transformation, including the Fourier transformation back to real space, then reads

$$c_j = \frac{1}{\sqrt{L}} \sum_k e^{-ikj} \left(a_k \eta_k - i b_k \eta_{-k}^\dagger \right) \qquad c_j^\dagger = \frac{1}{\sqrt{L}} \sum_k e^{ikj} \left(a_k \eta_k^\dagger + i b_k \eta_{-k} \right). \tag{2.34}$$

To transform (2.30) such that it becomes diagonal, we will first write it in matrix form

$$\hat{H}_{TIM} = \sum_{k>0} \begin{pmatrix} c_k^\dagger & c_{-k} \end{pmatrix} \underbrace{\begin{pmatrix} A_k & iB_k \\ -iB_k & -A_K \end{pmatrix}}_{:=M_k} \begin{pmatrix} c_k \\ c_{-k}^\dagger \end{pmatrix}. \tag{2.35}$$

We will then diagonalize M_k, its eigenbasis will correspond to a Bogoliubov transformation, which diagonalizes the Hamiltonian.

The eigenanalysis $M_k = U_k D_k {U_k}^\dagger$, with D_k the diagonal matrix containing the eigenvalues and U_k a unitary matrix containing the eigenvectors, yields

$$\lambda_k = \sqrt{A_k^2 + B_k^2} = \sqrt{\frac{J^2}{4} + Jh\cos(k) + h^2} \tag{2.36}$$

$$D_k = \begin{pmatrix} \lambda_k & 0 \\ 0 & -\lambda_k \end{pmatrix} \tag{2.37}$$

$$U_k = \begin{pmatrix} \frac{\lambda_k + A_k}{N_{k,+}} & \frac{i(\lambda_k - A_k)}{N_{k,-}} \\ \frac{iB_k}{N_{k,+}} & \frac{-B_k}{N_{k,-}} \end{pmatrix} \tag{2.38}$$

$$N_{k,\pm} = \sqrt{2\lambda_k \left(\lambda_k \pm A_k \right)} \tag{2.39}$$

The unitary matrix U_k in (2.38) defines the Bogoliubov transformation to the fermionic operators $\eta_k^\dagger$ and η_k

$$\begin{pmatrix} c_k^\dagger & c_{-k} \end{pmatrix} M_k \begin{pmatrix} c_k \\ c_{-k}^\dagger \end{pmatrix} = \underbrace{\begin{pmatrix} c_k^\dagger & c_{-k} \end{pmatrix} U_k}_{:=\begin{pmatrix} \eta_k^\dagger & \eta_{-k} \end{pmatrix}} D_k \underbrace{U_k{}^\dagger \begin{pmatrix} c_k \\ c_{-k}^\dagger \end{pmatrix}}_{:=\begin{pmatrix} \eta_k \\ \eta_{-k}^\dagger \end{pmatrix}} \rightarrow \begin{pmatrix} \eta_k \\ \eta_{-k}^\dagger \end{pmatrix} = U_k^\dagger \begin{pmatrix} c_k \\ c_{-k}^\dagger \end{pmatrix}. \quad (2.40)$$

Explicitly we get

$$\eta_k = \frac{\lambda_k + A_k}{N_{k,+}} c_k - i \frac{B_k}{N_{k,+}} c_{-k}^\dagger \qquad \eta_k^\dagger = \frac{\lambda_k + A_k}{N_{k,+}} c_k^\dagger + i \frac{B_k}{N_{k,+}} c_{-k}, \quad (2.41)$$

with $a_k = \frac{\lambda_k + A_k}{N_{k,+}}$ and $b_k = -\frac{B_k}{N_{k,+}}$ (cf. also [12]). Indeed, one can see, that both a_k and b_k fulfill the restrictions for Bogoliubov transformation coefficients by inserting into (2.32).

Plugging into (2.35) then gives

$$\begin{aligned} \hat{H}_{TIM} &= \sum_{k>0} \begin{pmatrix} c_k^\dagger & c_{-k} \end{pmatrix} U_k D_k U_k{}^\dagger \begin{pmatrix} c_k \\ c_{-k}^\dagger \end{pmatrix} = \sum_{k>0} \begin{pmatrix} \eta_k^\dagger & \eta_{-k} \end{pmatrix} D_k \begin{pmatrix} \eta_k \\ \eta_{-k}^\dagger \end{pmatrix} \\ &= \sum_{k>0} \lambda_k \eta_k^\dagger \eta_k - \lambda_k \underbrace{\eta_{-k}\eta_{-k}^\dagger}_{1-\eta_{-k}^\dagger \eta_{-k}} = \sum_{k>0} \lambda_k \left(\eta_k^\dagger \eta_k + \eta_{-k}^\dagger \eta_{-k} \right) - \sum_{k>0} \lambda_k \end{aligned} \quad (2.42)$$

and switching back to sum over all k we finally get

$$\hat{H}_{TIM} = \sum_k \lambda_k \eta_k^\dagger \eta_k - \frac{L}{2} \sum_k \lambda_k = \sum_k \lambda_k \left(\eta_k^\dagger \eta_k - \frac{1}{2} \right). \quad (2.43)$$

As one can see, (2.43) is now diagonal in terms of Bogoliubov operators. An excitation of one Bogoliubov fermion of momentum k has energy λ_k, which is always positive. The vacuum state has a negative energy per site $\frac{E_0}{L} = -\frac{1}{2}\sum_k \lambda_k$ and is also the ground state, since every excited fermion increases the energy.

2.3.2. Time Evolution of a JW Excitation

We will proceed similarly as for the XX model. The time dependent Bogoliubov operators can again be derived from solving the Heisenberg equation of motion, which gives

$$\eta_k(t) = \eta_k e^{-i\lambda_k t} \qquad \eta_k^\dagger(t) = \eta_k^\dagger e^{i\lambda_k t}. \quad (2.44)$$

Plugging into (2.34) for the time dependent JW fermion operators in real space, we get

$$c_j(t) = \frac{1}{\sqrt{L}} \sum_k e^{-ikj} \left(\alpha_k \eta_k + \beta_k \eta_{-k}^\dagger \right) \quad (2.45)$$

$$c_j^\dagger(t) = \frac{1}{\sqrt{L}} \sum_k e^{ikj} \left(\alpha_k^* \eta_k^\dagger + \beta_k^* \eta_{-k} \right), \quad (2.46)$$

where we have defined $\alpha_k = a_k e^{-i\lambda_k t}$ and $\beta_k = -ib_k e^{i\lambda_k t}$.

Now consider a single JW excitation to the ground state (i.e. the vacuum state of Bogoliubov fermions), which is defined as

$$|\psi_0\rangle_l = \left(c_l^\dagger + c_l\right)|0\rangle = \frac{1}{\sqrt{L}}\sum_k e^{ikl}\big(\underbrace{a_k + ib_k}_{:=f_k}\big)\eta_k^\dagger|0\rangle\,. \tag{2.47}$$

Notice that $f_k^* = f_{-k}$ and $|f_k|^2 = 1$ due to the properties of a_k and b_k. The advantage of a JW excitation over a regular spin flip is that we can easily calculate in terms of JW fermions without having to worry about any JW phase factor, which we would have for a simple spin flip, as it would not vanish due to the more complicated structure of the TIM ground state. We will now again calculate the time dependent expectation value $\langle \hat{S}_j^z(t)\rangle_l$ of this excited state. Start with

$$\langle \hat{n}_j(t)\rangle_l = \frac{1}{L}\sum_{mn} f_m^* f_n e^{-i(m-n)l}\langle 0|\,\eta_m c_j^\dagger(t) c_j(t)\eta_n^\dagger\,|0\rangle\,. \tag{2.48}$$

Inserting (2.45) and (2.46) and exploiting the fact, that only terms with an equal number of creation and annihilation operators remain, one gets

$$\begin{aligned}
\langle \hat{n}_j(t)\rangle_l &= \frac{1}{L^2}\sum_{mnkk'} f_m^* f_n e^{-i(m-n)l} e^{i(k-k')j}\ \times \\
&\quad \Big(\alpha_k^*\alpha_{k'}\underbrace{\langle 0|\eta_m\eta_k^\dagger\eta_{k'}\eta_n^\dagger|0\rangle}_{\delta_{mk}\delta_{nk'}} + \beta_k^*\beta_{k'}\underbrace{\langle 0|\eta_m\eta_{-k}\eta_{-k'}^\dagger\eta_n^\dagger|0\rangle}_{\delta_{mn}\delta_{kk'}-\delta_{-k'm}\delta_{-kn}}\Big) \\
&= \frac{1}{L^2}\sum_{kk'} f_k^* f_{k'} e^{-(k-k')(l-j)}\alpha_k^*\alpha_{k'} + 1\underbrace{|f_m|^2}_{=1}\underbrace{|\beta_k|^2}_{b_k^2} - \underbrace{f_{-k'}^* f_{-k}}_{f_{k'}f_k^*} e^{-i(k-k')(l-j)}\beta_k^*\beta_{k'} \\
&= \frac{1}{L^2}\Big(\underbrace{\sum_{k'} 1}_{=L}\sum_k b_k^2 + \sum_{kk'} f_k^* f_{k'} e^{-i(k-k')(l-j)}\left(\alpha_k^*\alpha_{k'} - \beta_k^*\beta_{k'}\right)\Big) \\
&= \frac{1}{L}\sum_k b_k^2 + \frac{1}{L^2}\left|\sum_k e^{ik(l-j)} f_k\alpha_k\right|^2 - \frac{1}{L^2}\left|\sum_k e^{ik(l-j)} f_k\beta_k\right|^2 .
\end{aligned} \tag{2.49}$$

For the magnetization $\langle \hat{S}_j^z(t)\rangle_l = \langle \hat{n}_j(t)\rangle_l - \frac{1}{2}$ we get, changing back to a_k and b_k,

$$\langle \hat{S}_j^z(t)\rangle_l = \frac{1}{L}\sum_k b_k^2 + \frac{1}{L^2}\left(\left|\sum_k e^{i[k(l-j)-\lambda_k t]} f_k a_k\right|^2 - \left|\sum_k e^{i[k(l-j)+\lambda_k t]} f_k b_k\right|^2\right) - \frac{1}{2} \tag{2.50}$$

2.4. The XXZ model

The XXZ model is a widely studied spin chain model with many applications, which as of today far surpass its original purpose of explaining ferromagnetism. Heisenberg and Dirac [17] first realized that the quantum mechanical effect of exchange interaction leads to an effective spin-spin interaction $W_{ij} = J_{ij}\hat{\mathbf{S}}_i \cdot \hat{\mathbf{S}}_j$ for particles i and j with overlapping wave functions, where J_{ij} the interaction parameter, which can also be negative. Thus for the first time the mysterious effect of ferromagnetism, which was not understood at that time, could be addressed on a quantum mechanical level. The magnetic properties of many magnetic materials can be described by either isotropic or anisotropic ferromagnetic or antiferromagnetic Heisenberg interactions, described by an accordingly modeled three-dimensional XYZ Hamiltonian and ab initio parameters $J_{ij}^{x,y,z}$. The homogeneous XXZ chain is a special case of the XYZ chain (2.1) with nearest neighbor interactions only and $J^x = J^y = J$. In one dimension, the XXZ model can be solved exactly by the Bethe ansatz (see Section 2.4.1). Extensions to the Bethe ansatz also solve the one-dimensional XYZ model.

The general structure of the model itself however allows for the treatment of many other phenomena that can be described in terms of (or mapped onto) spin operators. For example, Mott insulators in the Hubbard model can be described with an effective antiferromagnetic Heisenberg Hamiltonian. Also for the negative-U model, describing superconductivity, the charge operators can be mapped onto pseudo spin operators, yielding an anisotropic effective XXZ Hamiltonian with ferromagnetic xy-coupling $J > 0$ and antiferromagnetic z-coupling $J^z < 0$, which can describe charge density waves (cf. e.g. [18]).

The model itself is still a very simple model for a nearest neighbor interaction spin chain, however a straight forward exact solution as for the other spin chain models above is not possible. We will consider only magnetic fields in z, parametrized by h^z

$$\hat{H}_{XXZ} = -\sum_j J\left(\hat{S}_j^x\hat{S}_{j+1}^x + \hat{S}_j^y\hat{S}_{j+1}^y\right) + J^z\hat{S}_j^z\hat{S}_{j+1}^z - h^z\sum_j \hat{S}_j^z \tag{2.51}$$

$$= -\frac{J}{2}\sum_j \hat{S}_j^+\hat{S}_{j+1}^- + \hat{S}_j^-\hat{S}_{j+1}^+ - J^z\sum_j \hat{S}_j^z\hat{S}_{j+1}^z - h^z\sum_j \hat{S}_j^z \tag{2.52}$$

$$= -J\sum_j \frac{1}{2}\left(\hat{S}_j^+\hat{S}_{j+1}^- + \hat{S}_j^-\hat{S}_{j+1}^+\right) + \Delta\hat{S}_j^z\hat{S}_{j+1}^z - h^z\sum_j \hat{S}_j^z, \tag{2.53}$$

where $\Delta = \frac{J^z}{J}$. Notice that the isotropic case $J = J^z$ or $\Delta = 1$ and $h^z = 0$ yields the conventional isotropic Quantum Heisenberg model

$$\hat{H}_{HB} = -J\sum_j \hat{\mathbf{S}}_j \cdot \hat{\mathbf{S}}_{j+1}. \tag{2.54}$$

Again, we consider the case of an L-site chain with pbc. A JW transformation of (2.53), using $\hat{S}_j^z = \hat{n}_j - \frac{1}{2}$ and $\hat{S}_j^z\hat{S}_{j+1}^z = \hat{n}_j\hat{n}_{j+1} - \frac{1}{2}\left(\hat{n}_j + \hat{n}_{j+1}\right) + \frac{1}{4}$ yields

$$\hat{H}_{XXZ} = -\frac{J}{2}\sum_j c_j^\dagger c_{j+1} + c_{j+1}^\dagger c_j - J^z\sum_j \hat{n}_j\hat{n}_{j+1} + \left(J^z - h^z\right)\sum_j \hat{n}_j, \tag{2.55}$$

where we have dropped an energy offset of $-\frac{L}{4}\left(J^z - 2h^z\right)$ and again a correction term for pbc (cf. Section 2.2). Comparing with the general XYZ Hamiltonian (2.7) we can see that we again have fermion hopping, controlled by the hopping parameter J and also nearest neighbor particle-particle interaction controlled by J^z, as well as a chemical potential $\mu = J^z - h^z$. Clearly, this Hamiltonian is now quartic in fermion operators, usual methods of diagonalizing a quadratic Hamiltonian are thus not applicable.

Symmetries and Ground States The XXZ Hamiltonian also preserves total magnetization in $\hat{S}^z$ or total particle number $\hat{N}$ as the XX chain. Similarly, a rotation of every other spin by π around the z axis transforms $J \to -J$ or $\hat{H}_{XXZ}(J, \Delta) \to \hat{H}_{XXZ}(-J, \Delta)$, but we can also pull out the sign and write $\hat{H}_{XXZ}(J, \Delta) \to -\hat{H}_{XXZ}(J, -\Delta)$. On consequences of this for the time evolution of certain signals types, see Section 6.2

The case $\Delta = 1$ corresponds to the isotropic Heisenberg ferromagnet (FM), whereas $\Delta = -1$ corresponds to the isotropic Heisenberg antiferromagnet (AFM). The cases $\Delta \to \pm\infty$ yield the classical Ising (anti)ferromagnet, whereas $\Delta = 0$ yields the above described XX model. Furthermore, for $J > 0$ we get ferromagnetic (FM) behavior for $\Delta \geq 1$ for all values of S^z and antiferromagnetic (AFM) behavior for $\Delta \leq -1$ and $S^z = 0$. For $-1 < \Delta < 1$ and $S^z = 0$ the system is paramagnetic (cf. [19]).

For $h^z = 0$ and $\Delta \neq 1$ the Hamiltonian is also invariant under rotations of π about any axis in the xy plane. This will result in a 2 fold degeneracy of the FM ground state. For the Heisenberg FM with $\Delta = 1$ the ground state is $L+1$ fold degenerate due to the full rotational symmetry, where $\hat{\mathbf{S}}^2 = \sum_j \hat{\mathbf{S}}_j^2$ is also a conserved quantity. Energetically, spin alignment is favored for the FM, the ground state(s) will therefore have long range magnetic ordering with (generally) finite magnetization S^z.

The ground state for the AFM case is much more complicated. Even though antiparallel spin ordering is favored by the Ising interaction $J^z < 0$, the two Néel states as well as their symmetric and antisymmetric superposition are not eigenstates of $\hat{H}_{XXZ}$. Lieb, Schultz and Mattis [9] proved for the Heisenberg AFM ($\Delta = -1$) that the ground state of the linear chain is non degenerate and has total magnetization $S^z = 0$ or $\frac{L}{2}$ particles, i.e. the ground state shows half filling. They further proved that the ground state has indeed contributions of *all* states within the subspace of half filling. These proofs form the foundation of the *Lieb-Schultz-Mattis Theorem*, stating that the linear chain with pbc becomes gapless in the thermodynamic limit, i.e. there exist excited eigenstates with energies going towards the ground state energy with the chain becoming infinitely long.

2.4.1. Exact Solution: Bethe Ansatz

For the one-dimensional chain with $h^z = 0$ and pbc there exists an exact solution, proposed by Hans Bethe in 1931, which is known as the famous *Bethe ansatz* [20]. We will now take a short look at this solution, a good introduction can be found in [21] and also in [19]. Consider an L-site chain with pbc and L even. The essence of this ansatz is the classification of all possible states of an L-site chain by their particle numbers. This is a good classification since the particle number is a conserved quantity, i.e. applications of H do not interchange between different particle subspaces. We can therefore solve the system for eigenvalues and eigenvectors in the respective particle number subspaces individually.

The following short sketch follows [21] closely. Start with the fully saturated FM ground state with L particles, i.e. the all spin up state $|F\rangle = |\uparrow_1 \ldots \uparrow_L\rangle$. We can sequentially remove particles by applying the ladder operator $\hat{S}_n^-$ to yield a $L-1$ particle state

$$|n\rangle = \hat{S}_n^- |F\rangle , \qquad n = 1, \ldots, L \tag{2.56}$$

Thus a general eigenstate with $L-1$ particles can be written as a linear combination of all $L-1$ particle states (2.56)

$$|\psi\rangle_{L-1} = \sum_n a(n) |n\rangle , \tag{2.57}$$

where the parameters $a(n)$ have to be adjusted such that $|\psi\rangle_{L-1}$ is an eigenstate of H. For $L-1$ particles we get

$$a(n) = e^{ikn}, \qquad k = \frac{2\pi m}{L}, \qquad -\frac{L}{2} \leq m \leq \frac{L}{2} - 1, \tag{2.58}$$

i.e. L eigenstates with $L-1$ particles.

For the general case of $L-r$ particles we write the eigenstates in a similar fashion

$$|\psi\rangle_{L-r} = \sum_{1 \leq n_1 < \ldots < n_r \leq L} a(n_1, \ldots, n_r) |n_1 \ldots n_r\rangle \tag{2.59}$$

$$|n_1 \ldots n_r\rangle = \hat{S}_{n_1}^- \ldots \hat{S}_{n_r}^- |F\rangle . \tag{2.60}$$

To adjust the coefficients such, that the above states are eigenstates of H, we take the ansatz

$$a(n_1, \ldots, n_r) = \sum_{\mathcal{P}} exp \left(i \sum_{j=1}^{r} k_{\mathcal{P}_j} n_j + \frac{i}{2} \sum_{l<j} \Theta_{\mathcal{P}_l \mathcal{P}_j} \right) , \tag{2.61}$$

where $\mathcal{P}$ denotes the $r!$ permutations of the labels $1, \ldots, r$ and Θ_{lj} are the 2-body scattering phases, which must fulfill

$$2 \cot \frac{\Theta_{lj}}{2} = \cot \frac{k_l}{2} - \cot \frac{k_j}{2}, \qquad l, j = 1, \ldots, r. \tag{2.62}$$

Periodicity demands the additional relation

$$Lk_j = 2\pi \lambda_j + \sum_{l \neq j} \Theta_{jl}, \qquad j = 1, \ldots, r \tag{2.63}$$

where $\lambda_j \in \{0, 1, \ldots, L-1\}$ are the Bethe quantum numbers, defining the momentum of the eigenstate as $k = \frac{2\pi}{L} \sum_{j=1}^{r} \lambda_j$. The energy of the eigenstate is then

$$E - E_0 = J \sum_{j=1}^{r} (1 - \cos(k_j)) . \tag{2.64}$$

Notice that the total momentum of the eigenstate is in general not the sum of the r momenta k_j.

With this ansatz for the coefficients, which defines the Bethe ansatz, and the above relations the eigenvalue problem reduces to solving for the r values of the Bethe quantum numbers and the allowed values of the momenta k_j. This task itself can be numerically demanding. The Bethe ansatz however allows for better identification of different classes and properties of the eigenstates. Among them are e.g. bound states, where the probability to find the flipped spins on neighboring sites is strongly enhanced. On the other hand the Bethe ansatz also allows for (limited) analytic investigation of certain other properties (cf. e.g. [21]).

3. Matrix Product States (MPS)

In recent years a special class of quantum states for the description of correlated many body systems has gained much attention: Matrix Product States (MPS). After the huge success of the Density Matrix Renormalization Group (DMRG) method [1] and Östlund and Rommers realization, that DMRG produces exactly this kind of ansatz states [4], MPS have become a very active field of research. While originally developed for one-dimensional lattice systems, there are also generalizations to e.g. higher dimensions [22], continuous fields [23] or even applications in statistical mechanics for transfer matrices [24].

The key feature of MPS is their ability to describe one-dimensional quantum states and their features by a product of *locally* defined matrices of relatively small dimension, with high precision. Consider a general one-dimensional quantum spin system with L lattice sites, open boundary conditions and local Hilbert spaces $\{|\sigma_i\rangle\}$ of dimension d on each site. A general (possibly unnormalized) pure state on this spin system can be written in terms of the local spin bases as

$$|\tilde{\psi}\rangle = \sum_{\{\sigma\}} c_{\sigma_1 \dots \sigma_L} |\sigma_1 \dots \sigma_L\rangle \,, \tag{3.1}$$

where we have in general d^L independent, delocalized expansion coefficients $c_{\sigma_1 \dots \sigma_L}$. The idea is now to find a representation that allows for a local description of this state, while still keeping its general quantum mechanical, non local features. As will be shown below, it is indeed possible to decompose the coefficients of (3.1) into a product of site dependent matrices of the following form

$$c_{\sigma_1 \dots \sigma_L} = M^{\sigma_1} M^{\sigma_2} \dots M^{\sigma_{L-1}} M^{\sigma_L} \tag{3.2}$$

by subsequent decomposition of $c_{\sigma_1 \dots \sigma_L}$, where the spin variables σ_j are now merely a labeling for the matrices M, i.e. for each physical site j there is a set of d MPS matrices for each value of σ_j. Each of the d^L coefficients can now be constructed by taking the product of the corresponding matrices M^{σ_j} for each site. In general these matrices will be site dependent, so actually a labeling such as $M^{(j),\sigma_j}$ is more appropriate. However, for the sake of brevity we will use this notation only when site dependence is of importance.

In the following Sections 3.2 and 3.4 we will sketch the exact decomposition of a general state of the form (3.1) into an MPS. For this we will reinterpret the expansion coefficients $c_{\sigma_1 \dots \sigma_L}$ as a rectangular matrix and sequentially perform matrix decompositions to achieve (3.2). We will see that the dimensions of these matrices will grow exponentially with each decomposition step going towards the center of the chain.

In Section 3.3 we will reinterpret the decomposition process as a sequential growth of an L-site system from a small initial system by sequentially adding sites and performing a basis transformation to a new basis set of the enlarged system. We will also make the connection between MPS representations and Schmidt decompositions.

Due to the fact that matrix dimensions grow exponentially, the exact MPS representations derived in Sections 3.2 and 3.4 are not very useful for efficient numerical methods. In Section 3.5 we will introduce a maximum matrix dimension for all MPS matrices, truncating (most of) the MPS matrices to this maximum dimension. The resulting MPS is then only an approximation to the originally decomposed state of the form (3.1). We will however see, that the decomposition procedures of Sections 3.2 and 3.4 then represent an optimal approximation to the original state. This is due to the entanglement structure in one-dimensional systems. We will also see that most of the feature derived in the preceding Sections will still hold even for truncated MPS.

The decomposition (3.2) is highly non unique. We will therefore look for a decomposition with useful features that best serves our needs. In general one could use any matrix decomposition method to retrieve (3.2), but in order to construct a representation that is able to optimally describe the entanglement structure of the state, we will use the *singular value decomposition (SVD)*. For further references, see the very detailed and complete reviews [25], which we will follow closely in the following derivations.

3.1. Singular Value Decomposition (SVD)

In the following Sections for deriving MPS representations, but also in the context of MPS methods, we will make extensive use of the *singular value decomposition (SVD)*. The SVD is a factorization of a real or complex matrix with dimensions $m \times n$ into a product of two matrices and a diagonal matrix of the form

$$M = UDV^\dagger, \qquad M_{ij} = \sum_{k=1}^{N} U_{ik} D_k V^\dagger_{kj}, \tag{3.3}$$

where $N = \min(m, n)$. U is a $m \times N$ matrix, containing the orthonormal *left singular vectors* of M as its columns and V is a $n \times N$ matrix containing the *right singular vectors* of M as its columns. D is a diagonal $N \times N$ matrix with the N singular values d_k of M as its diagonal elements, which are real and non negative.

If $m < n$, U is a unitary square matrix of dimension $m \times m$, hence $U^\dagger U = UU^\dagger = \mathbb{1}$, whereas V is a $n \times m$ matrix with $V^\dagger V = \mathbb{1}$ only.

If $n < m$, V is a unitary square matrix of dimension $n \times n$, with $V^\dagger V = VV^\dagger = \mathbb{1}$ and U is a $m \times n$ matrix with $U^\dagger U = \mathbb{1}$ only.

Notice that there are only $\min(m, n)$ singular values d_k, which are the diagonal elements of D. For future applications, consider D with its singular values in descending order, i.e. $d_1 \geq d_2 \geq \ldots$.

For a graphical representation of the two cases $m < n$ and $n < m$ see Figure 3.1.

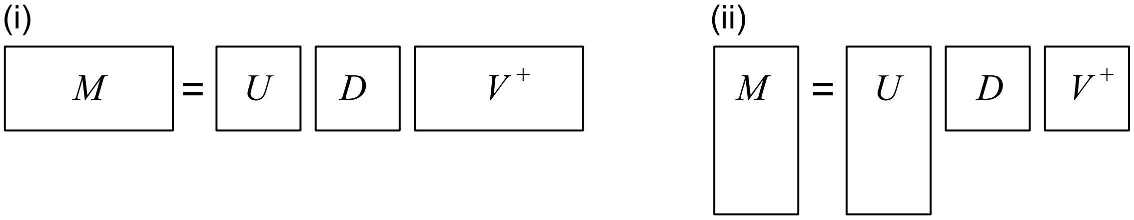

Figure 3.1.: Singular Value Decomposition of a $m \times n$ matrix M. (i) If $m < n$, U is a square unitary $m \times m$ matrix and V is a $m \times n$ matrix with $V^\dagger V = \mathbb{1}$ only. (ii) If $n < m$, V is a square unitary $n \times n$ matrix and U is a $n \times m$ matrix with $U^\dagger U = \mathbb{1}$ only. D is a diagonal matrix of dimensions $\min(m,n) \times \min(m,n)$, with the singular values of M as its diagonal elements.

The left and right singular vectors $u_i^{(k)} = U_{ik}$ and $v_i^{(k)} = V_{ik}$ fulfill the following left and right singular relations

$$M^\dagger u^{(k)} = d_k v^{(k)} \qquad\qquad M v^{(k)} = d_k u^{(k)}. \tag{3.4}$$

The SVD can also be understood as a generalized eigen decomposition to factorize non square matrices. Combining (3.3) and its hermitian conjugate in fact yields the decomposition of a square matrix in form of an eigen decomposition

$$MM^\dagger = UD\underbrace{V^\dagger V}_{\mathbb{1}}DU^\dagger = UD^2U^\dagger \tag{3.5}$$

$$M^\dagger M = VD\underbrace{U^\dagger U}_{\mathbb{1}}DV^\dagger = VD^2V^\dagger. \tag{3.6}$$

The columns of U are the eigen vectors of $MM^\dagger$, whereas the columns of V are the eigen vectors of $M^\dagger M$. Both $MM^\dagger$ and $M^\dagger M$ have the same spectrum of eigen values $d_k^2 > 0$.

3.2. Exact MPS Representations

We will start by reshaping the coefficient $c_{\sigma_1 \ldots \sigma_L}$ into a $d \times d^{L-1}$ matrix and subject it to an SVD

$$c_{\sigma_1 \ldots \sigma_L} = \psi_{(\sigma_1)(\sigma_2 \ldots \sigma_L)} \overset{SVD}{=} \sum_{a_1=1}^{d} U_{(\sigma_1)a_1} \lambda_{a_1}^{(1)} V^\dagger_{a_1(\sigma_2 \ldots \sigma_L)}. \tag{3.7}$$

$U_{(\sigma_1)a_1}$ will be a $d \times d$ matrix, we will reshape it into $A_{a_1}^{\sigma_1} = U_{(\sigma_1)a_1}$ and call it the left boundary matrix. In this form it is a set of d row vectors of length d, now *labeled* by the physical index σ_1. The vector elements are labeled with a_1, which we call auxiliary indices. In practice it is just a $d \times d$ matrix.

Next we will incorporate $\lambda^{(1)}_{a_1}$ into $V^\dagger_{a_1(\sigma_2\ldots\sigma_L)}$ again and reshape it to form a new matrix $\psi_{(a_1\sigma_2)(\sigma_3\ldots\sigma_L)} = \lambda^{(1)}_{a_1} V^\dagger_{a_1(\sigma_2\ldots\sigma_L)}$, now of dimension $d^2 \times d^{L-2}$. Thus we have

$$c_{\sigma_1\ldots\sigma_L} = \sum_{a_1=1}^{d} A^{\sigma_1}_{a_1} \psi_{(a_1\sigma_2)(\sigma_3\ldots\sigma_L)} \tag{3.8}$$

and we will proceed the same way as above with $\psi_{(a_1\sigma_2)(\sigma_3\ldots\sigma_L)}$. Decompose via SVD

$$\psi_{(a_1\sigma_2)(\sigma_3\ldots\sigma_L)} = \sum_{a_2=1}^{d^2} U_{(a_1\sigma_2)a_2} \lambda^{(2)}_{a_2} V^\dagger_{a_2(\sigma_3\ldots\sigma_L)} \tag{3.9}$$

and use $U_{(a_1\sigma_2)a_2}$ to again form a set of matrices $A^{\sigma_2}_{a_1a_2}$, which is now a collection of d matrices of dimensions $d \times d^2$, labeled by σ_2. We can again combine and form $\psi_{(a_2\sigma_3)(\sigma_4\ldots\sigma_l)} = \lambda^{(2)}_{a_2} V^\dagger_{a_2(\sigma_3\ldots\sigma_L)}$ to get

$$c_{\sigma_1\ldots\sigma_L} = \sum_{a_1=1}^{d} \sum_{a_2=1}^{d^2} A^{\sigma_1}_{a_1} A^{\sigma_2}_{a_1a_2} \psi_{(a_2\sigma_3)(\sigma_4\ldots\sigma_L)}, \tag{3.10}$$

where $A^{\sigma_\ell}_{a_{\ell-1}a_\ell}$ will be a collection of d matrices, labeled by σ_ℓ, of dimensions $d^{\ell-1} \times d^\ell$ while $\ell \leq \frac{L}{2}$. For $\ell < \frac{L}{2}$, $\psi_{(a_\ell\sigma_{\ell+1})(\sigma_{\ell+1}\ldots\sigma_L)}$ is a rectangular matrix of dimensions $m \times n$ where $m < n$, making $U_{(a_{\ell-1}\sigma_\ell)(a_\ell)}$ a square matrix of dimension $d^\ell \times d^\ell$. For $\ell > \frac{L}{2}$ we face the fact that now $n < m$, making $U_{(a_{\ell-1}\sigma_\ell)(a_\ell)}$ a rectangular matrix of dimension $d^\ell \times d^{L-\ell}$. $A^{\sigma_\ell}_{a_{\ell-1}a_\ell}$ will therefore be a collection of d matrices of dimensions $d^{\ell-1} \times d^{L-\ell}$. This is a consequence of the nature of an SVD (cf. Section 3.1). We can repeat these steps until we reach the last step

$$c_{\sigma_1\ldots\sigma_L} = \sum_{a_1a_2\ldots a_{L-1}} A^{\sigma_1}_{a_1} A^{\sigma_2}_{a_1a_2} \ldots A^{\sigma_{L-1}}_{a_{L-2}a_{L-1}} \lambda^{(L-1)}_{a_{L-1}} V^\dagger_{a_{L-1}(\sigma_L)}, \tag{3.11}$$

where we will reshape one last time and form a column vector $\psi_{(a_{L-1}\sigma_L)} = \lambda^{(L-1)}_{a_{L-1}} V^\dagger_{a_{L-1}(\sigma_L)}$, which we will subject to one more SVD

$$\psi_{(a_{L-1}\sigma_L)} = U_{(a_{L-1}\sigma_L)} \lambda^{(L)} V^*, \tag{3.12}$$

where U is again a column vector. $\lambda^{(L)}, V^*$ are scalars, their product gives the norm $N = \sqrt{\langle\tilde{\psi}|\tilde{\psi}\rangle}$ of the original state (3.1), automatically enabling us to normalize the state. We form the last matrix $A^{\sigma_L}_{a_{L-1}} = U_{(a_{L-1}\sigma_L)}$ and write down the coefficients of the original state as a product of L matrices

$$\begin{aligned} c_{\sigma_1\ldots\sigma_L} &= N \sum_{a_1a_2\ldots a_{L-2}a_L} A^{\sigma_1}_{a_1} A^{\sigma_2}_{a_1a_2} \ldots A^{\sigma_{L-1}}_{a_{L-2}a_{L-1}} A^{\sigma_L}_{a_{L-1}} && (3.13) \\ &= N A^{\sigma_1} A^{\sigma_2} \ldots A^{\sigma_{L-1}} A^{\sigma_L}, && (3.14) \end{aligned}$$

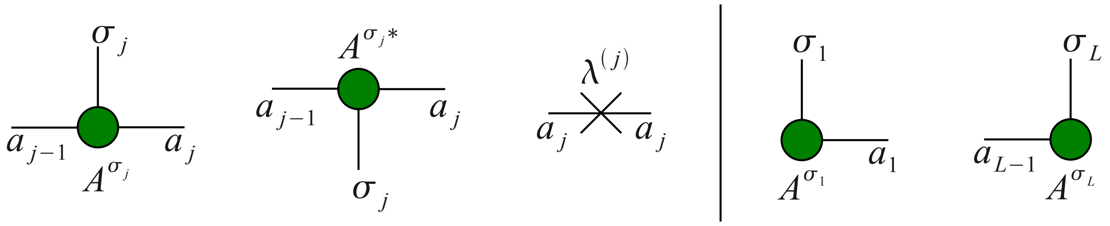

Figure 3.2.: Graphical representation of MPS matrices. Matrices are represented by circles and indices by lines. Vertical lines represent physical indices of corresponding sites, horizontal lines represent auxiliary indices connecting adjacent sites. Complex conjugate matrices are depicted by an upside down version. Singular Values are represented by crosses. They can be viewed as diagonal matrices with the singular values as their diagonal elements. Boundary matrices only have one auxiliary index, shown are the left and right boundary matrix. All graphical representations equally hold for B-matrices as well.

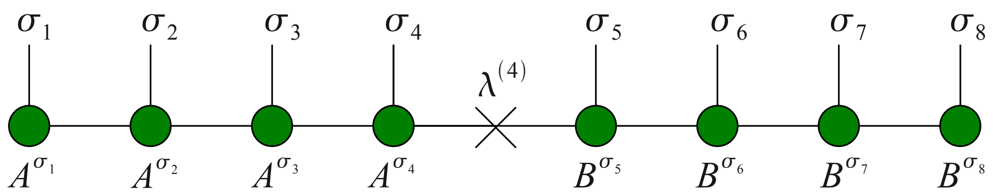

Figure 3.3.: Graphical representation of an 8 site mixed-canonical MPS. Whenever 2 lines of different matrices are connected, there is an implicit sum over these indices. Notice that in the depicted MPS matrix network all auxiliary indices are summed over and the only degrees of freedom are the physical indices σ_j. This exactly represents one general coefficient $c_{\sigma_1 \ldots \sigma_8}$ in MPS representation.

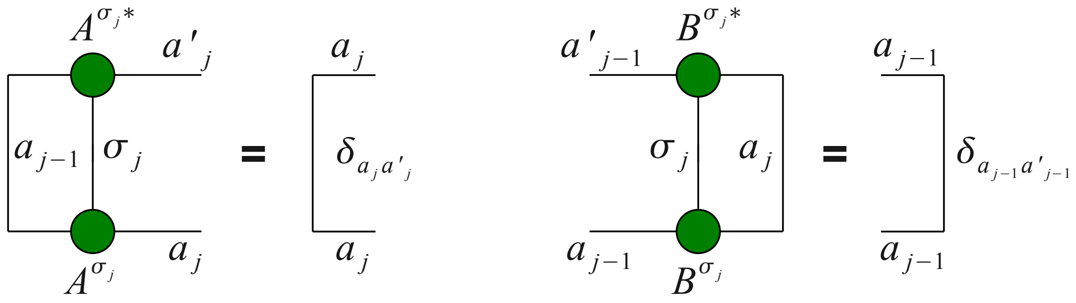

Figure 3.4.: Graphical representation of the left and right normalization conditions (3.18) and (3.19). In index notation they each produce a Kronecker-delta in the remaining auxiliary space. This fact can be widely exploited to calculate e.g. norms and expectation values (cf. Section 3.6).

where we have switched to matrix notation in the last line. At last, we can write down the normalized state as

$$|\psi\rangle = \sum_{\{\sigma\}} A^{\sigma_1} A^{\sigma_2} \dots A^{\sigma_{L-1}} A^{\sigma_L} \, |\sigma_1 \dots \sigma_L\rangle \, . \tag{3.15}$$

We can construct a similar MPS representation the by starting to decompose from the right end. In this case we will perform SVDs of the form

$$\psi_{(\sigma_1 \dots \sigma_{\ell-1})(\sigma_\ell a_\ell)} = \sum_{a_{\ell-1}} U_{(\sigma_1 \dots \sigma_{\ell-1}) a_{\ell-1}} \lambda^{(\ell-1)}_{a_{\ell-1}} V^\dagger_{a_{\ell-1}(\sigma_\ell a_\ell)}, \tag{3.16}$$

and reshape to form $B^{\sigma_\ell}_{a_{\ell-1} a_\ell} = V^\dagger_{a_{\ell-1}(\sigma_\ell a_\ell)}$ and $\psi_{(\sigma_1 \dots \sigma_{\ell-2})(\sigma_{\ell-1} a_\ell)} = U_{(\sigma_1 \dots \sigma_{\ell-1}) a_{\ell-1}} \lambda^{(\ell-1)}_{a_{\ell-1}}$ for the next decomposition. This way we will create an MPS of the form

$$|\psi\rangle = \sum_{\{\sigma\}} B^{\sigma_1} B^{\sigma_2} \dots B^{\sigma_{L-1}} B^{\sigma_L} \, |\sigma_1 \dots \sigma_L\rangle \, , \tag{3.17}$$

where we have similar dimensionality considerations for the $B^{\sigma_\ell}_{a_{\ell-1} a_\ell}$ as for the construction of (3.15).

Since the matrices A^{σ_i} and B^{σ_ℓ} arise from an SVD they automatically fulfill the so called *left- and right-normalization* conditions

$$\sum_{\sigma_\ell} A^{\sigma_\ell \dagger} A^{\sigma_\ell} = \mathbb{1} \tag{3.18}$$

$$\sum_{\sigma_\ell} B^{\sigma_\ell} B^{\sigma_\ell \dagger} = \mathbb{1}. \tag{3.19}$$

The state (3.15) is therefore called a *left-normalized* MPS, which is automatically normalized with all matrices fulfilling (3.18), whereas (3.17) is called a *right-normalized* MPS, which is also normalized with all matrices fulfilling (3.19). For a graphical representation see Figures 3.2, 3.3 and 3.4.

We can also mix these two representations to form a *mixed-canonical* state. To this behalf we perform left-canonized decomposition up to a certain site ℓ, where we have an intermediate state with coefficients

$$c_{\sigma_1 \dots \sigma_L} = \sum_{a_1 \dots a_\ell} A^{\sigma_1}_{a_1} A^{\sigma_2}_{a_1 a_2} \dots A^{\sigma_{\ell-1}}_{a_{\ell-2} a_{\ell-1}} \psi_{(a_{\ell-1} \sigma_\ell)(\sigma_{\ell+1} \dots \sigma_L)} \tag{3.20}$$

Now perform right-canonical decomposition of $\psi_{(a_{\ell-1} \sigma_\ell)(\sigma_{\ell+1} \dots \sigma_L)}$ from the right up to site $\ell + 1$

$$\psi_{(a_{\ell-1} \sigma_\ell)(\sigma_{\ell+1} \dots \sigma_L)} = \sum_{a_{\ell+1} \dots a_{L-1}} \psi_{(a_{\ell-1} \sigma_\ell)(\sigma_{\ell+1} a_{\ell+1})} B^{\sigma_{\ell+2}}_{a_{\ell+1} a_{\ell+2}} \dots B^{\sigma_{L-1}}_{a_{L-2} a_{L-1}} B^{\sigma_L}_{a_{L-1}} \tag{3.21}$$

and plug back into (3.20) to get

$$c_{\sigma_1 \dots \sigma_L} = \sum_{\substack{a_1 \dots a_\ell \\ a_{\ell+1} \dots a_{L-1}}} A^{\sigma_1}_{a_1} A^{\sigma_2}_{a_1 a_2} \dots A^{\sigma_{\ell-1}}_{a_{\ell-2} a_{\ell-1}} \psi_{(a_{\ell-1} \sigma_\ell)(\sigma_{\ell+1} a_{\ell+1})} B^{\sigma_{\ell+2}}_{a_{\ell+1} a_{\ell+2}} \dots B^{\sigma_{L-1}}_{a_{L-2} a_{L-1}} B^{\sigma_L}_{a_{L-1}}.$$

$$(3.22)$$

Reshape and define $\Psi^{\sigma_\ell\sigma_{\ell+1}}_{a_{\ell-1}a_{\ell+1}} = \psi_{(a_{\ell-1}\sigma_\ell)(\sigma_{\ell+1}a_{\ell+1})}$ as the *2-site wave function* of sites $\ell, \ell+1$. We can leave (3.22) like it is or perform one last SVD to get $\Psi^{\sigma_\ell\sigma_{\ell+1}} = A^{\sigma_\ell}\lambda^{(\ell)}B^{\sigma_{\ell+1}}$, where $\lambda^{(\ell)}$ is a diagonal matrix with the singular values $\lambda^{(\ell)}_{a_\ell}$ as its diagonal elements. At last we can write the MPS in its *mixed-canonical* representation as

$$|\psi\rangle = \sum_{\{\sigma\}} A^{\sigma_1}A^{\sigma_2}\dots A^{\sigma_{\ell-1}}\underline{\Psi^{\sigma_\ell\sigma_{\ell+1}}}B^{\sigma_{\ell+2}}\dots B^{\sigma_{L-1}}B^{\sigma_L}\,|\sigma_1\dots\sigma_L\rangle \tag{3.23}$$

$$|\psi\rangle = \sum_{\{\sigma\}} A^{\sigma_1}A^{\sigma_2}\dots A^{\sigma_{\ell-1}}\dots\underline{A^{\sigma_\ell}\lambda^{(\ell)}B^{\sigma_{\ell+1}}}B^{\sigma_{\ell+2}}\dots B^{\sigma_{L-1}}B^{\sigma_L}\,|\sigma_1\dots\sigma_L\rangle\,, \tag{3.24}$$

where the underlined parts correspond to the above mentioned 2-site wave function (in its decomposed form in (3.24)). Notice that the position of the 2-site wave function is arbitrary and need not be the center of the chain.

The hermitian conjugate of this state is derived by just taking the complex conjugate of the matrix product. For future calculations it is convenient to reverse the matrix product for the hermitian conjugate state, requiring hermitian conjugates of the MPS matrices in turn

$$\langle\psi| = \sum_{\{\sigma\}} B^{\sigma_L\dagger}\dots B^{\sigma_{\ell+1}\dagger}\Psi^{\sigma_{\ell+1}\sigma_\ell\dagger}A^{\sigma_{\ell-1}\dagger}\dots A^{\sigma_1\dagger}\,\langle\sigma_1\dots\sigma_L| \tag{3.25}$$

$$\langle\psi| = \sum_{\{\sigma\}} B^{\sigma_L\dagger}\dots B^{\sigma_\ell\dagger}\lambda^{(\ell)}A^{\sigma_\ell\dagger}\dots A^{\sigma_1\dagger}\,\langle\sigma_1\dots\sigma_L|\,. \tag{3.26}$$

3.3. Basis Transformations and Schmidt Decompositions

The MPS matrices represent basis transformations from a product space of an auxiliary and a physical space to another auxiliary space

$$|a^L_\ell\rangle = \sum_{\sigma_\ell a_{\ell-1}} A^{\sigma_\ell}_{a_{\ell-1}a_\ell}\,|a^L_{\ell-1}\rangle\,|\sigma_\ell\rangle\,, \tag{3.27}$$

$$|a^R_\ell\rangle = \sum_{\sigma_\ell a_{\ell+1}} B^{\sigma_\ell}_{a_\ell a_{\ell+1}}\,|\sigma_\ell\rangle\,|a^R_{\ell+1}\rangle\,. \tag{3.28}$$

$|a^L_{\ell-1}\rangle$ and $|a^R_{\ell+1}\rangle$ describe states on blocks containing sites left or right of site ℓ, i.e. $[1,\dots,\ell-1]$ and $[\ell+1,\dots,L]$ respectively. Due to the normalization conditions (3.18) and (3.19) the new states $|a^L_\ell\rangle$ and $|a^R_\ell\rangle$ form orthonormal basis sets if $\{|a^L_{\ell-1}\rangle\,|\sigma_\ell\rangle\}$ and $\{|\sigma_{\ell+1}\rangle\,|a^R_{\ell+1}\rangle\}$ were orthonormal basis sets too. Starting with a single site one can construct block states for blocks containing L sites by sequentially adding sites to the left or to the right and transforming onto new block states using (3.27) or (3.28) (cf. Figure 3.5). Since the basis transformations represented by $A^{\sigma_\ell}_{a_{\ell-1}a_\ell}$ and $B^{\sigma_\ell}_{a_\ell a_{\ell+1}}$ connect blocks of spins and additional single spin, one can interpret the auxiliary indices a_ℓ as living on the bonds between sites. This fact is included in the graphical representations

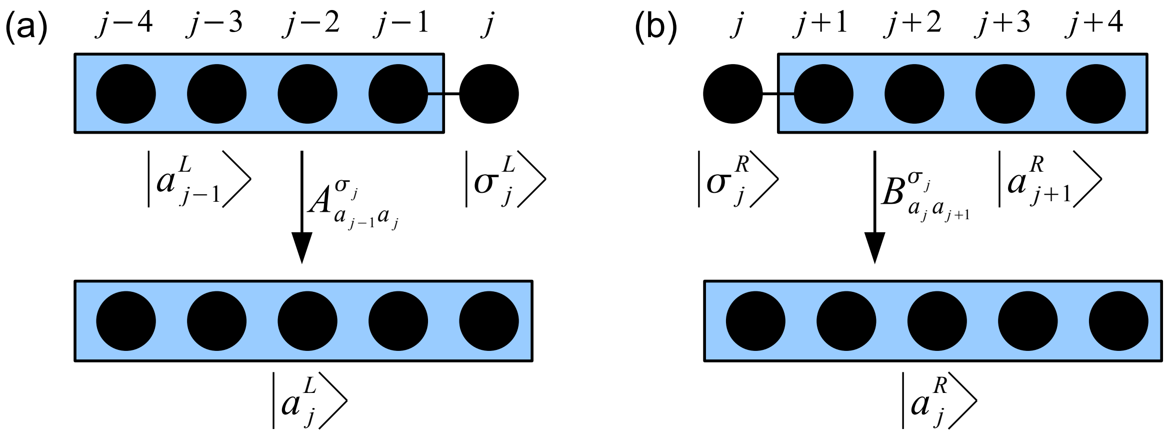

Figure 3.5.: (a) Block enlargement from the left. A block containing $\ell-1$ sites is enlarged by adding one site to the right. From the old block states $|a^L_{\ell-1}\rangle$ and the local spin states $|\sigma_\ell\rangle$ for the added site, new block states $|a^L_\ell\rangle$ for the enlarged block are constructed via (3.27). (b) Block enlargement from the right. Similarly, block states can be generated by adding sites to the left using (3.28).

of MPS matrices, as auxiliary indices are represented by horizontal lines connecting two MPS matrices sitting on adjacent sites (cf. Figure 3.3).

We will now show how the mixed canonical representation corresponds to a Schmidt decomposition of $|\psi\rangle$ at bond $\ell, \ell+1$. Consider a general splitting of a state in terms of basis states defined on two sublattices, which are the two parts of the lattice left and right of bond $\ell, \ell+1$

$$|\psi\rangle = \sum_{ij} C_{ij} \, |\psi^L_i\rangle \, |\psi^R_j\rangle \,, \tag{3.29}$$

where $\{|\psi^L_i\rangle\}$ and $\{|\psi^R_j\rangle\}$ are orthonormal basis sets defined on the sublattice L containing sites $[1, \ldots, \ell]$ and sublattice R containing sites $[\ell+1, \ldots, L]$. C_{ij} is a matrix of expansion coefficients. In general, dimensions of both Hilbert spaces are not equal, so C_{ij} is a rectangular matrix.

A Schmidt decomposition is a special case of such a split up, where the overall state is written as in (3.29), but choosing basis sets for the left and right sides in such a way that the expansion coefficient matrix only contains diagonal elements. This can be achieved by performing an SVD of the expansion coefficient matrix $C_{ij} = U_{ik}\lambda_k V^\dagger_{kj}$. Matrices U and V then correspond to basis transformations onto new orthonormal basis sets on both sublattices, so that one can write

$$|\psi\rangle = \sum_{ijk} U_{ik}\lambda_k V^\dagger_{kj} |\psi^L_i\rangle |\psi^R_j\rangle = \sum_k \lambda_k \underbrace{\left(\sum_i U_{ik} |\psi^L_i\rangle\right)}_{=:|\phi^L_k\rangle} \underbrace{\left(\sum_j V^*_{jk} |\psi^R_j\rangle\right)}_{=:|\phi^R_k\rangle} \tag{3.30}$$

$$= \sum_k \lambda_k |\phi^L_k\rangle |\phi^R_k\rangle \,. \tag{3.31}$$

(3.31) is then a Schmidt decomposition, the weights λ_k are called Schmidt values and correspond to the singular values of C_{ij}. The vectors $\{|\phi^L_k\rangle\}$ and $\{|\phi^L_k\rangle\}$ are called left and right Schmidt vectors, which again form orthonormal basis sets. As one can see, there is only one sum over basis states and each left Schmidt vector only gets paired with one right Schmidt vector, i.e. there is no mixing as in (3.29).

We will now assume that the block states for blocks L and R generated sequentially by (3.27) and (3.28) are indeed Schmidt vectors of a Schmidt decomposition at bond $\ell, \ell+1$ and show that by sequentially decomposing the block states into local spin states, the Schmidt decomposition in fact corresponds to the mixed-canonical representation (3.24). The Schmidt decomposition of $|\psi\rangle$ at bond $\ell, \ell+1$ then reads

$$|\psi\rangle = \sum_{a_\ell} \lambda^{(\ell)}_{a_\ell} |a^L_\ell\rangle |a^R_\ell\rangle \,. \tag{3.32}$$

We can now recover the representation of the Schmidt vectors $|a^L_\ell\rangle$ of the left sublattice in the local spin bases by recursively using the basis transformations (3.27)

$$|a^L_\ell\rangle = \sum_{\sigma_\ell a_{\ell-1}} A^{\sigma_\ell}_{a_{\ell-1}a_\ell} |a^L_{\ell-1}\rangle |\sigma_\ell\rangle \tag{3.33}$$

$$= \sum_{\substack{\sigma_\ell\sigma_{\ell-1} \\ a_{\ell-1}a_{\ell-2}}} A^{\sigma_{\ell-1}}_{a_{\ell-2}a_{\ell-1}} A^{\sigma_\ell}_{a_{\ell-1}a_\ell} |a^L_{\ell-2}\rangle |\sigma_{\ell-1}\rangle |\sigma_\ell\rangle \tag{3.34}$$

$$= \ldots \tag{3.35}$$

and equivalently (3.28) for $|a^R_\ell\rangle$ to finally get

$$|a^L_\ell\rangle = \sum_{\sigma_1\ldots\sigma_\ell} \left(A^{\sigma_1}\ldots A^{\sigma_\ell}\right)_{a_\ell} |\sigma_1\ldots\sigma_\ell\rangle \tag{3.36}$$

$$|a^R_\ell\rangle = \sum_{\sigma_\ell\ldots\sigma_L} \left(B^{\sigma_\ell}\ldots B^{\sigma_L}\right)_{a_\ell} |\sigma_{\ell+1}\ldots\sigma_L\rangle \,. \tag{3.37}$$

Plugging both of these expressions back into (3.32) exactly yields the MPS in mixed-canonical representation (3.24). This means that the mixed-canonical representation at sites $\ell, \ell+1$ with matrices A and B fulfilling (3.18) and (3.19) in fact represents a valid Schmidt decomposition at that bond and that the singular values $\lambda^{(\ell)}_{a_\ell}$ of (3.24) are indeed the Schmidt values of the corresponding Schmidt decomposition.

From the Schmidt decomposition we can also easily construct the reduced density operators for blocks L and R, yielding

$$\hat{\rho}_L^{(\ell)} = \mathrm{Tr}_R \left|\psi\right\rangle \left\langle\psi\right| = \sum_{a_\ell} \lambda_{a_\ell}^{(\ell)^2} \left|a_\ell^L\right\rangle \left\langle a_\ell^L\right| \tag{3.38}$$

$$\hat{\rho}_R^{(\ell)} = \mathrm{Tr}_L \left|\psi\right\rangle \left\langle\psi\right| = \sum_{a_\ell} \lambda_{a_\ell}^{(\ell)^2} \left|a_\ell^R\right\rangle \left\langle a_\ell^R\right|, \tag{3.39}$$

where Tr_R and Tr_L denote the partial traces over block states of blocks R and L respectively.

We can see that the *Schmidt vectors are the eigenvectors of the reduced density operators with eigenvalues* $\lambda_{a_\ell}^{(\ell)^2}$, which fulfill the necessary constraint $\sum_{a_\ell} = \lambda_{a_\ell}^{(\ell)^2} = 1$ for a statistical operator if the state is normalized. This also means that the singular values $\lambda_{a_\ell}^{(\ell)}$ of (3.32) quantify the bipartite entanglement entropy between blocks L and R via the *von Neumann entropy*

$$S_{LR} = -\,\mathrm{Tr}\,\hat{\rho}_L \log_2 \hat{\rho}_L = -\,\mathrm{Tr}\,\hat{\rho}_R \log_2 \hat{\rho}_R \overset{(3.38),(3.39)}{=} -\sum_{a_\ell} \lambda_{a_\ell}^{(\ell)^2} \log_2 \lambda_{a_\ell}^{(\ell)^2}. \tag{3.40}$$

3.4. Canonical Representation

In Section 3.2 we have already encountered several MPS representations. These representations focus on sequential system growth by iterative application of MPS matrices as basis transformations. This is essentially the viewpoint used in DMRG (cf. Section 4.1.1 and [1, 4]). Another slightly different representation of MPS, whose focus lies more on the Schmidt decomposition, is used in the TEBD algorithm (cf. Section 4.2.2 and [2]). The aim of this representation is to easily access all possible Schmidt decompositions at all bonds at all times. As we have shown above, the Schmidt decomposition at bond $\ell, \ell+1$ (3.32) can be written as a mixed canonical MPS (3.24). However in this form this is the only accessible Schmidt decomposition, since only the Schmidt values and Schmidt vectors at this bond are available. Thus we need a representation that gives us access to all Schmidt values and Schmidt vectors at all bonds simultaneously. This can be done by slightly modifying the decomposition procedure described in Section 3.2.

We will again start with (3.7) and reshape U to define $\Gamma_{a_1}^{\sigma_1} = U_{(\sigma_1)a_1}$, thus we have

$$A_{a_1}^{\sigma_1} = \Gamma_{a_1}^{\sigma_1}. \tag{3.41}$$

We will then keep proceeding according to (3.9), but we will remember $\lambda^{(1)}$. After performing an SVD on $\psi_{(a_1\sigma_2)(\sigma_3\ldots\sigma_L)}$ and remembering that we have included $\lambda^{(1)}$ in its formulation we can now again reshape $U_{(a_1\sigma_2)a_2} = A_{a_1a_2}^{\sigma_2}$ and redefine $A_{a_1a_2}^{\sigma_2} = \lambda_{a_1}^{(1)}\Gamma_{a_1a_2}^{\sigma_2}$. Proceed with the decomposition, remember all singular values $\lambda^{(\ell)}$ and redefine all

$$A_{a_{\ell-1}a_\ell}^{\sigma_\ell} = \lambda_{a_{\ell-1}}^{(\ell-1)}\Gamma_{a_{\ell-1}a_\ell}^{\sigma_\ell}, \tag{3.42}$$

also for $\ell = L$.

We can proceed similarly when decomposing from the right, where we will then redefine

$$B^{\sigma_L}_{a_{L-1}} = \Gamma^{\sigma_L}_{a_{L-1}} \tag{3.43}$$
$$B^{\sigma_\ell}_{a_{\ell-1}a_\ell} = \Gamma^{\sigma_\ell}_{a_{\ell-1}a_\ell}\lambda^{(\ell)}_{a_\ell}. \tag{3.44}$$

We can now either replace all A-matrices in (3.15), replace all B-matrices in (3.17) or even replace both kinds in (3.24) and write in matrix notation

$$|\psi\rangle = \sum_{\{\sigma\}} \Gamma^{\sigma_1}\lambda^{(1)}\Gamma^{\sigma_2}\lambda^{(2)}\Gamma^{\sigma_3}\dots\Gamma^{\sigma_{L-2}}\lambda^{(L-2)}\Gamma^{\sigma_{L-1}}\lambda^{(L-1)}\Gamma^{\sigma_L}\,|\sigma_1\dots\sigma_L\rangle\,. \tag{3.45}$$

There is no distinction between left- or right-canonization anymore, we will therefore call this form the *canonical representation* of an MPS.

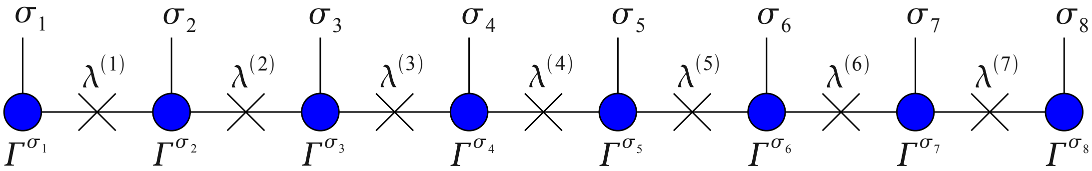

Figure 3.6.: Graphical representation of an MPS in canonical representation. Γ-matrices are depicted the same way as A- and B-matrices, but with blue color coding (cf. Figure 3.2). Schmidt values are represented by crosses. Again, connected lines imply sums, open ends imply degrees of freedom.

We can now easily access all Schmidt decompositions of all bonds, since the singular values $\lambda^{(\ell)}$ exactly correspond to the Schmidt values at all bonds. For any bond $\ell, \ell+1$ we can write according to (3.32)

$$|\psi\rangle = \sum_{a_\ell} \lambda^{(\ell)}_{a_\ell}\,|a^L_\ell\rangle\,|a^R_\ell\rangle\,, \tag{3.46}$$

where we can now write the Schmidt vectors as

$$|a^L_\ell\rangle = \sum_{\sigma_1\dots\sigma_\ell} \left(\Gamma^{\sigma_1}\lambda^{(1)}\Gamma^{\sigma_2}\dots\lambda^{(\ell-1)}\Gamma^{\sigma_\ell}\right)_{a_\ell}|\sigma_1\dots\sigma_\ell\rangle \tag{3.47}$$
$$|a^R_\ell\rangle = \sum_{\sigma_{\ell+1}\dots\sigma_L} \left(\Gamma^{\sigma_{\ell+1}}\lambda^{(\ell+1)}\dots\Gamma^{\sigma_{L-1}}\dots\lambda^{(L-1)}\Gamma^{\sigma_L}\right)_{a_\ell}|\sigma_{\ell+1}\dots\sigma_L\rangle\,. \tag{3.48}$$

We can also see that the boundary matrices are identical in both the mixed-canonical and the canonical representation (cf. (3.41) and (3.43)). Comparing the definitions (3.42) and (3.44) to the normalization conditions for A- and B-matrices (3.18) and (3.19), we can immediately derive normalization conditions for the canonical representation

$$\sum_{\sigma_\ell} \Gamma^{\sigma_\ell \dagger} {\lambda^{(\ell-1)}}^2 \Gamma^{\sigma_\ell} = \mathbb{1} \tag{3.49}$$

$$\sum_{\sigma_\ell} \Gamma^{\sigma_\ell} {\lambda^{(\ell)}}^2 \Gamma^{\sigma_\ell \dagger} = \mathbb{1}, \tag{3.50}$$

defining $\lambda^{(0)} = \lambda^{(L)} = 1$.

Similarly, the fact that we can write any of the three representations introduced in Section 3.2 in the canonical form enables us to translate between A- and B- matrices

$$A^{\sigma_\ell} \lambda^{(\ell)} = \lambda^{(\ell-1)} B^{\sigma_\ell} = \lambda^{(\ell-1)} \Gamma^{\sigma_\ell} \lambda^{(\ell)}. \tag{3.51}$$

For this, see also Section 4.1.3 and Figure 4.6 therein, where this property is used for a substantial speedup to the finite size DMRG algorithm in form of a prediction algorithm.

For the 2-site wave function in (3.23) we then get

$$\Psi^{\sigma_\ell \sigma_{\ell+1}} = \lambda^{(\ell-1)} \Gamma^{\sigma_\ell} \lambda^{(\ell)} \Gamma^{\sigma_{\ell+1}} \lambda^{(\ell+1)}. \tag{3.52}$$

This also enables us to reformulate the normalization conditions in terms of reduced density matrices. Using (3.38) and (3.39) we see that we can write them in their eigenbasis representations just as $\rho_L^{(\ell)} = \rho_R^{(\ell)} = {\lambda^{(\ell)}}^2$. Now multiply each side of (3.49) with $\lambda^{(\ell)}$ from both sides which yields

$$\sum_{\sigma_\ell} \underbrace{\lambda^{(\ell)} \Gamma^{\sigma_\ell \dagger}}_{B^{\sigma_\ell \dagger}} \underbrace{{\lambda^{(\ell-1)}}^2}_{\rho_R^{(\ell-1)}} \underbrace{\Gamma^{\sigma_\ell} \lambda^{(\ell)}}_{B^{\sigma_\ell}} = \rho_R^{(\ell)}, \tag{3.53}$$

and similar for (3.50) to give the following relations

$$\rho_R^{(\ell)} = \sum_{\sigma_\ell} B^{\sigma_\ell \dagger} \rho_R^{(\ell-1)} B^{\sigma_\ell} \tag{3.54}$$

$$\rho_L^{(\ell-1)} = \sum_{\sigma_\ell} A^{\sigma_\ell} \rho_L^{(\ell)} A^{\sigma_\ell \dagger}. \tag{3.55}$$

3.5. Truncation

Up until now we have considered the MPS matrices A and B to be unitary basis transformations without truncation. This means that every state can be *exactly* decomposed into an MPS without information loss. But it also means that the transformed basis sets grow exponentially in dimension the further we go into the center of the chain. The Hilbert spaces of $\{|a_\ell^L\rangle\}$ and $\{|a_\ell^R\rangle\}$ are thus of dimension d^ℓ and $d^{L-\ell}$ respectively. This is not exactly useful for a practical representation of the state (3.1), as we will then have to deal with a very large amount of numbers, which is in general more than the d^L coefficients in (3.1)! It is therefore useful to introduce a maximum dimension m for the MPS matrices and cutting all matrices of larger size to that maximum dimension. Truncated MPS matrices will then generally be a collection of d matrices of dimension $m \times m$. By doing this, we will obviously discard information of the MPS decomposition and the derived MPS will generally only be an approximation of the original state.

Even after truncation, condition (3.18) is still fulfilled for A-matrices and (3.19) still holds for B-matrices. Remember that A- and B-matrices are constructed from (the hermitian conjugate of) matrices stemming from an SVD, which consist of orthonormal vectors as their columns. The normalization conditions just reflect the orthonormality of the kept eigenstates from the SVD, which always holds, no matter how many states are discarded. The same reasoning also holds for MPS in canonical representation, where (3.49) and (3.50) still hold.

The basis transformations represented by the MPS matrices described in Section 3.3 now turn into reduced basis transformations generally from a $d \times m$ dimensional product space of an auxiliary space and a single spin to another auxiliary space of dimension m. These reduced basis transformations will correspond to the renormalization group (RG) transformations performed during the DMRG algorithm explained in Section 4.1.1. As we will see, DMRG is optimizing this truncation in a way, such that the norm of the residual between the true and the approximate state is minimal. However there are also states that can be exactly expressed in MPS form with very low dimension, the most notable of these being the ground state of the AKLT model [26].

If the decomposition into an MPS is performed via consecutive SVDs, as described above, the optimal truncation method of the DMRG algorithm can already be used. The procedure is very simple. We introduce an upper limit m for the dimensions of the MPS matrices. Every time we perform an SVD of $\psi = U\lambda V^\dagger$, we only use the first m left and right singular vectors – corresponding to the m largest Schmidt values – if the matrix dimensions exceed m. This means we will only use the first m columns of U and the first m rows of $V^\dagger$ and discard the rest.

By limiting all MPS matrix dimensions to a maximum of m, we will now have to deal with an amount of $\mathcal{O}\left(Lm^2\right)$ numbers in stead of 2^L coefficients. Thus memory effort now scales *linearly* with system size, as opposed to *exponentially* for a state of the form (3.1). Due to the entanglement nature of one-dimensional systems, truncated MPS are still very good approximations, even for small matrix dimensions m. In one dimension, bipartite entanglement between the left and right block, which make up a system of certain size, is at most $\propto \log(L)$, with L the system size. This holds for critical systems, for non critical systems, the bipartite entanglement does not scale with system size, but is constant everywhere. For further interpretation and truncation errors see remarks in Section 4.1.1 or cf. [25].

Decomposing a state of the form (3.1) into its MPS form following the above procedure is hardly applicable, since the coefficients $c_{\sigma_1 \ldots \sigma_L}$ are generally unknown. The procedure thus serves a conceptional purpose only. An efficient way to construct a mixed canonical representation of low energy states of an L site chain is the DMRG algorithm, described in Section 4.1.1.

3.6. Norms and Expectation Values

The local structure of MPS and the normalization conditions for MPS matrices allows for a very efficient calculation of norms and expectation values of local observables. The following derivations closely follows [25], where details on the below calculations can be found.

Consider an MPS in mixed-canonical form (3.24). Its norm $\langle\psi|\psi\rangle$ can be written using (3.26)

$$\langle\psi|\psi\rangle = \sum_{\{\sigma\}} \left(B^{\sigma_L\dagger} \dots B^{\sigma_\ell\dagger} \lambda^{(\ell)} A^{\sigma_\ell\dagger} \dots A^{\sigma_1\dagger}\right) \left(A^{\sigma_1} A^{\sigma_2} \dots A^{\sigma_\ell} \lambda^{(\ell)} B^{\sigma_{\ell+1}} \dots B^{\sigma_{L-1}} B^{\sigma_L}\right). \tag{3.56}$$

By sequentially using normalizations conditions (3.18) and (3.19), rearranging and rebracketing in the process one finds for the norm

$$\langle\psi|\psi\rangle = \sum_{a_\ell} {\lambda^{(\ell)}_{a_\ell}}^2, \tag{3.57}$$

where $\lambda^{(\ell)}_{a_\ell}$ are the diagonal elements of $\lambda^{(\ell)}$. This corresponds to the fact that the eigenvalues of the reduced density operators sum up to 1 if the state is properly normalized (cf. Figure 3.7).

We can extend the above result to calculate expectation values of local operators. Consider a local Operator on site j in its local spin basis representation

$$\hat{O}_j = \sum_{\sigma'_j \sigma_j} O^{\sigma'_j \sigma_j} \left|\sigma'_j\right\rangle \left\langle\sigma_j\right|. \tag{3.58}$$

Its expectation value in a state in mixed-canonical MPS form can be written as follows

$$\begin{aligned} \langle\hat{O}_j\rangle &= \langle\psi|\hat{O}_j|\psi\rangle \\ &= \sum_{\sigma'_j} \sum_{\{\sigma\}} \left(A^{\sigma_1} \dots A^{\sigma'_j} \lambda^{(j)} B^{\sigma_{j+1}} \dots B^{\sigma_L}\right)^\dagger O^{\sigma'_j \sigma_j} \left(A^{\sigma_1} \dots A^{\sigma_j} \lambda^{(j)} B^{\sigma_{j+1}} \dots B^{\sigma_L}\right). \end{aligned} \tag{3.59}$$

Notice, that only matrices A^{σ_j} and $A^{\sigma'_j}$ are summed over different local states σ'_j and σ_j. One can now go back from matrix notation to summing over all auxiliary indices of MPS matrices. By rearranging and exploiting the normalization conditions (3.18) and (3.19) one finds that all MPS matrices except for A^{σ_j} and $A^{\sigma'_j}$ cancel out and one is left with the following expression by defining the center matrix $M^{\sigma_j} = A^{\sigma_j}\lambda^{(j)}$

$$\langle\hat{O}_j\rangle = \sum_{\sigma'_j \sigma_j} O^{\sigma'_j \sigma_j} \operatorname{Tr}\left({M^{\sigma'_j}}^\dagger M^{\sigma_j}\right). \tag{3.60}$$

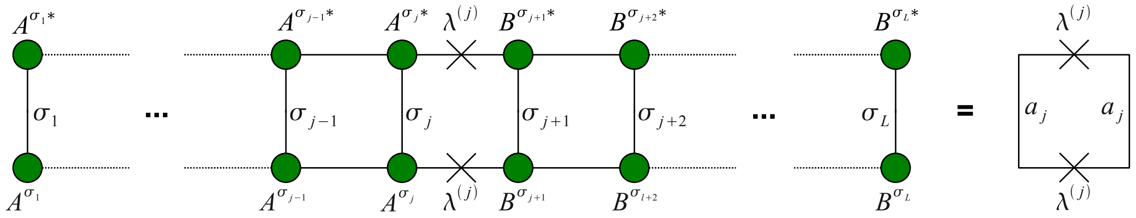

Figure 3.7.: Calculating the norm of a state in MPS form. By exploiting the normalization conditions of MPS matrices (cf. Figure 3.4) sequentially from the outside, one finds that all matrix products cancel out and one is left with the sum over the square of the Schmidt values of the current Schmidt decomposition.

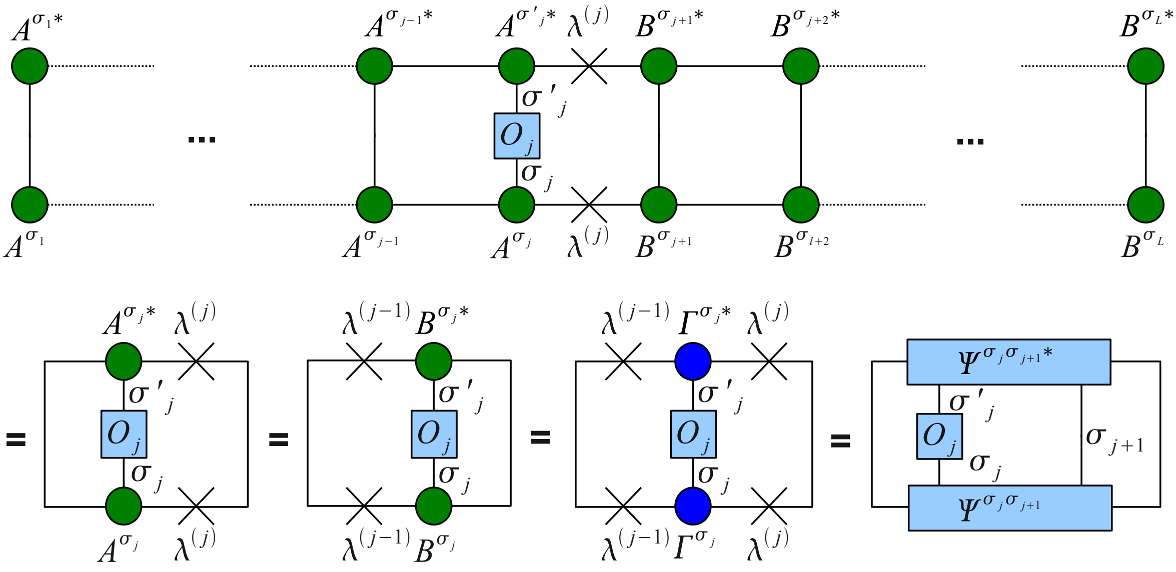

Figure 3.8.: Calculation of the expectation value $\langle \hat{O}_j \rangle$ of a local operator. Exploiting the normalization conditions of the MPS matrices and shifting the center part of the mixed-canonical representation or using the 2-site wave function yields the four possible results in the second line, where A- and B-matrices are depicted in green and Γ-matrices in blue.

By comparing with (3.51) we can see that the center matrix M can be equally written as

$$M^{\sigma_j} = A^{\sigma_j}\lambda^{(j)} = \lambda^{(j-1)}B^{\sigma_j} = \lambda^{(j-1)}\Gamma^{\sigma_j}\lambda^{(j)} \tag{3.61}$$

We can see, that all one needs are the MPS matrices at site j and the adjacent Schmidt values instead of d^L general coefficients in the case of states like (3.1)! We can also formulate the expectation value in terms of the 2-site wave function $\Psi^{\sigma_j\sigma_{j+1}}$

$$\langle\hat{O}_j\rangle = \sum_{\sigma'_j\sigma_j\sigma_{j+1}} O^{\sigma'_j\sigma_j}\,\mathrm{Tr}\left(\Psi^{\sigma_{j+1}\sigma'_j\dagger}\Psi^{\sigma_j\sigma_{j+1}}\right). \tag{3.62}$$

For all these expressions cf. Figure 3.8. For expectation values of operators defined on multiple sites and correlations see [25].

4. MPS Methods

4.1. Density Matrix Renormalization Group (DMRG)

Renormalization group methods have been an instrument for solving models in statistical mechanics for decades. Applications in numerics are e.g. Wilson's *Numerical Renormalization Group (NRG)* [27], which is also applicable to quantum models. In fact even today it still represents one of the best methods to solve quantum impurity models such as the Anderson Impurity Model [28, 29].

By far the most powerful and successful method for determining ground states and low energy states of one-dimensional strongly correlated, slightly entangled systems however is the *Density Matrix Renormalization Group (DMRG)* [1]. It is a variational method, its general principle is to find a state $|\Psi\rangle$ in a certain class of ansatz states (mixed-canonical MPS in the case of DMRG) that minimizes the energy expectation value

$$E = \frac{\langle\Psi|\,\hat{H}\,|\Psi\rangle}{\langle\Psi|\Psi\rangle}. \tag{4.1}$$

Like all renormalization group methods, it relies on constructing an underlying system site by site by subsequent reduced basis transformations, projecting onto important degrees of freedom. A renormalized Hilbert space of the underlying system is generated step by step, which will be of significantly lower dimension.

The major success of DMRG lies within the efficient projection method it uses. In every step it projects onto a (generally fixed) number of states, which are the most prominent eigenstates of the reduced density matrix of the system of current size (hence the name). After L steps one is left with an effective Hamiltonian for the underlying L site system, but with significantly reduced Hilbert space dimension. This procedure yields by far better results for strongly correlated one-dimensional models than projecting onto e.g. low energy states of the system of current size (NRG). The ground state (and possibly the first few excited states) of this Hamiltonian can then easily be determined by the use of efficient iterative eigensolvers such as the Lanczos or Davidson method. As a matter of fact this step is performed in every DMRG iteration, so at the end one automatically gets an approximate representation of the L-site system ground state. We will see that these states have MPS structure.

In the following, the concept of DMRG is explained in short, more information can be found in the very detailed reviews [25] or in the original publications [1], which we will mainly follow. Essentially there are two versions of the DMRG, namely *infinite size DMRG* and *finite size DMRG*.

4.1.1. Infinite Size DMRG (iDMRG)

This algorithm was originally merely a tool to give a good starting point for the finite size DMRG algorithm explained in 4.1.3. Its essential purpose is to generate an effective Hamiltonian and an approximate ground state in MPS form for an L-site system, which is then further optimized in one or more sweeps of the finite size algorithm. However recently its potential to derive thermodynamic limit ground states has been rediscovered by optimizing the algorithm through an efficient prediction algorithm and by giving an efficient measure of convergence for the algorithm [30] (cf. Section 4.1.2).

For the sake of concreteness let us consider an isotropic spin-$\frac{1}{2}$ Heisenberg chain of length L and obc with the Hamiltonian

$$\hat{H} = -J \sum_{i=1}^{L} \frac{1}{2} \left(\hat{S}_i^+ \hat{S}_{i+1}^- + \hat{S}_i^- \hat{S}_{i+1}^+ \right) + \hat{S}_i^z \hat{S}_{i+1}^z = \sum_{i=1}^{L} \hat{h}_{i,i+1} \tag{4.2}$$

$$\hat{h}_{i,i+1} = -\frac{J}{2} \left(\hat{S}_i^+ \hat{S}_{i+1}^- + \hat{S}_i^- \hat{S}_{i+1}^+ \right) - J \hat{S}_i^z \hat{S}_{i+1}^z . \tag{4.3}$$

We will construct the system of size L by starting with a system of very small size ℓ, calling it the initial *system block* S. We will embed this system block in an environment, represented by an *environment block* E, which is constructed the same way as the system block S. We will then iteratively enlarge both blocks at the same time, effectively inserting 2 sites between blocks S and E to form a *superblock* $B = S \bullet \bullet E$ of size $2\ell + 2$. We will then determine the superblock ground state and apply reduced basis transformations (see below). We iterate this procedure until $2\ell + 2 = L$. The superblock Hamiltonian and the superblock ground state will then be a good approximation for the L-site system.

We will start off with a block S of some small initial size ℓ. The Hamiltonian $\hat{H}_\ell^S$ and its constituting operators $\hat{S}_{j\leq\ell}^{\alpha,S}$ are assumed to be known exactly in terms of the local spin basis $\{|a_\ell^S\rangle\} \equiv \{|\sigma_1^S \dots \sigma_\ell^S\rangle\}$. Initially, this basis is of dimension $M_S = d^\ell$, where d is the dimension of the local physical Hilbert space on each site (for spin-$\frac{1}{2}$ $d = 2$) and $M_S < m$ with m the reduced Hilbert space dimension specified a priori (cf. Section 3.5). Construct the initial block E the same way. Then proceed according to the following steps.

(1) Enlarge block S by adding one site to form block $S' = S\bullet$ of size $\ell' = \ell + 1$, enlarging the Hilbert space dimension to $M_{S'} = dM_S$. Determine $\hat{H}_{\ell+1}^{S'} = \hat{H}_\ell^S + \hat{h}_{\ell,\ell+1}$ in the basis $\{|a_\ell^S\rangle\,|\sigma_{\ell+1}^S\rangle\}$ of block S'. To generate $\hat{h}_{\ell,\ell+1}$, both the surface spin operators of block S, $\hat{S}_\ell^{\alpha,S}$, and the spin operators $\hat{S}_{\ell+1}^\alpha$ on the single site $\ell + 1$ in the basis of S' are required. Equivalently, enlarge E to form $E' = \bullet E$ and $\hat{H}_{\ell+1}^{E'}$ the same way.

(2) Form the superblock $B = S \bullet \bullet E = S'E'$ and the superblock Hamiltonian

$$\hat{H}^B = \hat{H}_{\ell+1}^{S'} + \hat{h}_{S'E'} + \hat{H}_{\ell+1}^{E'}, \tag{4.4}$$

with $\hat{h}_{S'E'} = \frac{J}{2} \left(\hat{S}_{\ell+1}^{+,S'} \hat{S}_{\ell+1}^{-,E'} + \hat{S}_{\ell+1}^{-,S'} \hat{S}_{\ell+1}^{+,E'} \right) + J \hat{S}_{\ell+1}^{z,S'} \hat{S}_{\ell+1}^{z,E'}$ the 2-site Hamiltonian connecting blocks S' and E'. The superblock Hamiltonian is of dimension $M^B =$

$d^2 M^S M^E$. Use an iterative eigensolver to determine the *superblock ground state*

$$|\Psi\rangle = \sum_{a_\ell^S \sigma_{\ell+1}^S \sigma_{\ell+1}^E a_\ell^E} \Psi_{(a_{\ell+1}^S \sigma_\ell^S)(\sigma_{\ell+1}^E a_\ell^E)} \left|a_\ell^S \sigma_{\ell+1}^S\right\rangle \left|\sigma_{\ell+1}^E a_\ell^E\right\rangle = \sum_{ij} \Psi_{ij} |i\rangle |j\rangle , \tag{4.5}$$

using $|i\rangle = |a_\ell^S \sigma_{\ell+1}^S\rangle$ and $|j\rangle = |\sigma_{\ell+1}^E a_\ell^E\rangle$. Notice, that we can write the coefficients of the superblock ground state as a $M^{S'} \times M^{E'}$ matrix Ψ.

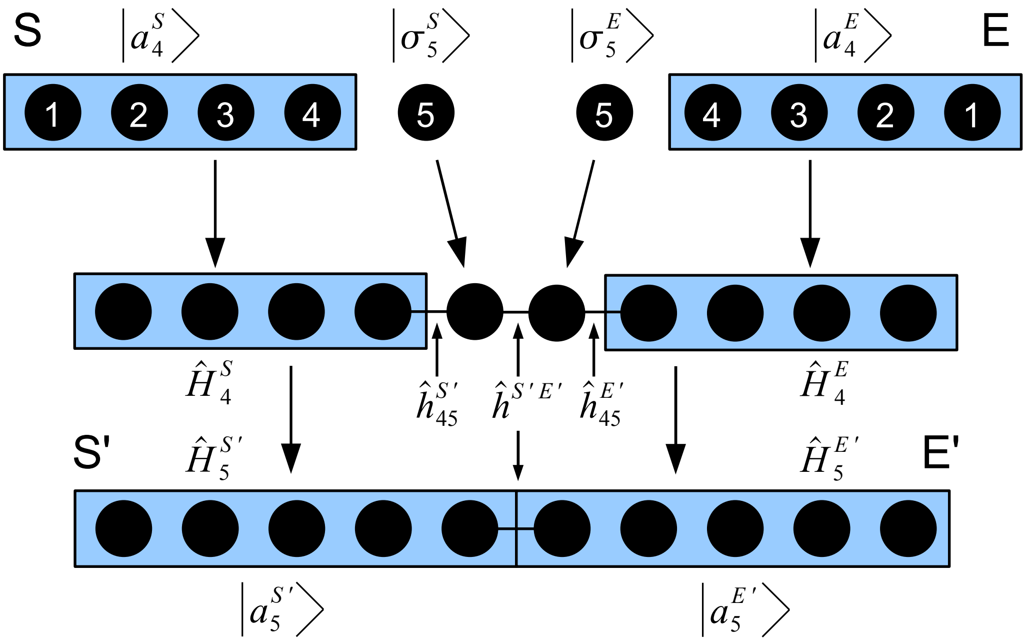

Figure 4.1.: Enlarging both blocks S and E by inserting one site for each block in between. The superblock $B = S \bullet\bullet E$ and its Hamiltonian $\hat{H}^B = \hat{H}_\ell^S + \hat{h}_{\ell,\ell+1}^S + \hat{h}_{S'E'} + \hat{h}_{\ell,\ell+1}^E + \hat{H}_\ell^E$ is formed.

(3) From the derived superblock ground state, form the reduced density operators $\hat{\rho}^{S'} = \mathrm{Tr}_{E'} |\Psi\rangle \langle\Psi|$ and $\hat{\rho}^{E'} = \mathrm{Tr}_{S'} |\Psi\rangle \langle\Psi|$, with $\mathrm{Tr}_{E'}, \mathrm{Tr}_{S'}$ the trace over the basis states of E' and S' respectively. Represented in the basis states of S' and E' the reduced density matrices read

$$\rho_{ii'}^{S'} = \sum_j \Psi_{ij} \Psi_{i'j}^* \qquad \rho_{jj'}^{E'} = \sum_i \Psi_{ij} \Psi_{ij'}^*, \tag{4.6}$$

or in matrix form

$$\rho^{S'} = \Psi\Psi^\dagger \qquad \rho^{E'} = \Psi^T \Psi^*. \tag{4.7}$$

Notice that they are hermitian matrices of dimensions $M_{S'} \times M_{S'}$ and $M_{E'} \times M_{E'}$, which can be exactly diagonalized easily. Both matrices have the exact same spectrum of at most $\min(M^{S'}, M^{E'})$[1] nonzero eigenvalues d_α and can be written in terms

---

[1] For the infinite size algorithm we always have $M^{S'} = M^{E'}$, but this will generally not be the case for the finite size algorithm. For the sake of generality, we will already consider this case here.

of an eigen decomposition as

$$\rho_{ij}^{S'} = \sum_{\alpha} U_{i\alpha} d_\alpha U_{\alpha j}^{\dagger} \tag{4.8}$$

$$\rho_{ij}^{E'} = \sum_{\alpha} V_{i\alpha} d_\alpha V_{\alpha j}^{\dagger}, \tag{4.9}$$

with U, V unitary matrices containing the eigenvectors of $\rho^{S'}$ and $\rho^{E'}$ respectively. Their eigenvalues sum up to unity $\sum_\alpha d_\alpha = 1$ if the superblock ground state was properly normalized, i.e. each block is in state $U^{(\alpha)}$ and $V^{(\alpha)}$ with a probability $d_\alpha < 1$. The matrices U and V represent basis transformations onto the eigenbases of the reduced density operators and we will use them to transform all relevant operators, such as the block Hamiltonians and the surface spin matrices to this new basis sets (see below).

However, if $M^{S'}, M^{E'} > m$, we will only use the first m eigenvectors of U and V, corresponding to the m largest eigenvalues of the density operators. We are thus projecting onto the m eigenstates of the respective reduced density operators contributing the most to the superblock ground state, avoiding an exponential growth of Hilbert space dimensions. This truncation means that the transformation is not exact anymore and represents thus an approximation. The quadratic norm of the deviation of the approximate state $|\tilde{\Psi}\rangle$ from the exact state $|\Psi\rangle$ is controlled by the *discarded weight* ϵ (cf. e.g. [25, 1])

$$\epsilon = \Big| |\Psi\rangle - |\tilde{\Psi}\rangle \Big|^2 = 1 - \sum_{\alpha=1}^{m} d_\alpha \tag{4.10}$$

Thus, if the weights d_α decay fast enough, the approximation is very good. This is usually the case for systems not close to critical points, where the d_α will generally decay exponentially and ϵ is usually of the order $\mathcal{O}(10^{-10})$ or lower. This truncated basis transformation is the heart of success of the DMRG method, since it represents an optimal renormalization scheme for representing the states of S' and E' as part of the system as a whole. In the case $M^{S'} < m$ and/or $M^{E'} < m$ no truncation is necessary and the basis transformation does not correspond to an information loss. We will include this case (e.g. in the first few steps of the iteration) and call $N^{S'} = \min(M^{S'}, m)$ and $N^{E'} = \min(M^{E'}, m)$.

We are therefore left with transformation matrices U^{tr}, V^{tr} of dimensions $dN^S \times N^{S'}$ and $dN^E \times N^{E'}$ respectively, where ^{tr} denotes the truncated version of the matrices. They represent reduced basis transformations to the new block basis sets (cf. also Section 3.3 and Figure 4.2)

$$|a_{\ell+1}^{S'}\rangle = \sum_{a_\ell^S \sigma_{\ell+1}^S} U^{tr}_{(a_\ell^S \sigma_{\ell+1}^S)(a_{\ell+1}^{S'})} \, |a_\ell^S \sigma_{\ell+1}^S\rangle \tag{4.11}$$

$$|a_{\ell+1}^{E'}\rangle = \sum_{a_\ell^E \sigma_{\ell+1}^E} V^{tr}_{(a_\ell^E \sigma_{\ell+1}^E)(a_{\ell+1}^{E'})} \, |a_\ell^E \sigma_{\ell+1}^E\rangle \, . \tag{4.12}$$

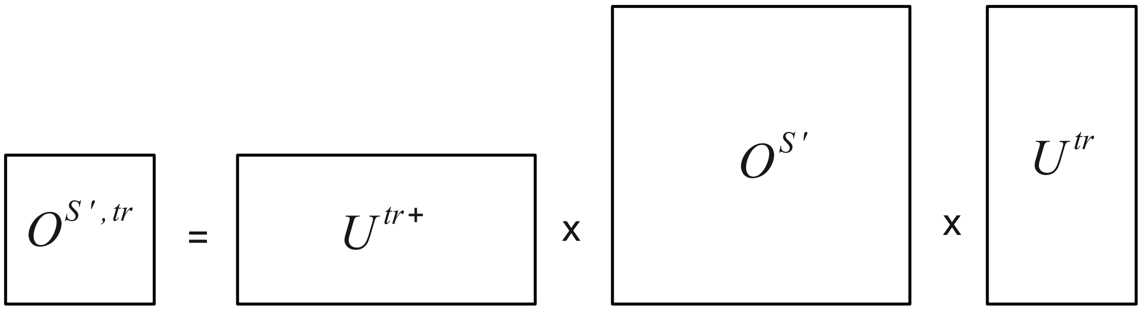

Figure 4.2.: Renormalization Group (RG) transformation for block S'. For every relevant operator, transform to the truncated Hilbert space of reduced dimension, using (4.11). RG-transformation for block E' works the same according to (4.12).

(4) Transform the block Hamiltonians and all relevant operators in blocks S' and E' according to this reduced basis transformations

$$O^{S',tr} = U^{tr\dagger} O^{S'} U^{tr} \qquad\qquad O^{E',tr} = V^{tr\dagger} O^{E'} V^{tr}. \tag{4.13}$$

The transformed and truncated matrices are now of dimensions $N^{S'} \times N^{S'}$ and $N^{E'} \times N^{E'}$. Use these renormalized matrix representations of operators for block enlargement in the next DMRG step.

(5) Call $S = S', E = E'$ and $\ell = \ell'$, go back to (1) and iterate or stop if $\ell = L/2$.

After the last step we have an approximate description of the Hamiltonian for the L-site system in a reduced Hilbert space, given by the last superblock Hamiltonian $H^B = H^{S'}_{\frac{L}{2}} + \hat{H}^{E'}_{\frac{L}{2}}$ and for the ground state, given by the last superblock ground state.

Remarks and Relation to MPS

- Forming and diagonalizing the reduced density operators corresponds to a Schmidt decomposition of the superblock ground state, which is calculated by performing an SVD of Ψ_{ij} in (4.5) (cf. also Section 3.3)

$$\Psi_{ij} = \sum_\alpha P_{i\alpha} \lambda_\alpha Q^\dagger_{\alpha j} \tag{4.14}$$

$$|\Psi\rangle = \sum_\alpha \lambda_\alpha \left(\sum_i P_{i\alpha} |i\rangle \right) \left(\sum_j Q^*_{j\alpha} |j\rangle \right) = \sum_\alpha \lambda_\alpha |\phi^{S'}_\alpha\rangle |\phi^{E'}_\alpha\rangle \tag{4.15}$$

with P, Q again unitaries and $|\phi^{S'}_\alpha\rangle$ and $|\phi^{E'}_\alpha\rangle$ the left and right Schmidt vectors. λ_α is a diagonal matrix, containing the (real) singular values of Ψ. They correspond to the eigenvalues of $\rho^{S'/E'}$ via $\lambda_\alpha = \sqrt{d_\alpha}$ and we can also identify $P = U$ as well as $Q^* = V$. This can be seen by considering

$$\rho^{S'} \overset{(4.14)}{=} \Psi\Psi^\dagger = P\lambda \underbrace{Q^\dagger Q}_{\mathbb{1}} \lambda P^\dagger = P\lambda^2 P^\dagger \overset{(4.8)}{=} UdU^\dagger \tag{4.16}$$

$$\rho^{E'} \overset{(4.14)}{=} \Psi^T\Psi^* = Q^*\lambda \underbrace{P^T P^*}_{\mathbb{1}} \lambda Q^T = Q^*\lambda^2 Q^T \overset{(4.9)}{=} VdV^\dagger \tag{4.17}$$

Thus the RG transformation (4.13) transforms onto the Schmidt basis sets of blocks S' and E'.

- In Section 3.3 we have shown that a Schmidt decomposition can be expressed as a mixed canonical MPS in the form of (3.23). We have also shown how to retrieve the reduced density matrices from a Schmidt decomposition in (3.38) and (3.39). We have constructed the mixed canonical representation by using reshaped versions of P and Q and the fact that MPS-matrices correspond to reduced basis transformations. By comparing (3.27) and (3.28) to the RG transformations (4.11) and (4.12) and remembering the fact, that we have constructed the MPS-matrices A and B from an SVD, we can identify, using the above

$$A^{\sigma_\ell^S}_{a^S_{\ell-1} a^S_\ell} = U^{tr}_{(a^S_{\ell-1}\sigma^S_\ell)(a^S_\ell)} \tag{4.18}$$

$$B^{\sigma_\ell^E}_{a^E_\ell a^E_{\ell-1}} = {V^{tr}}^T_{(a^E_\ell)(\sigma^E_\ell a^E_{\ell-1})}. \tag{4.19}$$

  This means that the DMRG algorithm produces mixed canonical MPS per construction due to its iterative nature.

- We can write the final approximate superblock ground state exactly in the form (3.23). The superblock ground state in the reduced Hilbert space is then the 2-site wave function defined for (3.23). This fact was not discovered by Östlund and Rommer [4] until some years after White's proposal of the DMRG algorithm in 1992 [1].

- The set of eigenvalues of the reduced density matrices also describe a measure for the entanglement present between the two blocks via the von Neumann entropy

$$S_{S'E'} = -\operatorname{Tr} \hat\rho^{S'} \log_2 \hat\rho^{S'} = -\operatorname{Tr} \hat\rho^{S'} \log_2 \hat\rho^{S'} \overset{(4.8)(4.9)}{=} -\sum_\alpha d_\alpha \log_2 d_\alpha \tag{4.20}$$

  Thus the truncation prescription of DMRG preserves the maximum amount of entanglement of the blocks with the system, by discarding only the smallest eigenvalues of the reduced density matrices. From this point of view it makes sense to use a setup of 2 interacting blocks S and E, since truncation is controlled by the entanglement between these 2 blocks. Historically, White named block S the system block, which is "embedded" in an environment represented by block E, hence the names.

4.1.2. iDMRG State Prediction and Convergence

The infinite size algorithm described above is a good tool for finding thermodynamic limit ground states of strongly correlated one-dimensional quantum systems. For finite size systems, the finite size algorithm described below gives much better results, however in the infinite case we will see that we can define a good convergence criterion in form of a fixed point relation. In the process we will also find a state prediction scheme to give a much better starting point for the eigensolver to find the superblock ground state. This following reinterpretation of the infinite size algorithm – or iDMRG – and the proposal of a good state prediction (which already existed for the finite size case for some time) was not done until recently by McCulloch [30]. As a matter of fact, other prediction methods for the iDMRG case had been proposed earlier [31], however the following prediction method yields by far the best results, as it can also be used as a tool for forming a convergence criterion.

As we have seen above, iDMRG produces states in the mixed canonical MPS form (3.23) or (3.24). For a translationally invariant infinite size MPS (iMPS) the matrices should be site independent. One should therefore be able to find a 2-site unit cell of MPS matrices and the iMPS is then an infinite repetition of this unit cell.[2] Consider an MPS generated by iDMRG after ℓ steps

$$|\Psi_\ell\rangle = \sum_{\{\sigma\}} A^{\sigma_1^S} \dots A^{\sigma_\ell^S} \lambda^{(\ell)} B^{\sigma_\ell^E} \dots B^{\sigma_1^E} \, |\sigma_1^S \dots \sigma_\ell^S \sigma_\ell^E \dots \sigma_1^E\rangle \tag{4.21}$$

or in its canonical representation

$$|\Psi_\ell\rangle = \sum_{\{\sigma\}} \Gamma^{\sigma_1^S} \lambda^{(1)} \dots \lambda^{(\ell-1)} \Gamma^{\sigma_\ell^S} \lambda^{(\ell)} \Gamma^{\sigma_\ell^E} \lambda^{(\ell-1)} \dots \Gamma^{\sigma_1^E} \, |\sigma_1^S \dots \sigma_\ell^S \sigma_\ell^E \dots \sigma_1^E\rangle \tag{4.22}$$

We now take the central two Γ, λ pairs to define a 2-site unit cell

$$\Phi_{UC}^{\sigma_\ell^S \sigma_\ell^E} = \lambda^{(\ell-1)} \Gamma^{(\ell_S)\sigma_\ell^S} \lambda^{(\ell)} \Gamma^{(\ell_E)\sigma_\ell^E} = A^{(\ell)\sigma_\ell^S} \lambda^{(\ell)} B^{(\ell)\sigma_\ell^E} \left(\lambda^{(\ell-1)}\right)^{-1} , \tag{4.23}$$

where UC stands for *unit cell.* We now have introduced a distinct labeling of A-, B- and Γ-matrices by the site they were originally defined on, with ℓ_S being site ℓ in block S and equivalently for block E.

After a sufficient amount of DMRG iterations the unit cell in the center should be a good description of the infinite system. This of course has to be quantified in form of a convergence criterion, which we will elaborate below. Suppose iDMRG has reached convergence, then the unit cell (4.23) is sufficient to describe the translationally invariant ground state of the infinite system in form of an iMPS

$$|\Psi\rangle = \sum_{\sigma_{-\infty} \dots \sigma_{\infty}} \left(\prod_{i=-\infty}^{\infty} \Phi_{UC}^{\sigma_{2i-1}\sigma_{2i}} \right) |\sigma_{-\infty} \dots \sigma_{\infty}\rangle \, . \tag{4.24}$$

---

[2] Actually, an iMPS which is invariant under translation by one site requires only a 1-site unit cell its description. However, for iDMRG state prediction we need a 2-site unit cell, since 2 sites are inserted in every iDMRG step (see below).

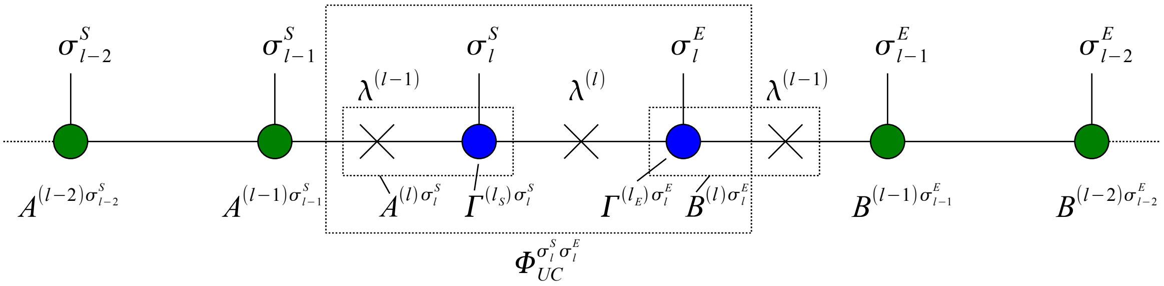

Figure 4.3.: Construction of a 2-site unit cell for state prediction in the next iDMRG step, using the central part of the MPS in the current step. A- and B-matrices are depicted in green, Γ-matrices in blue, for which position l is also classified by block, with l_S being site l in block S and equivalently for block E.

Notice that we only need 2 distinct Γ and λ matrices to describe the entire iMPS. Also, since we will use the same matrices on different sites, we have introduced a distinct labeling for MPS matrices, just like for λ-matrices. Notice also that we can relate $\Phi^{\sigma^S_\ell\sigma^E_\ell}_{UC}$ to the 2-site wave function in (3.23) via

$$\Psi^{\sigma^S_\ell\sigma^E_\ell} = \Phi^{\sigma^S_\ell\sigma^E_\ell}_{UC}\lambda^{(\ell-1)}. \tag{4.25}$$

Now in each DMRG step we insert 2 sites between S and E, effectively adding 2 sites to the system. In standard iDMRG one would now construct the block Hamiltonian and compute its ground state from scratch, i.e. use a some (generally random) initial vector for the iterative eigensolver. In terms of faster convergence and better algorithm performance it would be convenient to have a good estimate for the ground state of the *enlarged* superblock. Recall that the superblock ground state is computed by the eigensolver in the reduced Hilbert space and corresponds thus exactly to the 2-site wave function defined in (3.23). We now approximate the superblock ground state for the enlarged system by inserting the center unit cell of the ℓ-site system (4.21) once more into (4.21) as a repetition of the center part to give

$$\begin{aligned}|\tilde{\Psi}_{\ell+1}\rangle = &\sum_{\{\sigma\}} A^{(1)\sigma^S_1}\dots A^{(\ell-1)\sigma^S_{\ell-1}}\left(A^{(\ell)\sigma^S_\ell}\lambda^{(\ell)}B^{(\ell)\sigma^S_{\ell+1}}\left(\lambda^{(\ell-1)}\right)^{-1}\right)\times\\ &\left(A^{(\ell)\sigma^E_{\ell+1}}\lambda^{(\ell)}B^{(\ell)\sigma^E_\ell}\left(\lambda^{(\ell-1)}\right)^{-1}\right)\lambda^{(\ell-1)}B^{(\ell-1)\sigma^E_{\ell-1}}\dots B^{\sigma^E_1}\,|\sigma^S_1\dots\sigma^S_{\ell+1}\sigma^E_{\ell+1}\dots\sigma^E_1\rangle\,.\end{aligned} \tag{4.26}$$

Notice that we now have matrices sitting on different sites than where they were originally defined. This is because we have not split up the originally defined unit cell to insert the new sites in the center, but rather inserted the new unit cell next to the old one. This follows the presumption, that in the thermodynamic limit the iMPS is just an

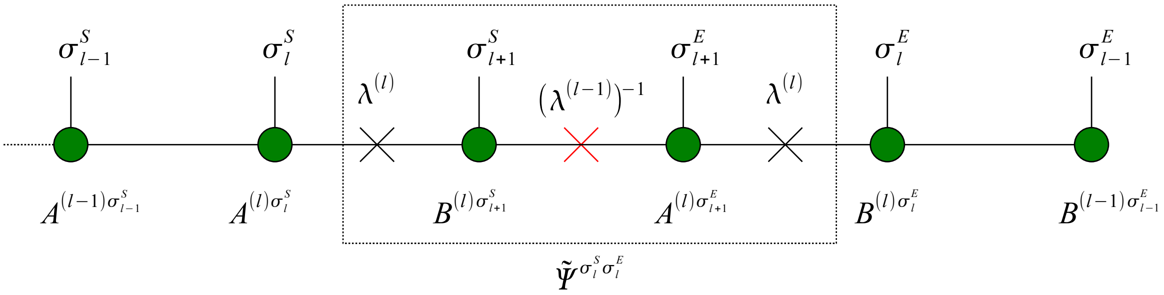

Figure 4.4.: Extraction of an initial guess for the 2-site wave function after inserting the 2-site unit cell to generate an MPS containing 2 additional sites. Notice that there are now A matrices sitting on the right and B matrices sitting on the left of the center.

infinite repetition of this unit cell. We can now, re-bracket and identify a good initial guess for the 2-site wave function for the enlarged system

$$\begin{aligned}|\tilde\Psi_{\ell+1}\rangle = &\sum_{\{\sigma\}} A^{(1)\sigma^S_1}\dots A^{(\ell)\sigma^S_\ell}\underbrace{\left(\lambda^{(\ell)}B^{(\ell)\sigma^S_{\ell+1}}\left(\lambda^{(\ell-1)}\right)^{-1}A^{(\ell)\sigma^E_{\ell+1}}\lambda^{(\ell)}\right)}_{\tilde\Psi^{\sigma^S_{\ell+1}\sigma^E_{\ell+1}}}\times\\ &B^{(\ell-1)\sigma^E_{\ell-1}}\dots B^{\sigma^E_1}\,|\sigma^S_1\dots\sigma^S_{\ell+1}\sigma^E_{\ell+1}\dots\sigma^E_1\rangle\,,\end{aligned}\tag{4.27}$$

where

$$\tilde\Psi^{\sigma^S_{\ell+1}\sigma^E_{\ell+1}} = \lambda^{(\ell)}B^{(\ell)\sigma^S_{\ell+1}}\left(\lambda^{(\ell-1)}\right)^{-1}A^{(\ell)\sigma^E_{\ell+1}}\lambda^{(\ell)} = \lambda^{(\ell)}\Gamma^{(\ell_E)\sigma^S_{\ell+1}}\lambda^{(\ell-1)}\Gamma^{(\ell_S)\sigma^E_{\ell+1}}\lambda^{(\ell)}\tag{4.28}$$

is now a good initial guess for the eigensolver (cf. Figure 4.4). This is especially the case for already large chains, where the MPS structure is already close to the translationally invariant iMPS structure. However, this also works well for small chains, where the state structure is still far from translationally invariant since the above state prediction is still much better than a random initial vector and leads to a huge overall speedup in iDMRG.

At last we need a good convergence criterion to check if iDMRG has indeed produced a translationally invariant thermodynamic limit ground state. The fixed point relation we will be using is just the formulation of the left normalization condition for MPS-matrices in terms of reduced density operators (3.55)[3] This relation is strictly defined for finite size MPS matrices only. In the iDMRG case the matrices are defined on chains of different length, the relationship however holds again in the thermodynamic limit, for which we then *demand*

$$\rho_S^{(\ell-1)} \overset{!}{=} \sum_{\sigma_\ell} A^{\sigma^S_\ell}\rho_S^{(\ell)}A^{\sigma^S_\ell\dagger}\tag{4.29}$$

---

[3] The convergence criterion using the right normalization condition (3.54) can be derived in a similar way.

We will now combine $A^{\sigma_\ell^S}\lambda^{(\ell)} = M^{\sigma_\ell^S}$, decompose via SVD into $M^{\sigma_\ell^S} = UDV^{\sigma_\ell^S\dagger}$ and redefine $V^{\sigma_\ell^S\dagger} = B^{\sigma_\ell^S}$ and $UD = \Lambda_L^{(\ell-1)}$ to give

$$A^{\sigma_\ell^S}\lambda^{(\ell)} = UDV^{\sigma_\ell^S\dagger} = \Lambda_L^{(\ell-1)}B^{\sigma_\ell^S}. \tag{4.30}$$

Notice that $\Lambda_L^{(\ell-1)}$ is not a diagonal matrix and the identity (3.51) does in general not hold here, which stems from the following fact. In each iDMRG step, where the 2-site wave function is first computed using an iterative eigen solver and then decomposed as

$$\Psi^{\sigma_\ell^S\sigma_\ell^E}_{a_{\ell-1}^S a_{\ell-1}^E} = \sum_{a_\ell} A^{\sigma_\ell^S}_{a_{\ell-1}^S a_\ell}\lambda^{(\ell)}_{a_\ell}B^{\sigma_\ell^E}_{a_\ell a_{\ell-1}^E}, \tag{4.31}$$

the basis $\{|a_\ell\rangle\}$ is the eigen basis of the reduced density matrices $\rho^{(\ell)}_{S,E}$, hence $\rho^{(\ell)}_{S,E} = \lambda^{(\ell)2}$ in this basis. The basis sets $\{|a^S_{\ell-1}\rangle\}$ and $\{|a^E_{\ell-1}\rangle\}$ however are in general not the same basis sets and also not the eigen bases of the reduced density matrices $\rho^{(\ell-1)}_{S,E}$ from the last step. One way to transform these basis sets (and thus the matrices $A^{\sigma_\ell^S}$ and $B^{\sigma_\ell^E}$) to the eigen basis of $\rho^{(\ell-1)}_{S,E}$, while preserving the normalization conditions (3.18) and (3.19), is the canonization procedure described in Appendix A.1. For the interpretation of this procedure in terms of A- and B-matrices see also [30].

This canonization procedure is however not necessary here if we use (4.30) to extract $B^{\sigma_\ell^S}$ from $A^{\sigma_\ell^S}$ and $\lambda^{(\ell)}$. Using $\rho^{(\ell)}_S = \lambda^{(\ell)2}$ (see above) and inserting (4.30) into (4.29) gives

$$\sum_{\sigma_\ell} A^{\sigma_\ell}\rho^{(\ell)}_S A^{\sigma_\ell\dagger} = \sum_{\sigma_\ell} A^{\sigma_\ell}\lambda^{(\ell)2}A^{\sigma_\ell\dagger} = \Lambda^\ell_L \underbrace{\sum_{\sigma_\ell} B^{\sigma_\ell}B^{\sigma_\ell\dagger}}_{\mathbb{1}} \Lambda^{\ell\dagger}_L = \Lambda^\ell_L\Lambda^{\ell\dagger}_L =: \rho^{(\ell)}_L \tag{4.32}$$

Thus the fixed point relation becomes

$$\rho^{(\ell-1)}_S \overset{!}{=} \rho^{(\ell)}_L. \tag{4.33}$$

As this relation will never be fulfilled exactly in numerical simulations, we want the two density matrices in (4.33) to become as close to each other as possible. The closeness of the 2 density matrices can be quantified by the *orthogonality fidelity* [30, 32]

$$F\left(\rho^{(\ell-1)}_S, \rho^{(\ell)}_L\right) = \mathrm{Tr}\sqrt{\sqrt{\rho^{(\ell-1)}_S}\rho^{(\ell)}_L\sqrt{\rho^{(\ell-1)}_S}} = \left\|\sqrt{\rho^{(\ell)}_L}\sqrt{\rho^{(\ell-1)}_S}\right\|_{tr}, \tag{4.34}$$

where $\|\ldots\|_{tr}$ is the trace norm, defined as the sum over the argument's singular values. Using this form of the fidelity we get $F = \sum_i d_i$ with d_i the singular values of $\Lambda^\ell_L\lambda^{(\ell-1)}$. It holds that $0 \le F \le 1$ and the fidelity is 1 if and only if the two density matrices are identical. We can therefore use the quantity $1 - F$ as a good convergence criterion and ask that it drops below a certain threshold. At this point iDMRG has converged by fulfilling (4.33) to a certain accuracy and the current MPS matrices $A^{\sigma_\ell^S}$ and $B^{\sigma_\ell^E}$

are good MPS matrices together with the current Schmidt values $\lambda^{(\ell)}$, to describe the translationally invariant iMPS of the infinite system. For further references see [30, 25].

The converged $A^{\sigma_\ell^S}$ and $B^{\sigma_\ell^E}$ and $\lambda^{(\ell)}$ can be used to define an iMPS unit cell for subsequent simulations, such as time evolution for infinite systems (cf. Section 4.2.4) or the Comoving Window method (cf. Section 5). One can define a canonical iMPS unit cell $\{\Gamma^A, \lambda^{(A)}, \Gamma^B, \lambda^{(B)}\}$, where e.g.

$$\lambda^{(A)} = \lambda^{(\ell)} \qquad \Gamma^A = {\lambda^{(\ell-1)}}^{-1} A^{\sigma_\ell^S} \tag{4.35}$$

$$\lambda^{(B)} = \lambda^{(\ell-1)} \qquad \Gamma^B = B^{\sigma_\ell^E} {\lambda^{(\ell-1)}}^{-1}. \tag{4.36}$$

The resulting Γ- and λ-matrices will in general not fulfill both left and right normalization conditions (3.49) and (3.50) due to the reason explained above. A way to properly canonize an arbitrary, but normed iMPS is described in Appendix A.1.

4.1.3. Finite Size DMRG

For many finite systems, infinite size DMRG doesn't yield satisfactory results, as in its first few iterations, the system is still dominated by boundary effects. Thus the boundary strongly affects the bulk behavior of the resulting state, but not vice versa. One can say the system is not yet properly "thermalized". The finite size DMRG algorithm presents a method to further improve the infinite size DMRG ansatz for finite systems to account for this problem. Starting point is the superblock ground state in its MPS form for L sites. Finite size DMRG will further increase the quality of the ground state MPS matrices by successive sweeps through all sites of the system, further increasing the accuracy of the ground state. For this purpose, all blocks of all sizes for S and E and their matrix representations for operators and MPS matrices must be stored.

The initial setup for one sweep is the last superblock configuration $SE = S' \bullet \bullet E'$ from infinite size DMRG, with E and S of equal size ℓ and $2\ell = L$.

(1) Enlarge block S of size ℓ by adding one site, forming S' of size $\ell + 1$. At the same time, "shrink" block E by regenerating E' from a previously stored block E of size $\ell - 2$, enlarged by one site to size $\ell - 1$. Block enlargement is done according to step (1) of Section 4.1.1.

(2) Proceed with steps (2) - (4) of Section 4.1.1, but only calculate the updated left normalized MPS matrix $A^{\sigma_{\ell+1}}$ and apply RG transformations only for block S'. Call $S = S'$ and repeat this step until block E has reached a minimal size (usually until matrix dimensions are smaller than m).

(3) Reverse the procedure of the above steps (1) and (2) by enlarging E and shrinking S, this time only calculating the updated right normalized MPS matrices $B^{\sigma_{\ell+1}}$ and applying RG transformations for block E'. Again, repeat this step until S has reached a minimal size.

(4) Once more, reverse the above process and repeat steps (1) and (2) until the initial configuration $S \bullet \bullet E$ with blocks E and S of equal size ℓ is reached again.

Steps (1) - (4) are called a finite size DMRG sweep (cf. Figure 4.5). As a convergence criterion one could watch the overall energy or other observables such as local magnetizations. For slightly entangled systems far away from critical points, usually 2 sweeps are enough, but this also depends on the number of kept states m.

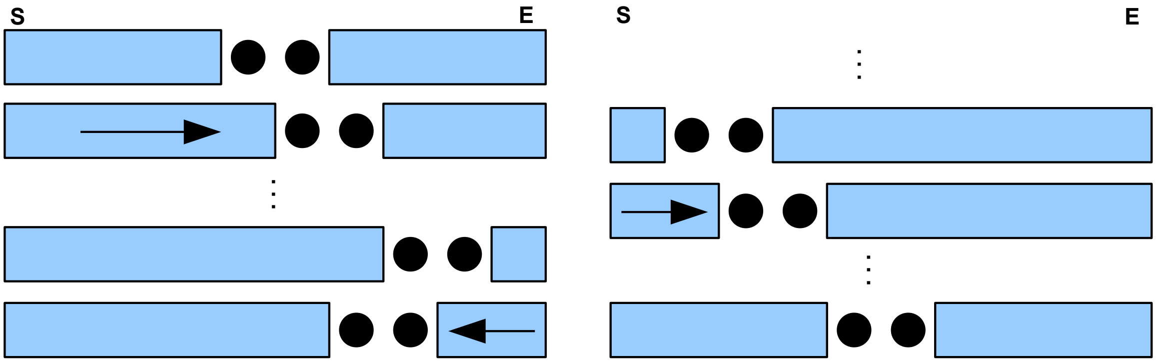

Figure 4.5.: One full DMRG sweep. Block S grows while E shrinks until E reaches a minimal size. The process is reversed until S reaches minimal size. Again the process is reversed until both blocks are of the same size again.

Prediction algorithm

Similar to the iDMRG case there exists a prediction algorithm to get a good initial guess for the 2-site wave function in each DMRG step [33]. Actually, this prediction method was proposed much earlier than for the iDMRG case. The basic idea is to "shift" the representation of the current 2-site wave function 1 site to the right or to the left, depending on the current position in the sweep, to give a good initial guess for the iterative eigensolver in the next step.

Regard the same finite size MPS in two distinct mixed-canonical representations (3.23), with the 2-site wave functions being on sites $j-1, j$ and $j, j+1$ respectively. Both MPS only differ in their representation on sites $j-1, j$ and $j+1$. Thus, by setting these 2 parts equal we get

$$\Psi^{\sigma_{j-1}\sigma_j} B^{\sigma_{j+1}} = A^{\sigma_{j-1}} \Psi^{\sigma_j \sigma_{j+1}} \tag{4.37}$$

Exploiting the normalization conditions of MPS matrices we can shift the 2-site wave function to the left and to the right by

$$\Psi^{\sigma_{j-1}\sigma_j} = \sum_{\sigma_{j+1}} A^{\sigma_{j-1}} \Psi^{\sigma_j \sigma_{j+1}} B^{\sigma_{j+1}\dagger} \tag{4.38}$$

$$\Psi^{\sigma_j \sigma_{j+1}} = \sum_{\sigma_{j-1}} A^{\sigma_{j-1}\dagger} \Psi^{\sigma_{j-1}\sigma_j} B^{\sigma_{j+1}} \tag{4.39}$$

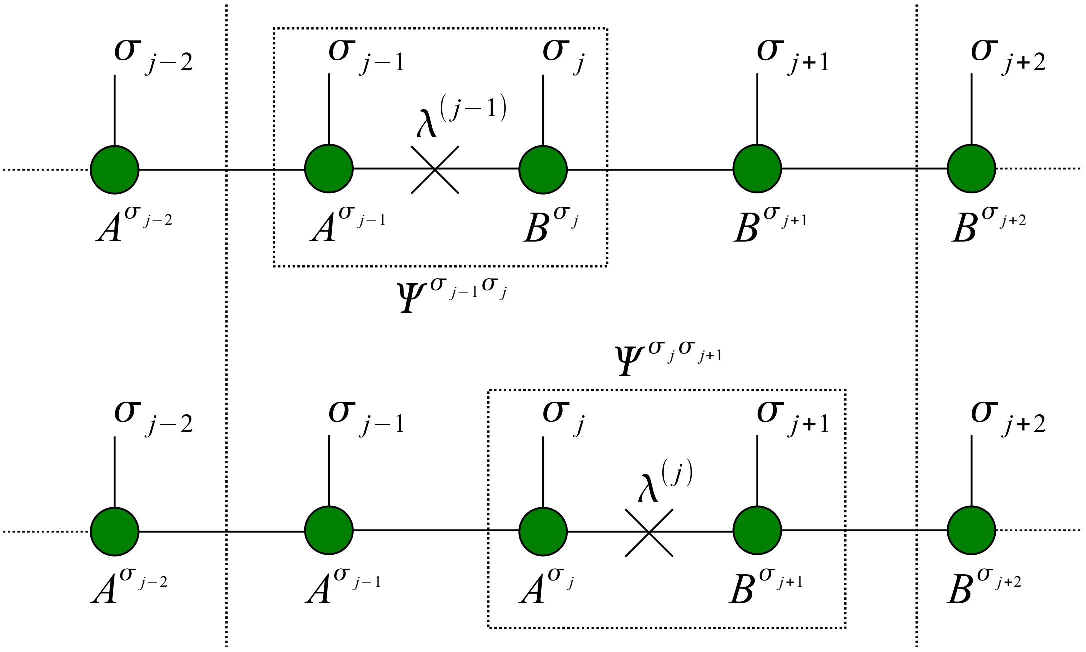

Figure 4.6.: Graphical representation of finite size DMRG state prediction. Consider two equivalent mixed-canonical MPS representations with their 2-site wave functions on sites $j-1, j$ and $j, j+1$ respectively. The representations only differ on sites $j-1, j, j+1$ (in between the two vertical dashed lines). Setting both parts equal and exploiting normalization conditions gives a method to shift the 2-site wave function to the left and to the right.

4.2. Time Evolution using MPS

Cazalilla and Marston were the first to propose time evolution using DMRG results [34]. Their approach was to use a fixed point Hamiltonian and its ground state generated by iDMRG, adding a time dependent perturbation to the Hamiltonian and integrating the time dependent Schrödinger equation (4.40) numerically. This approach is not optimal, since the reduced Hilbert space generated by DMRG is not optimal for the resulting excited state after a short period of time and this state will generally have its main contributions from different parts of the total Hilbert space. This approach thus represents a *non-adaptive* MPS time evolution method. Its accuracy breaks down fairly quickly depending on the excitation. In the following years however, two very powerful *adaptive* time evolution methods were proposed: TEBD [2] and shortly thereafter tDMRG [3]. They are both mathematically equivalent, but differ in their numerical implementation, both having advantages and disadvantages. They both rely on the Suzuki-Trotter decomposition (see below) and deliver the time evolution of the total system in discrete time steps τ, while constantly adapting the reduced Hilbert space in order to optimally approximate the true time dependent quantum state.

4.2.1. The Suzuki-Trotter Decomposition

Time evolution of quantum mechanical states is governed by the time dependent Schrödinger equation

$$i\frac{\partial}{\partial t}\left|\Psi(t)\right\rangle = \hat{H}\left|\Psi(t)\right\rangle, \tag{4.40}$$

with $\left|\Psi(t)\right\rangle$ the time dependent state of the system and $\hat{H}$ the system Hamiltonian. In terms of the time evolution operator $\hat{U}$, the above equation can be written as

$$i\frac{\partial}{\partial t}\hat{U}(t) = \hat{H}\hat{U}(t), \tag{4.41}$$

$$\left|\Psi(t)\right\rangle = \hat{U}(t)\left|\Psi(0)\right\rangle. \tag{4.42}$$

In the case of not explicitly time dependent Hamiltonians, the solution to (4.41) for $\hat{U}(t)$ is

$$\hat{U}(t) = e^{-it\hat{H}}. \tag{4.43}$$

The time evolution can be split up into an arbitrary amount of sequential time evolutions of smaller time intervals, e.g. in N equally spaced intervals τ

$$\hat{U}(t) = e^{-it\hat{H}} = \left(e^{-i\tau\hat{H}}\right)^{N} = \hat{U}(\tau)^{N}, \tag{4.44}$$

with $N = \frac{t}{\tau}$.

Furthermore, consider Hamiltonians of an L-site lattice with L even, consisting of nearest neighbor interactions only, giving $\hat{H} = \sum_i \hat{h}_{j,j+1}$, with $\hat{h}_{j,j+1}$ 2-site Hamiltonians, connecting sites $j, j+1$. In general, these 2-site Hamiltonian will not commute with one another, therefore a straight forward decomposition of (4.43) in a product of exponentials of 2-site Hamiltonians is not possible. However, it can be approximately decomposed using the Suzuki-Trotter decomposition of first order [35]

$$\hat{U}(\tau) = e^{-i\tau\hat{H}} = e^{-i\tau\hat{H}_o}e^{-i\tau\hat{H}_e} + \mathcal{O}\left(\tau^2\right) \tag{4.45}$$

with $\hat{H} = \hat{H}_o + \hat{H}_e$ and $\hat{H}_o$ and $\hat{H}_e$ the parts of the overall Hamiltonian containing only odd and even bonds respectively

$$\hat{H}_o = \sum_{j=1}^{\frac{L}{2}} \hat{h}_{2j-1,2j}, \qquad \hat{H}_e = \sum_{j=1}^{\frac{L}{2}-1} \hat{h}_{2j,2j+1}. \tag{4.46}$$

Applying $\hat{U}(\tau)$ in (4.45) $N = \frac{t}{\tau}$ times to perform time evolution up to t according to (4.44) costs one order of τ for the approximation error (cf. [35])

$$\hat{U}(t) = \hat{U}(\tau)^{N} = \left(e^{-i\tau\hat{H}_o}e^{-i\tau\hat{H}_e}\right)^{N} + \mathcal{O}\left(\tau\right) \tag{4.47}$$

Since all 2-site Hamiltonians in $\hat{H}_o$ and $\hat{H}_e$ commute with each other respectively, one can now exactly decompose $\hat{H}_o$ and $\hat{H}_e$ into a product of 2-site time evolution operators

$$\hat{U}_o(\tau) = e^{-i\tau\hat{H}_o} = \bigotimes_{j=1}^{\frac{L}{2}} e^{-i\tau\hat{h}_{2j-1,2j}} = \bigotimes_{j=1}^{\frac{L}{2}} \hat{u}_{2j-1,2j}(\tau) \tag{4.48}$$

$$\hat{U}_e(\tau) = e^{-i\tau\hat{H}_e} = \bigotimes_{j=1}^{\frac{L}{2}-1} e^{-i\tau\hat{h}_{2j,2j+1}} = \bigotimes_{j=1}^{\frac{L}{2}-1} \hat{u}_{2j,2j+1}(\tau), \tag{4.49}$$

where we have defined $\hat{u}_{j,j+1}(\tau) = e^{-i\tau\hat{h}_{j,j+1}}$. As can be seen from (4.45), the approximation error for a small interval τ is of the order $\mathcal{O}(\tau^2)$. With τ sufficiently small, this error can be kept very small, even for first order. Higher orders of the Suzuki-Trotter decomposition yield better behavior of the time step error, but require a more sophisticated decomposition structure, however second order decomposition is still very similar to first order

$$\hat{U}(\tau) = e^{-i\tau\hat{H}} = e^{-i\frac{\tau}{2}\hat{H}_o} e^{-i\tau\hat{H}_e} e^{-i\frac{\tau}{2}\hat{H}_o} + \mathcal{O}\left(\tau^3\right). \tag{4.50}$$

Especially when measurements are performed every n steps, the intermediate time steps technically become first order, since $\hat{U}_o(\frac{\tau}{2})\hat{U}_o(\frac{\tau}{2}) = \hat{U}_o(\tau)$. When using second order, start with an initial odd update $\hat{U}_o(\frac{\tau}{2})$. Then perform first order like even and odd bond updates in full time steps τ until step n, where one performs one half time odd update $\hat{U}_o(\frac{\tau}{2})$ before measuring and one half time odd update $\hat{U}_o(\frac{\tau}{2})$ after measuring. As one can see, computational effort is hardly increased, whereas one gains one order of τ in accuracy.

In the following, only first and second order Suzuki-Trotter decomposition is considered.

4.2.2. Time Evolving Block Decimation (TEBD)

Proposed by Vidal in 2003, TEBD was the first *adaptive* time evolution algorithm using MPS [2]. It first introduced the canonical representation of MPS described in Section 3.4. Its focus on easy access to all possible Schmidt decompositions of the system is most suitable for the task of Suzuki-Trotter like time evolutions. The algorithm generally provides a method for updating a finite size MPS after applying 1- or 2-site unitary operators onto it. However, it is especially tailored for evolving a quantum mechanical state in MPS form in time, i.e. it provides an efficient method for applying the Suzuki-Trotter time evolution operator to a finite size MPS.

The basic concept is to deliver time evolution up to time t by applying $\hat{U}(\tau)$ sequentially to an initial state in *canonical MPS form* (cf. Section 3.4) for N times, adapting reduced Hilbert spaces on each bond at every step. This ensures an optimal approximation of the state at all times, given a certain finite matrix dimension m throughout the time evolution process.[4] For first order Suzuki-Trotter decomposition, one Trotter time

---

[4] TEBD language uses the Greek letter χ for the matrix dimension m.

step consists of first applying $\hat{U}_o(\tau)$ to all odd bonds and then $\hat{U}_e(\tau)$ to all even bonds (or vice versa). For a graphical representation see Figure 4.7.

(1) Start with odd bonds and set $j = 1$.

(2) To apply $\hat{u}_{j,j+1}$ to bond $j, j+1$ construct the 2-site wave function according to (3.52)

$$\Psi^{\sigma_j \sigma_{j+1}} = \lambda^{(j-1)} \Gamma^{\sigma_j} \lambda^{(j)} \Gamma^{\sigma_{j+1}} \lambda^{(j+1)}, \tag{4.51}$$

with $\lambda^{(0)} = \lambda^{(L)} = 1$.

(3) $\hat{u}_{j,j+1}$ has matrix representation $u^{\sigma_j \sigma_{j+1}}_{\sigma'_j \sigma'_{j+1}}$ in the local 2-site Hilbert space. Apply this time evolution matrix to $\Psi^{\sigma_j \sigma_{j+1}}$ to get

$$\tilde{\Psi}^{\sigma_j \sigma_{j+1}} = \sum_{\sigma'_j \sigma'_{j+1}} u^{\sigma_j \sigma_{j+1}}_{\sigma'_j \sigma'_{j+1}} \Psi^{\sigma'_j \sigma'_{j+1}}. \tag{4.52}$$

(4) In Reference [2] it is shown, that applying a unitary 2-site operator on neighboring sites $j, j+1$ only requires updating the connecting Schmidt values $\lambda^{(j)}$ and the matrices on both sites Γ^{σ_j} and $\Gamma^{\sigma_{j+1}}$. We therefore need to extract the updated versions $\tilde{\lambda}^{(j)}$, $\bar{\Gamma}^{\sigma_{j+1}}$ and $\bar{\Gamma}^{\sigma_{j+1}}$ from (4.52), while $\lambda^{(j-1)}$ and $\lambda^{(j+1)}$ remain unaffected by this step. We can do this by recomputing the Schmidt decomposition at the current bond using an SVD

$$\tilde{\Psi}^{\sigma_j \sigma_{j+1}} = U^{\sigma_j} \tilde{\lambda}^{(j)} V^{\sigma_{j+1} \dagger}, \tag{4.53}$$

which immediately gives us the updated Schmidt values $\tilde{\lambda}^{(j)}$. Notice that both MPS matrices are not fully evolved by one time step yet, since they each lack an update "from the other side". We will extract $\tilde{\Gamma}^{\sigma_{j+1}}$ and $\tilde{\Gamma}^{\sigma_{j+1}}$ by dividing out the Schmidt values $\lambda^{(j-1)}$ and $\lambda^{(j+1)}$, which we included to form $\Psi^{\sigma_j \sigma_{j+1}}$ in the beginning

$$\tilde{\Gamma}^{\sigma_j} = {\lambda^{(j-1)}}^{-1} U^{\sigma_j} \tag{4.54}$$

$$\tilde{\Gamma}^{\sigma_{j+1}} = V^{\sigma_{j+1} \dagger} {\lambda^{(j+1)}}^{-1}. \tag{4.55}$$

As mentioned above, $\lambda^{(j-1)}$ and $\lambda^{(j+1)}$ are not affected by the application of $\hat{u}_{i,i+1}$. However, we need them to preserve the proper normalization conditions for $\tilde{\Gamma}^{\sigma_j}$ and $\tilde{\Gamma}^{\sigma_{j+1}}$, since U^{σ_j} is left-normalized and $V^{\sigma_{j+1} \dagger}$ right-normalized per construction. This concludes the update for the current bond $j, j+1$. Set $j \to j+2$

(5) Repeat steps (2) - (4) while $j < N$, i.e. for all odd bonds

(6) After updating all odd bonds, switch to even bonds by setting $j = 2$ and repeating steps (2) - (4) while $j < N$, i.e. for all even bonds. This concludes one full Trotter time step, i.e. one application of $\hat{U}(\tau)$.

Full time evolution up to time t is achieved by applying the above procedure N times to the initial state. Measurements can be carried out after each Trotter step or every few Trotter steps, yielding an observable time line.

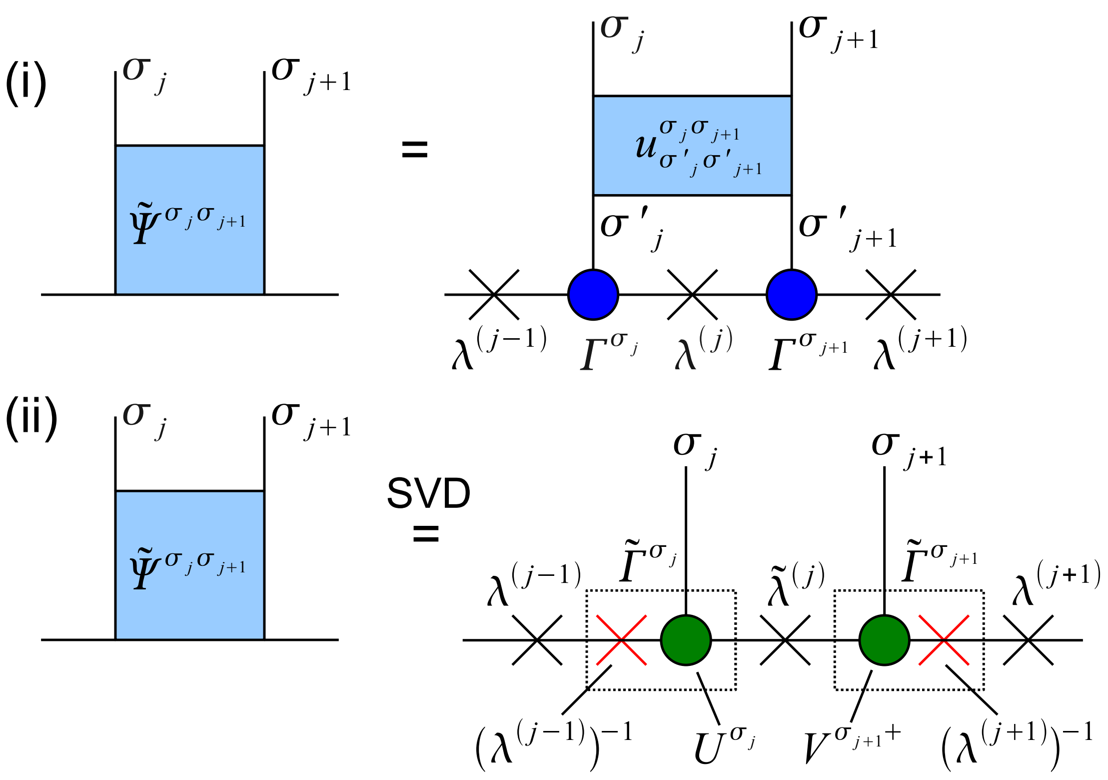

Figure 4.7.: TEBD update for a single bond. (i) Form the 2-site wave function $\Psi^{\sigma_j\sigma_{j+1}}$ and apply the 2-site time evolution operator $u^{\sigma_j\sigma_{j+1}}_{\sigma'_j\sigma'_{j+1}}$ to get $\tilde{\Psi}^{\sigma_j\sigma_{j+1}}$. (ii) Decompose via SVD to get $\tilde{\Psi}^{\sigma_j\sigma_{j+1}} = U^{\sigma_j}\tilde{\lambda}^{(j)}V^{\sigma_{j+1}\dagger}$ and extract updated $\tilde{\lambda}^{(j)}$, $\tilde{\Gamma}^{\sigma_j}$ and $\tilde{\Gamma}^{\sigma_{j+1}}$ using (4.54) and (4.55).

Remarks

- There are two main sources of errors, namely the Trotter error, controlled by τ (see above) and the truncation error, controlled by m (cf. remarks in Section 4.1.1). An additional error, which is arises from computer arithmetics, comes from the division by small Schmidt values in (4.54) and (4.55) (see below).

  For first order Suzuki-Trotter decomposition a value of τ of the order $\mathcal{O}(10^{-3})$ should suffice in most cases, second order Suzuki-Trotter of course behaves better and gives access to more efficient simulations.

  The matrix dimension m can either be kept constant to watch the evolution of the truncation error (4.10). However (4.10) can also be used as a threshold to dynamically adjust m, e.g. by choosing m large enough after each SVD so that the truncation error doesn't rise above a certain value. Usual threshold values range from 10^{-14} to 10^{-10}. A rise in truncation error is also always connected to a rise in bipartite entanglement entropy (4.20), both being a function of the corresponding Schmidt values $\lambda^{(\ell)}_{a_\ell}$.

Typically, time evolutions of highly excited states generate a rapid growth in entanglement entropy and thus rapid growth in m to keep the same accuracy. Of course, m only needs to be large around areas of high entanglement. However simulations quickly become either inefficient or inaccurate due to the propagation of entanglement entropy. This fact is one of the major limitations of MPS time evolution.

- The canonical representation is especially useful for TEBD time evolution, since all Schmidt decompositions and thus all 2-site wave functions of the system are accessible at all times. This also enables easy parallelization of the algorithm, by parallelizing odd and even updates separately. The feasibility of parallelization is one of the advantages of the TEBD algorithm.

- The multiplication by the inverse of the Schmidt values in (4.54) and (4.55) is numerically problematic when dividing by very small numbers. This is often the case, since Schmidt values usually decay exponentially for systems not at their critical point. One way to circumvent this problem is to exclude small singular values below a certain threshold value altogether and to set corresponding MPS matrix rows or columns to zero as well. There is however an elegant workaround to this problem proposed by Hastings, which essentially connects TEBD with the tDMRG algorithm (described in 4.2.3), avoiding the division by Schmidt values altogether [36].

4.2.3. Adaptive Time Dependent DMRG (tDMRG)

Shortly after Vidal's proposal of the TEBD algorithm in 2003, White and Feiguin proposed a modification of finite size DMRG to do time evolution, called *adaptive time dependent DMRG* or *tDMRG* [3]. Mathematically there is no difference between TEBD and tDMRG, although they use different MPS language (with tDMRG sticking to the usual mixed-canonical representation). However they both have their advantages and disadvantages from a numerical point of view.

The basic idea of tDMRG is the same as in TEBD. Again, time evolution operators, which can be Suzuki-Trotter decomposed, are addressed and time evolution is delivered by a sequential application of time evolution for even and odd bonds in small discrete time steps τ by the time evolution operator $\hat{U}(\tau)$.

The algorithm exactly follows steps (1) - (4) of finite size DMRG in Section 4.1.3, with one modification: Instead of computing block and superblock Hamiltonians to derive a new optimized superblock ground state (i.e. 2-site wave function), the existing 2-site wave function is subjected to time evolution by $u^{\sigma_j \sigma_{j+1}}_{\sigma'_j \sigma'_{j+1}}$ according to (4.52). This means that the prediction algorithm (4.38) and (4.39) to shift the 2-site wave function has now become a necessity. One time step by τ then corresponds to one full sweep through the system.

(1) Start with odd bond evolution and an initial block configuration $\bullet\bullet E$ (i.e. block S

containing 0 sites) with an initial state in mixed-canonical MPS form (3.23)

$$|\psi_0\rangle = \sum_{\{\sigma\}} \Psi^{\sigma_1\sigma_2} B^{\sigma_3} \dots B^{\sigma_L} |\sigma_1 \dots \sigma_L\rangle \tag{4.56}$$

and set $j = 1$.

(2) Apply $u^{\sigma_j\sigma_{j+1}}_{\sigma'_j\sigma'_{j+1}}$ to the 2-site wave function according to (4.52).

(3) Decompose either via SVD $\tilde{\Psi}^{\sigma_j\sigma_{j+1}} = \tilde{A}^{\sigma_j}\tilde{\lambda}^{(j)}\tilde{B}^{\sigma_{j+1}}$ or perform a reduced density matrix analysis. For right sweeping, store updated $\tilde{A}^{\sigma_j}$.[5]

(4) Shift the 2-site wave function to the right by applying (4.39), already using the updated $\tilde{A}^{\sigma_j}$.

(5) Perform another SVD of the shifted 2-site wave function $\tilde{\Psi}^{\sigma_{j+1}\sigma_{j+2}}$ to get an updated $\tilde{A}^{\sigma_{j+1}}$. Again shift to to right, using the just derived updated $\tilde{A}^{\sigma_{j+1}}$, now yielding the updated 2-site wave function $\tilde{\Psi}^{\sigma_{j+2}\sigma_{j+3}}$, shifted to the right by 2 sites in total.

(6) Perform steps (2) - (5) while $j < L - 1$, applying 2-site time evolution operators to odd bonds only. The final configuration after a full right sweep is then $S \bullet\bullet$ with E containing 0 sites, similar to above.

(7) Perform steps (2) - (5) now shifting to the left while $j > 1$, now only storing updated B-matrices. Apply 2-site time evolution operators to even bonds only.[6] The final configuration is again $\bullet\bullet E$ with all B-matrices and the 2-site wave function fully updated by one time step.

The initial state can be specified in different ways. One can also use a mixed-canonized MPS only containing A-matrices or start from the standard symmetric finite size DMRG configuration. Measurements are best taken on the fly while sweeping *back*, only using the fully updated MPS-matrices and (3.60).

Remarks

- As mentioned, tDMRG is mathematically equivalent to TEBD. Its advantage lies in the fact that it avoids the numerically problematic division by possibly small singular values. However it has the disadvantage that after each bond update one has to perform two costly SVDs in order to shift to second next bond for the next update. Notice that a preliminary SVD is necessary before every shift in tDMRG. In this manner the Canonical Representation of TEBD is clearly better. One way to combine the advantages of both methods is the mentioned modification by Hastings [36].

---

[5] Since an SVD is a costly decomposition, a density matrix analysis or even a QR decomposition (if Schmidt values are of no interest) is to be favored from a numerical point of view.

[6] If L is even, a preliminary shift to the left after completing odd bond updates is necessary to switch to even bonds. If L is odd a preliminary shift to the right once more is necessary.

- It is important that measurements are taken after MPS matrices have been fully evolved from both sides, i.e. both odd and even bond updates have been performed. If not, MPS matrices are not fully evolved yet and measured timelines will yield wrong results. It is also possible to perform a separate measurement sweep after one time step instead of measuring on the fly.

- Other than that, general remarks of TEBD (e.g. concerning Suzuki-Trotter and truncation errors) apply as well.

4.2.4. Infinite Size TEBD (iTEBD)

So far we have dealt with time evolutions for *finite* systems only. In many cases however, one is interested in (time-dependent) bulk properties of the system. On finite systems, one always faces finite size effects such as boundary effects. One approach to extract information about the thermodynamic limit in this case would be to gradually simulate systems with growing system size and then extrapolate to the thermodynamic limit. A certainly much more favorable approach would be to simulate the time evolution of an infinitely large system from the beginning.

In 2007 Vidal proposed a variation of the TEBD algorithm to simulate real and imaginary time evolution in the thermodynamic limit [37]. This algorithm turns out to be very simple and efficient due to the following assumptions:

- The Hamiltonian in the thermodynamic limit is translationally invariant

- The initial state of the infinite system is translationally invariant

- The Hamiltonian couples only nearest neighbor sites, such that the updates for even and odd bonds are parallelizable, e.g. all even and odd updates can be performed at the same time respectively.

This enables one to describe the thermodynamic limit state in terms of an iMPS using a single unit cell containing 2 sites (cf. remarks about iMPS in Section 4.1.2). In TEBD language, this means that only two individual MPS-matrices Γ^A and Γ^B and two individual sets of Schmidt values λ^A and λ^B are necessary, making the unit cell

$$\psi_{UC}^{\sigma_\ell \sigma_{\ell+1}} = \Gamma^{A,\sigma_\ell} \lambda^A \Gamma^{B,\sigma_{\ell+1}} \lambda^B \tag{4.57}$$

The full iMPS is then an infinite repetition of this unit cell (cf. (4.23) and (4.24) of Section 4.1.2).[7]

Similarly, the time evolution is described by two individual 2-site evolution operators, one for odd bonds and one for even bonds (cf. (4.48) and (4.49)).

$$\hat{U}_o(\tau) = \bigotimes_{\ell \in \mathbb{Z}} \hat{u}^A_{2\ell-1,2\ell}(\tau), \qquad \hat{U}_e(\tau) = \bigotimes_{\ell \in \mathbb{Z}} \hat{u}^B_{2\ell,2\ell+1}(\tau). \tag{4.58}$$

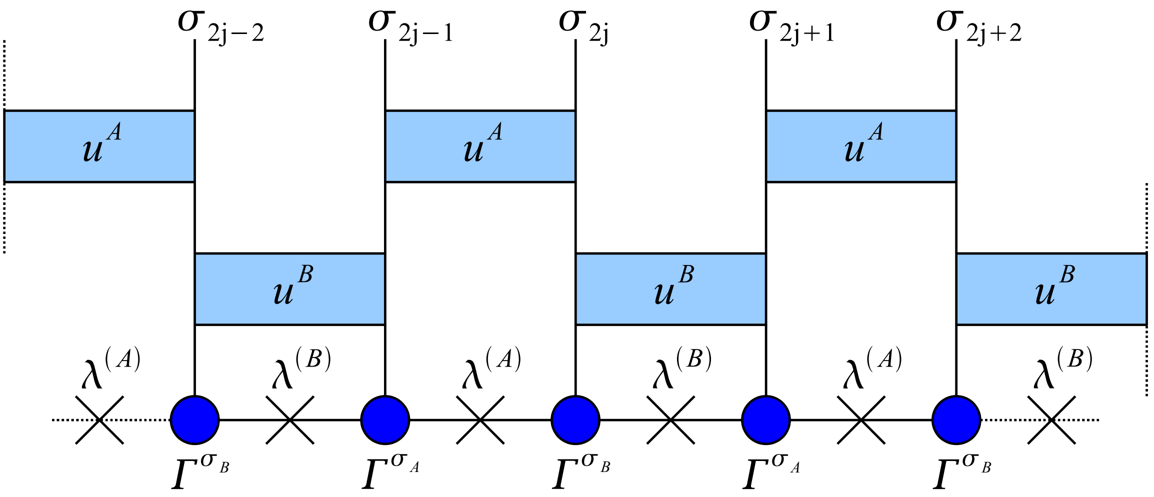

Figure 4.8.: One Suzuki-Trotter time step for an infinite size, translationally invariant MPS (iMPS). With the assumptions on page 52 it is sufficient to construct two 2-site wave functions (cf. (4.59) and (4.60)) and perform 2-site time evolution as for the TEBD algorithm (cf. also Figure 4.7) using the 2-site operators u^A and u^B for one complete time step for the infinite system.

For one time step it is necessary to perform time evolution on this unit cell only, remembering that the iMPS is an infinite repetition of this unit cell and all even, as well as all odd bond updates can be performed at the same time respectively. For simplicity we will call odd sites $\sigma_{2\ell-1} = \sigma_A$ and even sites $\sigma_{2\ell} = \sigma_B$.

(1) *odd bonds:* Construct the odd bond 2-site wave function

$$\Psi^{\sigma_A \sigma_B} = \lambda^B \Gamma^{\sigma_A} \lambda^A \Gamma^{\sigma_B} \lambda^B. \tag{4.59}$$

Apply odd bond time evolution using $\hat{u}^A$ and compute updated $\bar{\Gamma}^A$, $\bar{\Gamma}^B$ and $\tilde{\lambda}^A$ by following steps (3) - (4) from Section 4.2.2 (cf. also Figure 4.7). Notice that $\tilde{\lambda}^A$ is already fully evolved while $\bar{\Gamma}^A$, $\bar{\Gamma}^B$ still lack the update from the even bonds.

(2) *even bonds:* Using the updated matrices and Schmidt values from above, construct the even bond 2-site wave function

$$\Psi^{\sigma_B \sigma_A} = \tilde{\lambda}^A \bar{\Gamma}^{\sigma_B} \lambda^B \bar{\Gamma}^{\sigma_A} \tilde{\lambda}^A. \tag{4.60}$$

Perform even bond time evolution using $\hat{u}^B$ and again compute updated $\tilde{\Gamma}^A$, $\tilde{\Gamma}^B$ and $\tilde{\lambda}^B$ (cf. Figure 4.7). Now both MPS matrices and both sets of Schmidt values are fully evolved and one time step is completed.

---

[7] The concept is easily generalized to unit cells containing more than 2 sites by defining a corresponding number of individual MPS matrices and sets of Schmidt values. The 2-site case however is natural for 2-site time evolution operators.

Notice that this algorithm can only simulate the time evolution of an initial state under a Hamiltonian, *which are both translationally invariant over two sites*. Local disturbances break translational invariance and in order to simulate their time evolution an extension to the above procedure is needed. A possible way for simulating local signals and their time evolutions in a finite part of an infinite system is presented in Chapter 5.

5. The Comoving Window

In many applications, signal propagation in the bulk of a one-dimensional system is of interest. In order to properly simulate this scenario, one has to either use very large systems or better yet turn to infinite systems to avoid finite size effects. The standard way to simulate the behavior of local signals (e.g. spin flips or domain walls) is to introduce the signal into the center of finite system and simulate its time evolution using either TEBD (cf. 4.2.2) or tDMRG (cf. 4.2.3). However, often one needs to use a very large system in order for boundary effects not to reach the origin of the signal in the first place. Also, propagating signals will get distorted due to immediate boundary effects (e.g. Friedel oscillations) when propagating towards the boundaries and eventually get reflected at the boundaries and start interfering with themselves. The system size will thus effectively limit the accessible simulation times, during which signals can be studied undistorted by finite size effects.

In order to avoid these boundary effects one could introduce periodic boundary conditions, but then again, signals will travel around the face and start interfering with themselves after some time. Therefore a truly infinite system as background is to be favored. We have already introduced iTEBD as a method for simulating the time evolution of an infinite system in Section 4.2.4. This algorithm however requires complete translational invariance for the evolving state, as well as the underlying system Hamiltonian at all times. This fact unfortunately makes it impossible to use it to simulate the propagation of local signals.

In the following, a method is presented, which combines both the ability of finite systems to simulate local signals without boundary effects on infinite systems. It will be able to accurately simulate the time evolution of a local signal up to very high simulation times (which are *not* limited by system sizes), free from finite size effects.

We will consider systems of infinite size with nearest neighbor interactions only, initially in a translationally invariant state. We will then focus on the time evolution of signals generated by local excitations, such as one or more spin flips confined to a small area. For finite range interactions, the wave front of this type of signals can at most propagate with the system's characteristic maximum velocity, which is given by the *Lieb-Robinson bound* [38] and is essentially dependent on the interaction strengths present in the system. Therefore information and also entanglement from the signal source can only propagate within the signal's light cone. This fact is important, as the translational invariance in front of the signal front (i.e. outside the light cone) is necessary for the presented method (see below). Although correlations may reach beyond the light cone, they are exponentially suppressed there [39].

For many initial conditions (e.g. domain walls), bipartite entanglement will grow rapidly around the origin of the signal. A dramatic increase in entanglement entropy also requires an increase in matrix dimension m for MPS simulations of the same accuracy, although these parts of the system are far away from the signal front. On the other hand, entanglement entropy can only spread with the system's maximum velocity as well. Entanglement entropy around the signal front will therefore be significantly lower and vary only little over time.

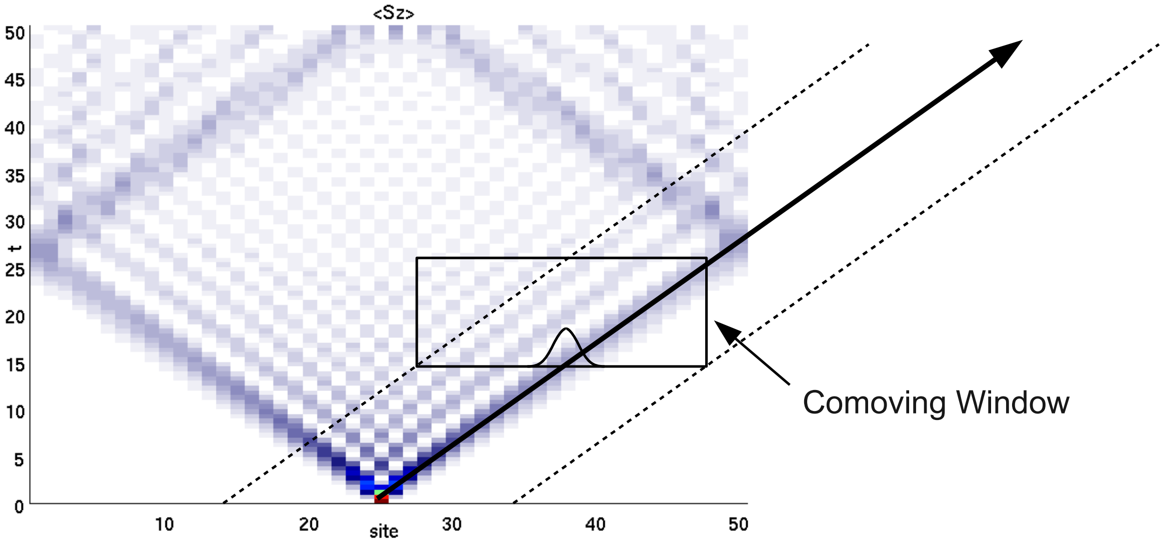

Figure 5.1.: Motivation for the Comoving Window. The time evolution of a single spin flip (magnon) excitation on a 50 site ferromagnetic XXZ chain with $J = J^z = 1$ and obc is shown. The signal hits the boundaries at $t \approx 25$, gets reflected and starts interfering with itself. The purpose of the Comoving Window is to follow the signal along its propagation path on an infinite system, removing all finite size effects.

Consider an infinite system that is initially in a translationally invariant state. The idea is to describe a part of this system by means of a finite system, which will be called the *Comoving Window (CMW)*. We will induce a local signal inside this window and simulate its propagation using time evolution methods for finite systems such as TEBD or tDMRG. The CMW is connected to the remaining parts of the infinite system on both ends. The boundaries of the window must connect smoothly to the remaining infinite system, i.e the infinite parts must be an infinite repetition of these boundaries. It is therefore crucial that the boundaries be sufficiently translationally invariant. This also means that the CMW must move along with the signal as it propagates, such that translational invariance at the boundaries is not broken by the signal itself. The time evolution of the infinite parts of the system and their influence on the CMW are simulated by a special connection update for the both ends of the CMW.

However, an immediate problem arises from the fact, that general excitations will generate signals, which travel to both sides. The CMW can only follow one branch though, with the other branch hitting the rear boundary of the CMW after some time, generating reflections and interferences there. In most cases, the signal *front* of an induced signal travels with the system's characteristic maximum velocity. Thus if one moves the CMW along with this maximum velocity, the reflections and perturbations created at the rear end can never travel far into the CMW and distort the signal of interest. In fact, as soon as this happens, one can neglect the rear infinite system altogether, treat the rear boundary of the CMW with open boundary conditions and focus on the connection at the front boundary only. In practice one can just stop performing the connection update at the rear boundary at this point.

Conversely, due to the infinite continuation at the front end, finite size effects are removed there and one can follow the signal unperturbed up to very high simulation times, which are now only limited by the truncation error or the Suzuki-Trotter error.

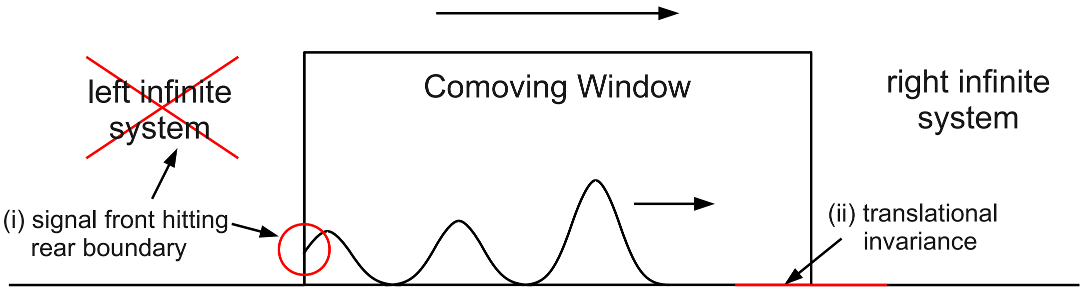

Figure 5.2.: Comoving Window moving along with a right going signal. (i) As soon as a part of the signal hits the rear boundary, the left infinite system can be disregarded. (ii) Around the front boundary a sufficiently large area of translational invariance is necessary.

5.1. Defining the Comoving Window

In this Section we will define the Comoving Window in terms of MPS language. As mentioned above, we will describe it as a finite part of the state of the infinite system. Consider a translationally invariant initial state of the infinite system in iMPS form, described by a single site unit cell $\{\hat{\Gamma}, \hat{\lambda}\}$, i.e. the iMPS consists of an infinite repetition of this unit cell.[1] For an L-site CMW we will now group together L MPS matrices and $L-1$ Schmidt values to form a set of finite size Schmidt states

$$|\Psi^{CMW}_{\alpha\beta}\rangle = \sum_{\sigma_1\ldots\sigma_L} \left(\hat{\Gamma}^{\sigma_1}\hat{\lambda}\ldots\hat{\lambda}\hat{\Gamma}^{\sigma_L}\right)_{\alpha\beta} |\sigma_1\ldots\sigma_L\rangle\,, \tag{5.1}$$

so that we can write the state of the overall system $|\Psi\rangle$ as a Schmidt decomposition on bonds $0,1$ and $L, L+1$. We rename $\hat{\lambda}$ on bond $0,1$ to $\lambda^{(l)}$ and on bond $L, L+1$ to $\lambda^{(r)}$ to get

$$|\Psi\rangle = \sum_{\alpha\beta} \lambda^{(l)}_\alpha \lambda^{(r)}_\beta \, |\Psi^{CMW}_{\alpha\beta}\rangle \left(|\Psi^l_\alpha\rangle\, |\Psi^r_\beta\rangle\right). \tag{5.2}$$

---

[1] The extension to multi-site unit cells is straight forward.

The states $|\Psi^l_\alpha\rangle$ and $|\Psi^r_\beta\rangle$ correspond to states defined on the remaining parts of the infinite system to the left and right of the CMW

$$|\Psi^l_\alpha\rangle = \sum_{\sigma_{-\infty}\cdots\sigma_0} \left(\ldots\hat{\lambda}\hat{\Gamma}^{\sigma_{-1}}\hat{\lambda}\hat{\Gamma}^{\sigma_0}\right)_\alpha |\sigma_{-\infty}\ldots\sigma_0\rangle\,, \tag{5.3}$$

$$|\Psi^r_\beta\rangle = \sum_{\sigma_{L+1}\cdots\sigma_\infty} \left(\hat{\Gamma}^{\sigma_{L+1}}\hat{\lambda}\hat{\Gamma}^{\sigma_{L+2}}\hat{\lambda}\ldots\right)_\beta |\sigma_{L+1}\ldots\sigma_\infty\rangle\,. \tag{5.4}$$

We will identify the set of Schmidt states $|\Psi^{CMW}_{\alpha\beta}\rangle$ for the L-site system together with the Schmidt values $\lambda^{(l)}$ and $\lambda^{(r)}$ on the connection bonds as the L-site CMW. The MPS matrices and Schmidt values inside the window are now generally site dependent (especially after having induced a signal inside the CMW), save around the boundaries, where we require translational invariance. The time evolution of the signal inside the window can now be simulated as for regular finite systems. Finite size effects will be removed by connecting the CMW to the infinite systems to the left (and to the right).

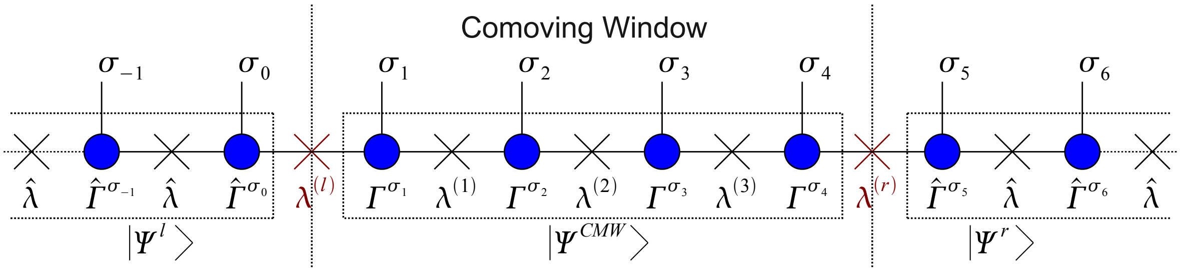

Figure 5.3.: Definition of the CMW by means of a Schmidt decomposition on two bonds.

5.2. Connection Updates

After initializing the CMW in a translationally invariant state and inducing a local signal inside, the time evolution of the CMW will be simulated by using conventional methods for finite size systems, such as TEBD or tDMRG. In finite systems, the lack of a second bond connected to the edge sites and the lack of the corresponding bond update with every time step causes boundary effects. In order to prevent this from happening for the CMW, we will need special connection updates to amend for the lacking bond update in finite size time evolution.

5.2.1. iTEBD Method (Method I)

After one TEBD time step (cf. Section 4.2.2) the boundary matrices Γ^{σ_1} and Γ^{σ_L} as well as the Schmidt values $\lambda^{(l)}$ and $\lambda^{(r)}$ on the connection bonds lack one bond update to complete the time step. As a straight forward approach, one can use separate iTEBD systems as update partners for the connections. These systems represent the infinite systems to the right and to the left of the CMW and are described by 2-site unit cells $\{\Gamma^A, \lambda^A, \Gamma^B, \lambda^B\}$, which are initially in the same translationally invariant state as the right and left boundary. Notice that for different initial states at the boundaries two separate iTEBD systems are necessary.[2]

We will investigate the case of the right boundary, the procedure for the left boundary works similarly. For one connection update, form the 2-site wave function at the connection using the iTEBD system as a partner

$$\Psi^{\sigma_L \sigma_A} = \lambda^{(L-1)} \Gamma^{\sigma_L} \lambda^{(r)} \Gamma^{\sigma_A} \lambda^A, \tag{5.5}$$

apply $\hat{u}_{L,L+1}$ to $\Psi^{\sigma_L \sigma_A}$, decompose via SVD and extract the updated $\tilde{\Gamma}^{\sigma_L}, \tilde{\lambda}^r$. Perform a separate time update for the iTEBD system (cf. Section 4.2.4), not using the updated $\tilde{\Gamma}^{\sigma_A}$ from the last step. By means of this connection update, the influence of the infinite system on the CMW has been accounted for and boundary effects are removed. For a graphical representation see Figure 5.4.

5.2.2. Copy Method (Method II)

Another interpretation of the above procedure is the following. As above, after one regular TEBD step inside the CMW the last pair $\Gamma^{\sigma_L}, \lambda^{(r)}$ is lacking the connection bond update to complete one time step. At the same time this pair has served as an update partner for the second last pair $\Gamma^{\sigma_{L-1}}, \lambda^{(L-1)}$, which in turn *has* received one complete time step update. Since translational invariance is required around the boundary, one can use the updated second last pair and copy it over the last pair, which will then again serve as an update partner for the second last pair in the next time step. In the viewpoint of the above iTEBD method, the effective boundary between CMW and the infinite system has thus shifted to the left by one bond.

This procedure also works for unit cells containing more than one site, as long as there is translational invariance in a sufficiently large area around the boundaries. In this case one would copy the pair $\Gamma^{\sigma_{L-n}}, \lambda^{\sigma(L-n)}$ over $\Gamma^{\sigma_L}, \lambda^{(r)}$, with n being the number of sites in the unit cell. However, for the sake of numerical stability, it is better to copy $2n$-tuples in stead of pairs. Overall, the use of 2-site unit cells has proved to give best results, since this unit cell size is natural to the Suzuki-Trotter decomposition.

While Method I is straight forward conceptually, Method II is numerically lighter and more efficient. There is no significant difference in results when comparing both methods, however Method II is faster. A graphical representation of this procedure is shown in Figure 5.4.

5.3. Moving the Window

In order to retain translational invariance around the front boundary, the CMW has to move along with the signal front, so that no information of the signal can disturb

---

[2] This might happen when the initial excitation is e.g. a domain wall. Both boundaries are then in a different state, but are still translationally invariant there.

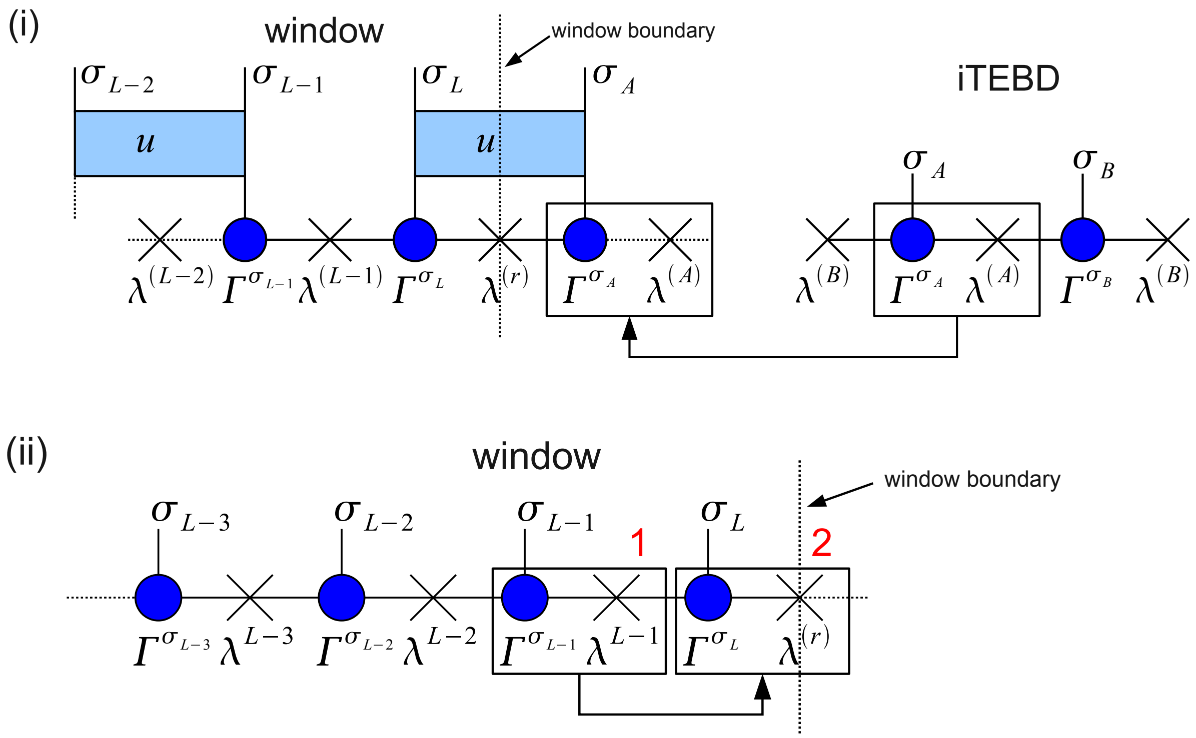

Figure 5.4.: Connection update methods. (i) Use a separate iTEBD system to form the 2-site wave function $\Psi^{\sigma_L \sigma_A}$ at the connection bond. Apply $\hat{u}_{L,L+1}$, decompose via SVD and extract updated $\tilde{\Gamma}^{\sigma_L}, \tilde{\lambda}^{(r)}$. Perform a separate time step update for the iTEBD system. (ii) After one regular TEBD step, pair 2 has served as an update partner for pair 1, which is fully evolved by one time step. Translational invariance allows for copying pair 1 over pair 2 after one time step to remove boundary effects.

the front boundary. Conceptually, window movement e.g. to the right is performed by simply redefining the finite part of the infinite system represented by the CMW. A shift by 2 sites then corresponds to redefining the CMW from containing sites $[1, \ldots, L]$ to containing sites $[3, \ldots, L+2]$.

Technically, a shift to the right by one unit cell is performed by

(1) Discarding the leftmost unit cell of the CMW,

(2) Copying all remaining MPS matrices (and Schmidt values) to the left by one unit cell,

(3) Introducing a new unit cell at the front boundary out of the infinite system. This is done by either extracting the unit cell from the iTEBD system (Method I) or reusing the former rightmost unit cell (Method II).

The window movement can be triggered with the propagation of the signal front by watching the value of a certain observable or better yet the bipartite entanglement

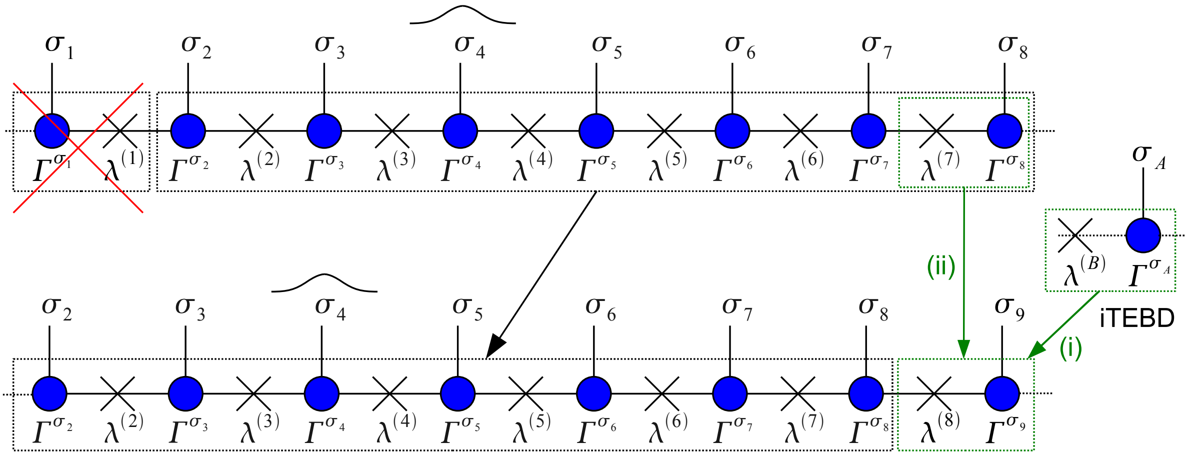

Figure 5.5.: Moving the window to the right by one site. Redefine the finite part of the infinite system described by the CMW by copying all MPS matrices (and Schmidt values) to the left by one site, discarding the leftmost unit cell. A signal around site 4 has then effectively moved to the left by one site inside the CMW. (i) When using Method I, introduce a new unit cell at the front boundary out of the iTEBD system. (ii) When using Method II, reuse the former rightmost unit cell to again be the rightmost unit cell.

entropy at a certain site (or bond) inside the CMW and moving the window, whenever the watched value changes by a significant amount.

Alternatively, if the signal front's velocity v_0 is known beforehand (the system's maximum velocity in most cases), the window can be moved along with this velocity by performing a shift every certain amount of time steps $n = \frac{\Delta t_s}{\tau}$ and $\Delta t_s = \frac{\Delta x_{UC}}{v_0}$ the time span between shifts, where Δx_{UC} the length of the unit cell.

Depending on the correlation lengths present in the system one has to carefully adjust the margin between the signal front and the front boundary of the CMW. This effectively governs the choice of the site (or bond) for the quantity to watch when triggering the window shift. For systems, which show phase transitions, correlation lengths increase drastically close to their critical point. Therefore the margin between signal front and front boundary of the CMW has to be adequately large. This fact actually limits the effectiveness of the CMW method, as the necessary size of the CMW increases dramatically when getting close to the critical point.

5.4. Gauge Freedom and Phase Convention

The definition of the CMW in Section 5.1, together with the Connection Updates from Section 5.2 and the Window Movement from Section 5.3 describe the basic framework of the CMW method. Before implementing and testing there is however an essential technical detail one has to take care of.

Ground state search methods (DMRG), as well as time evolution methods (TEBD, tDMRG) make extensive use of SVD. Whenever one performs such a decomposition, there is the freedom of phase for every pair of left and right singular vector. Let us consider the case of an SVD of a general matrix

$$M_{\alpha\beta} = \sum_\gamma U_{\alpha\gamma} D_\gamma {V_{\gamma\alpha}}^\dagger, \tag{5.6}$$

with U and V again unitaries, where the columns of U are the left singular vectors of M and the columns of V are the right singular vectors of M. D is a diagonal matrix containing the singular values of M as its diagonal elements. When choosing another gauge, one can multiply each singular value D_γ with unity, expanded as $1 = e^{i\varphi_\gamma} e^{-i\varphi_\gamma}$, giving

$$D_\gamma = e^{i\varphi_\gamma} D_\gamma e^{-i\varphi_\gamma}. \tag{5.7}$$

For every singular value one can choose an individual phase φ_γ. Inserting (5.7) into (5.6) then defines new unitary matrices, containing left and right singular vectors, now in a different gauge

$$M_{\alpha\beta} = \sum_\gamma \underbrace{U_{\alpha\gamma} e^{i\varphi_\gamma}}_{:=\tilde{U}_{\alpha\gamma}} D_\gamma \underbrace{e^{-i\varphi_\gamma} {V_{\gamma\alpha}}^\dagger}_{:=\tilde{V}^\dagger_{\gamma\beta}} = \tilde{U}_{\alpha\gamma} D_\gamma \tilde{V}^\dagger_{\gamma\beta}, \tag{5.8}$$

which is of course also a valid SVD of M. The key point is that, even though one is free to choose an individual phase for all pairs of left and right singular vectors, they are always connected by this phase. Thus only changing gauge for one kind of singular vectors (left or right) gives a wrong decomposition as the different phase factors don't cancel out

$$\left(U_{\alpha\gamma} e^{i\tilde{\varphi}_\gamma}\right) D_\gamma \left(e^{-i\varphi_\gamma} {V_{\gamma\alpha}}^\dagger\right) = U_{\alpha\gamma} \underbrace{e^{i\tilde{\varphi}_\gamma} e^{-i\varphi_\gamma}}_{\neq 1} {V_{\gamma\alpha}}^\dagger D_\gamma \neq M_{\alpha\beta}. \tag{5.9}$$

This fact is of importance when considering the numerical realization of the Connection Update Methods introduced in Section 5.2, since both methods rely on joining matrices, originally defined in different auxiliary spaces, together to form a 2-site wave function.

In the case of Method I, time evolution for the CMW and the iTEBD system is done separately. When performing the actual connection update, two MPS matrices stemming from independent numerical SVDs are put together to form (5.5). In the case of Method II, (at least) one matrix from a different site and thus also stemming from a different numerical SVD is copied and again joined to form a 2-site wave function. A possible difference in phase conventions can then yield a wrong result for the formed 2-site wave function resulting in perturbations traveling into the window as artificial signals.

In practice, when applying SVDs numerically by means of a software package, the corresponding routine necessarily has a certain phase convention mechanism implemented.

Consider a CMW initially in a completely translationally invariant state, i.e. before a signal has been induced. When doing time evolution without a signal, translational invariance is preserved, thus the same phase convention will be chosen by the software package everywhere. If one now introduces a local signal somewhere, the phase convention mechanism of the package might then switch to a different phase convention around the signal at some point. Due to the nature of the Suzuki-Trotter expansion this new phase convention will then spread with an unphysical velocity of 2 sites per time step τ. As it is a numerical effect and has no physical meaning, this fact does not conflict with the Lieb-Robinson bound and the existence of a maximum velocity (cf. beginning of Section 5). As soon as this new phase convention reaches the front boundary, where matrices stemming from different SVD are put together, it will happen, that a matrix coming from an SVD already using the new phase convention will be joined with a matrix still using the old phase convention. At this point, artificial signals will be generated, which travel into the window, distorting the signal front of interest.

To circumvent this problem one can manually fix the phase convention for all SVDs by e.g. requesting that for every left singular vector the component with largest absolute value be real and positive. This effectively protects the area around the front boundary from any new phase conventions coming from inside the CMW. This procedure has shown to fix the above issue, whereas the generation of perturbations has been observed when no phase convention was implemented. These perturbations are strong enough to distort the signal front of interest considerably, thus causing the break down of the method. The implementation of a phase convention is therefore necessary for the CMW method to work properly.

6. Results

The CMW method has been tested for several signal types on infinite one-dimensional spin chain models as introduced in Section 2. The general procedure is to initialize the system in one of its eigenstates (not necessarily the ground state), induce a local signal inside the CMW and follow its fastest right going branch. While following the signal front, various observables are measured and various properties are investigated.

For the time evolution of all signals, the CMW method with second order Suzuki-Trotter decomposition (cf. Section 4.2.1) and connection update method II (copying, cf. Section 5.2) has been used. Since all initial states are translationally invariant at both boundaries, copying has also been performed at the rear boundary up to the impact of the left going branch. From this moment on obc were imposed there.

Window movement has been triggered with the relative growth of bipartite entanglement entropy (3.40) above a small threshold $\epsilon_S = 0.5\%$ at a certain specified bond inside the CMW, unless stated otherwise. The CMW hence moves along with the propagation front of signal information, which is generally the system's maximum velocity.

6.1. XX Model

For an initial test of the CMW, the following very simple scenario has been chosen. The infinite XX spin chain with $J > 0$ has been initialized in the magnon vacuum state $|0\rangle$ (2.18), i.e. in the all spin down state. As a signal, a single spin in the center of the CMW has been flipped to spin up, i.e. a 1-magnon state

$$|\psi\rangle_j = c_j^\dagger |0\rangle \tag{6.1}$$

with $j = \frac{L}{2}$ has been induced. This excitation decays into 2 signal branches going left and right. Subsequently, the right going branch of the signal has been followed with the CMW, where window movement has been triggered with the growth in bipartite entanglement entropy (3.40) around the signal front. The signal has been followed up to very large times to compare the measured magnetization $\langle \hat{S}_j^z(t) \rangle$ with the analytic result (2.25) to give a first estimate of the performance of the CMW method. Additionally, the dependence of the signal propagation velocity on the interaction parameter J has been studied.

It can be shown that for product states the expectation values of hermitian operators are the same under time evolutions of $\hat{H}_{XX}(J)$ and $\hat{H}_{XX}(-J)$ (cf. Section 2.2 and [40]), therefore the sign of parameter J is of no importance. This is exactly the case for the investigated spin flip initial state. Therefore only the case $J > 0$ has been considered.

6.1.1. Initial State

The all spin down state is in fact very simple to encode as an iMPS, since the state is one of the local spin basis product states and in theory an MPS dimension of $m = 1$ would suffice. However, the vacuum state iMPS wa¡s initialized directly with the MPS dimension m used throughout the rest of the simulation. One way to encode the all spin down state this way is to use a 1-site unit cell with

$$\Gamma^{\uparrow}_{kl} = 0, \qquad \Gamma^{\downarrow}_{kl} = \delta_{1k}\delta_{1l}, \qquad \lambda_k = \delta_{1k}. \tag{6.2}$$

An L-site CMW was then filled with this unit cell and a single spin in the center at site j was flipped according to (A.17), giving

$$\Gamma^{(j),\uparrow}_{kl} = \delta_{1k}\delta_{1l}, \qquad \Gamma^{(j),\downarrow}_{kl} = 0, \tag{6.3}$$

i.e. $\Gamma^{(j),\uparrow}$ and $\Gamma^{(j),\downarrow}$ switched places on site j.

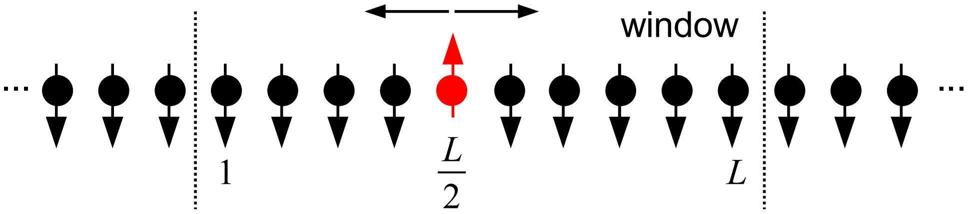

Figure 6.1.: Initial state with a 1-magnon excitation out of the all spin down vacuum state. The single flipped spin induces a signal splitting into a left and a right going branch.

Notice that because the initial state with one flipped spin is again a local spin basis product state, entanglement entropy is zero everywhere in the system. During time evolution, the decaying excitation in the center will cause a rise in bipartite entanglement inside the signal's light cone. Sufficiently outside the light cone, entanglement entropy will remain zero at all times.

6.1.2. Propagation Velocity of Spin Flip Signals

The group velocity for wave packets of free fermions can easily be derived from the dispersion relation $\varepsilon_k = -J\cos(k)$

$$v(k) = \frac{d\varepsilon_k}{dk} = J\sin(k). \tag{6.4}$$

When generating a general wave packet of free fermions centered around a certain momentum k, it will stay the most stable around momentum regimes, where the dispersion relation is close to linear, i.e. around $k = \pm\frac{\pi}{2}$ and all momenta in this regime move roughly with the same velocity $v\left(\pm\frac{\pi}{2}\right) = \pm J$, which is then also the system's maximum velocity from this viewpoint (cf. Figure 6.2 and also [40]). From this considerations one can expect that a general signal's propagation front will always be the most prominent part of the signal, moving with $v_0 = \pm J$, even though the signal is not of wave packet character. Indeed this is also the case for the investigated single spin flip magnon excitation. This can also be seen in the shape of the signal in Figure 6.4.

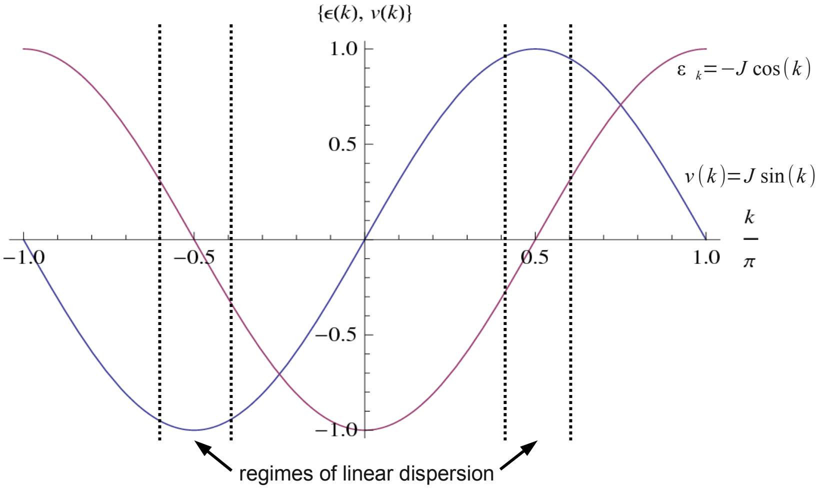

Figure 6.2.: Dispersion relation and group velocity for free fermions. Around $k = \pm\frac{\pi}{2}$ the dispersion relation is closest to linear. On the other hand the group velocity has its maximum/minimum $v_0 = \pm J$ there, resulting in a high density of states with that velocity.

For the case of the XX model, the linear dependence $v_0 \propto J$ can be understood very easily, as J is the only experimental parameter and a multiplicative factor for the entire Hamiltonian. A change in J corresponds to a rescaling of the energy levels and thus of the time scale as well. A system evolved to time t with a parameter J will look like a system with J twice as large at half the time.

6.1.3. Time Evolution of Single Spin Flips

Notice that the nature of the initial state is such, that there would be no finite size boundary effects in a finite system either, i.e. the all spin down state is also an eigenstate of the finite system with obc. Therefore a connecting infinite system to the right and to the left are actually not necessary.

However, as a first test for the connection updates, simulations have been done both with and without connection updates for $J = 1$ with $\tau = 0.01$ and $m = 8$ up until $t = 200$.[1] Time evolutions of the magnetization and the bipartite entanglement entropy

---

[1] Due to the very simple structure of this signal an MPS dimension as low as $m = 8$ already gives a truncation error $\epsilon < 10^{-14}$

(3.40) for both cases up to $t = 100$ can be seen in Figure 6.3. Magnetization has been measured on each site j according to (3.60) and bipartite entanglement entropy has been measured on each bond $j, j+1$ according to (3.40). The latter quantity describes the bipartite entanglement between the left and right part of the system, which has been cut at bond $j, j+1$. As can be seen, the CMW follows the right going signal front perfectly in both cases and no boundary effects are introduced at the front boundary. The signal and its evolution during propagation can therefore be studied unhindered up to very large times, which are now only limited by truncation errors or Trotter-Suzuki errors. The simulated CMW results will be compared to the exact solution (2.25) below.

There are also no significant differences between the timelines of the observables magnetization $\langle \hat{S}^z_j(t) \rangle$ and the bipartite entanglement entropy $S_{ent}(t)$ (cf. (3.40)) for both simulations. Largest deviations arise at the point where the left going signal branch hits the rear boundaries and the simulation using connection updates switches to obc. There, relative deviations are of the order $\mathcal{O}(10^{-5})$, everywhere else relative deviations are at most of the order $\mathcal{O}(10^{-10})$.

As a next test, the magnetization $\langle \hat{S}^z_j(t) \rangle$ has been compared to the exact result (2.25) at times $t = 100, 150, 200$. The simulated data is in very good agreement with the exact solutions, even at large times. Largest relative deviations again occur at the rear boundary after the impact of the left going signal branch and are of the order $\mathcal{O}(10^{-3})$. From this moment on, reflections from the rear boundary are constantly sent into the CMW, but since they propagate with the same velocity as the signal front and hence the CMW itself, they can never travel far into the window. In fact, perturbations from the rear boundary are restricted to the first few sites into the window at all times, as can be seen in Figure 6.4. Inside the window, relative deviations are of the order $\mathcal{O}(10^{-6})$.

6.2. XXZ Model

The CMW method has also been tested for the XXZ chain (cf. Section 2.4). Two kinds of signal types have been investigated: (1) Single and double spin flips to the all spin down state with no magnetic field as for the XX chain and (2) the evolution of the ground state of the antiferromagnet (AFM) under a time dependent Hamiltonian, where a local magnetic field has been turned on at $t = 0$. Whereas case (1) yields results very similar to those of the XX chain, case (2) caused serious problems, which were as of now not possible to be overcome.

Again, magnetization timelines $\langle \hat{S}^z_j(t) \rangle$ and bipartite entanglement entropy timelines $S_{ent}(t)$ (cf. (3.40)) have been simulated for several values of J^z up to very large times, where $J = 1$ at all times.[2] The evolution of the shape of the resulting signal front has been investigated.

---

[2] A change in J would again correspond only to a rescaling of the energy with a rescaled parameter J^z in turn. It is therefore sufficient to investigate only variations in J^z.

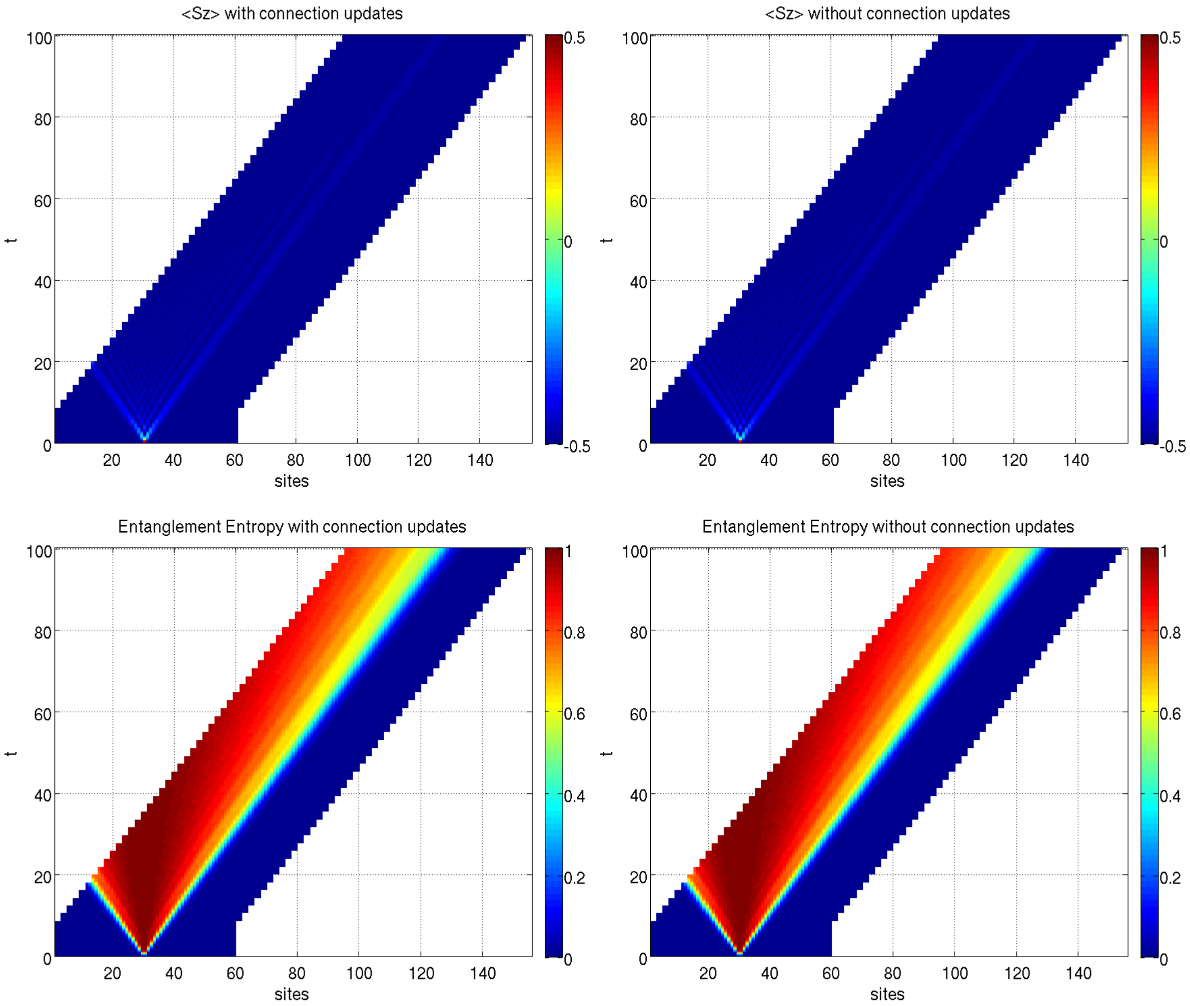

Figure 6.3.: Single magnon excitation of the XX chain for $J = 1$ with $\tau = 0.01$ and $m = 8$. The timelines for the magnetization $\langle \hat{S}^z_j(t) \rangle$ and bipartite entanglement entropy $S_{ent}(t)$ (cf. (3.40)) for the simulations with (on the left) and without connection updates (on the right) show no significant difference. Largest deviations are of the order $\mathcal{O}(10^{-5})$ at the point, where the left signal branch hits the rear boundary. This is due to the switch to obc for the simulation using connection updates.

6.2.1. Time Evolution of Single Spin Flips for the FM

For the investigation of signal front shapes of spin flip signals, the initial state has again been encoded into an MPS according to (6.2) and (6.3). For the ferromagnetic (FM) case $J^z > 0$ and $\Delta > 1$ in the thermodynamic limit, the all spin down state is one of the degenerate ground states, however for the antiferromagnetic (AFM) case $J^z < 0$ and $\Delta < 1$ it is in fact a high energy eigenstate. For further details on ground states for other values of J and Δ see e.g. [19].

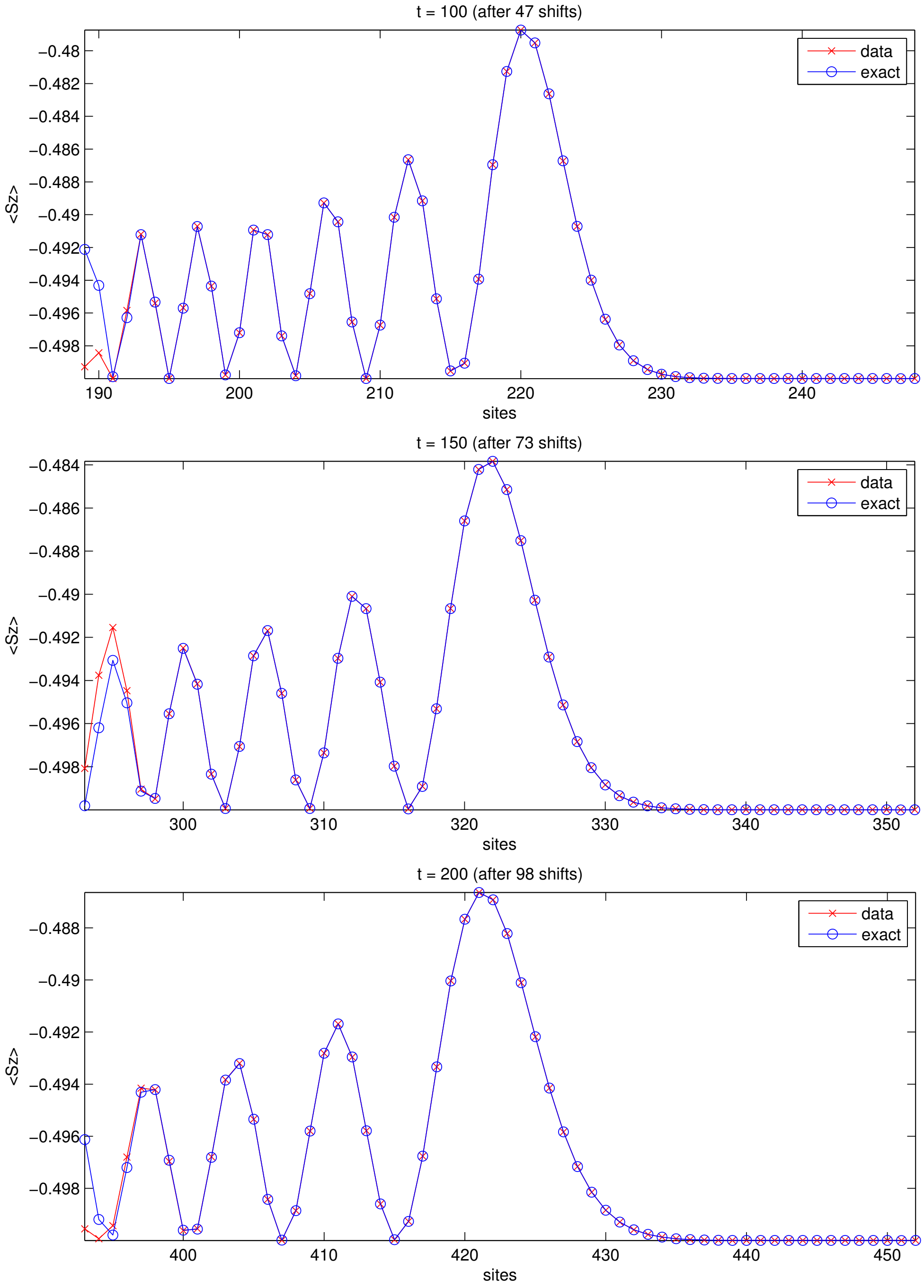

Figure 6.4.: Comparison of the magnetization $\langle \hat{S}_j^z(t) \rangle$ of a single magnon excitation with the exact result (2.25) for $J = 1$. Comparisons have been made at times $t = 100, 150, 200$ and show very good agreement. Largest relative deviations arise at the rear boundary and are of the order $\mathcal{O}(10^{-3})$. Everywhere else relative deviations are of the order $\mathcal{O}(10^{-6})$.

Again, the expectation values of hermitian operators (such as magnetizations) for time evolution of product states under $\hat{H}_{XXZ}(J, \Delta)$, $\hat{H}_{XXZ}(-J, \Delta)$ and $\hat{H}_{XXZ}(J, -\Delta)$ are the same [40]. For $J = 1$ only the magnitude of Δ is thus of importance. Simulations have therefore been performed for $J^z > 0$.

As a matter of fact, the simulations for single spin flips yield the *exact* same results in terms of magnetization and bipartite entanglement entropy as single spin flips to the XX chain up to order $\mathcal{O}(10^{-14})$. This can be understood in the particle picture, as the Ising interaction controlled by J^z is a particle-particle interaction. With no other particle in the system, there is no interaction, but only a constant energy shift, which makes the XXZ Hamiltonian equivalent to the XX Hamiltonian for a single particle. The time evolution of single spin flips in the XXZ chain is therefore independent of the value of J^z.

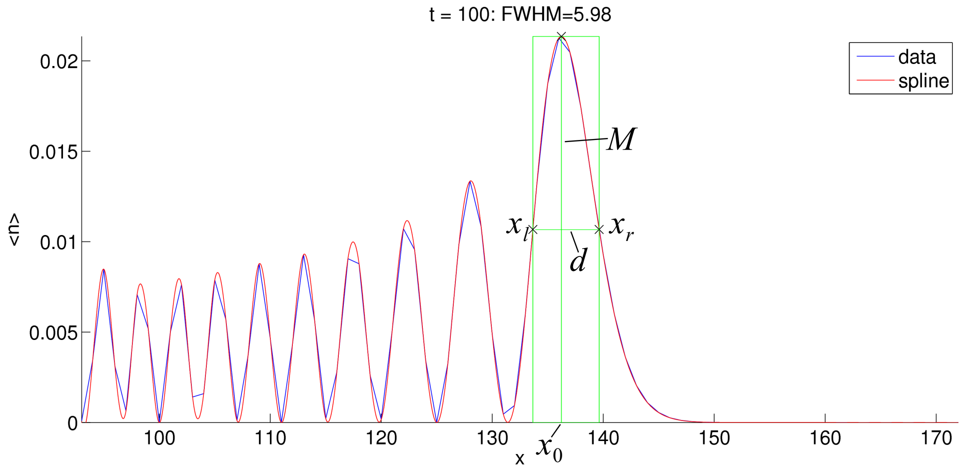

Figure 6.5.: Determination of position, width and magnitude of the signal front for a single magnon signal front on the XXZ chain at $J^z = 1$. The particle density $\langle n_j \rangle = \langle \hat{S}^z_j \rangle + \frac{1}{2}$ is shown. The width of the signal is taken as the full width at half maximum $d(t) = x_r(t) - x_l(t)$. The magnitude $M(t)$ of the signal is taken as the maximum of the spline interpolation within the signal front. Its position is used as the position $x_0(t)$ of the signal front. One can see that the splines work best around $x_l(t)$ and $x_r(t)$.

As a first characterization, the shape of the signal front of a single spin flip has been investigated. The position $x_0(t)$ as well as the magnitude $M(t) = \langle n(x_0(t), t) \rangle$ of the maximum of the signal front, where $n_j = \hat{S}^z_j + \frac{1}{2}$ is the particle density, have been determined. To get the width of the front, the full width at half maximum (FWHM) has been calculated by determining the points $x_l(t)$ and $x_r(t)$ left and right of the maximum, where the particle density has dropped to one half of the maximum of the signal front. The FWHM is then $d(t) = x_r(t) - x_l(t)$. To determine all of these points accurately, cubic splines have been used to interpolate between data points. An example is given in Figure 6.5.

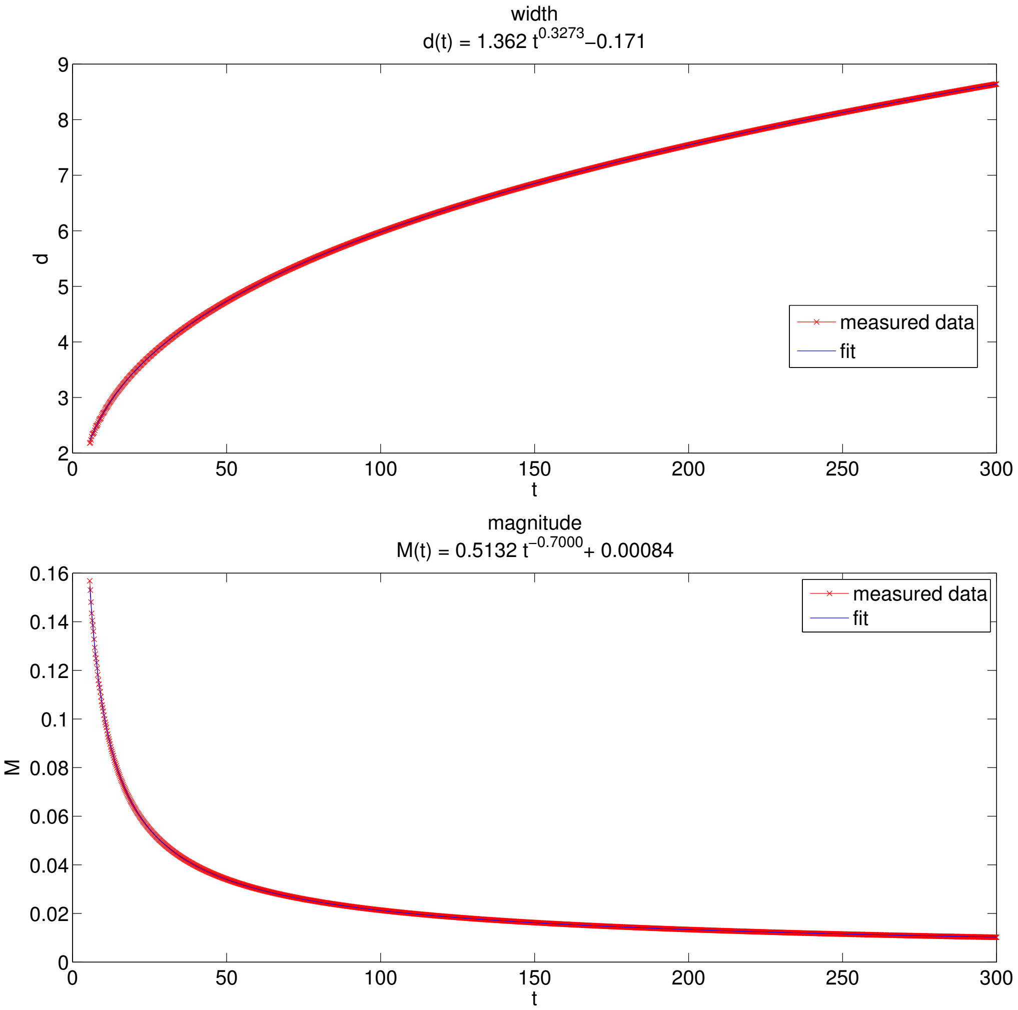

Figure 6.6.: Signal width and height of a single magnon signal front on the XXZ chain with $J^z = 1$ up to $t = 300$. It is evident that the width $d(t)$ does not increase linearly with time, nor does it seem to converge to a constant value $d(t_\infty)$. A power law fit for the model $y(t) = at^\alpha + c$ yields an exponent α which is clearly within $0 < \alpha < 1$, showing that the width diverges for very large times. The relative width with respect to the propagated distance (which is proportional to t) however converges, since $\alpha < 1$. The magnitude of the signal decreases rapidly over time and seems to also follow a power law. A fit of the same model yields a negative exponent $\alpha < 0$ and thus a constant value of $M(t_\infty) = c \approx 0$.

The evolution of the signal shape has been determined for a single spin flip up to $t = 300$. The FWHM has been found to increase with a power α as $d(t) \propto t^{\alpha}$ with $0 < \alpha < 1$, i.e. the width increases root-like with time and does not converge to a constant value. This can be seen in Figure 6.6. Since $\alpha < 1$, the relative width compared to the propagated distance (which is proportional to t) goes to 0 for $t \to \infty$. This means that for very large times all characteristic points move with the same velocity (see below).

Since the signal itself propagates with a constant velocity $v = J = 1$, the power law behavior of $d(t)$ leads to the conjecture, that some of the characteristic points $x_l(t)$, $x_r(t)$ and $x_0(t)$ must propagate non linearly to produce the power law behavior of $d(t)$, i.e. their propagation velocities will vary over time. In order to investigate this, the individual time dependent velocities $v_l(t)$, $v_r(t)$ and $v_0(t)$ have been estimated via simple numerical differentiation

$$v_j(t_i) = \frac{x_j(t_i) - x_j(t_{i-1})}{t_i - t_{i-1}}. \tag{6.5}$$

The estimated velocities have then been compared to the constant velocity $v = 1$. It can be seen that the closer the point to the front boundary of the light cone, the smaller the deviation of its velocity from $v = 1$. Indeed $v_r(t)$ has converged to $v = 1$ better than $v_l(t)$ by about one order of magnitude at $t = 300$. Due to the fact, that the spline interpolations work best around the steep parts of the signal front, but strongly depend on the actual position and values of the measured magnetizations around the maximum, the interpolated position of the maximum of the front shows some oscillatory behavior, which is a relic from the interpolation. The estimated velocity $v_0(t)$ therefore also shows strong oscillatory behavior and is plotted separately. The time evolution of the velocities can be seen in Figure 6.7.

The magnitude of the signal front seems to also follow a power law in time with a negative exponent, leading to the conjecture that it converges to a constant value. A power law fit $M(t) = at^{-\alpha} + c$ yields a constant value of $M(t_{\infty}) = c = (84 \pm 3) \cdot 10^{-5} \approx 0$ for $t \to \infty$. The timeline of the signal magnitude of the front is shown in Figure 6.6.

Since a single spin flip signal on the XXZ chain is equivalent to a single spin flip signal on the XX chain these results can also be deduced from the exact solution (2.25). This is however not the case for signals with more than one particle, e.g. double spin flips.

6.2.2. Time Evolution of Double Spin Flips for the FM

In the next step, spin flips of two adjacent sites in the center of the CMW have been (as depicted in Figure 6.8) have been investigated. Following the same reasoning as in 6.2.1, only the case $J^z > 0$ has been considered. These 2-particle excitations decay into a signal front moving at the system's maximum velocity v_0 (independent of J^z) and a bound state with a velocity $v_b < v_0$ dependent on J^z [40, 21, 19]. These bound states as a special class of eigenstates of the XXZ Hamiltonian can be investigated by means

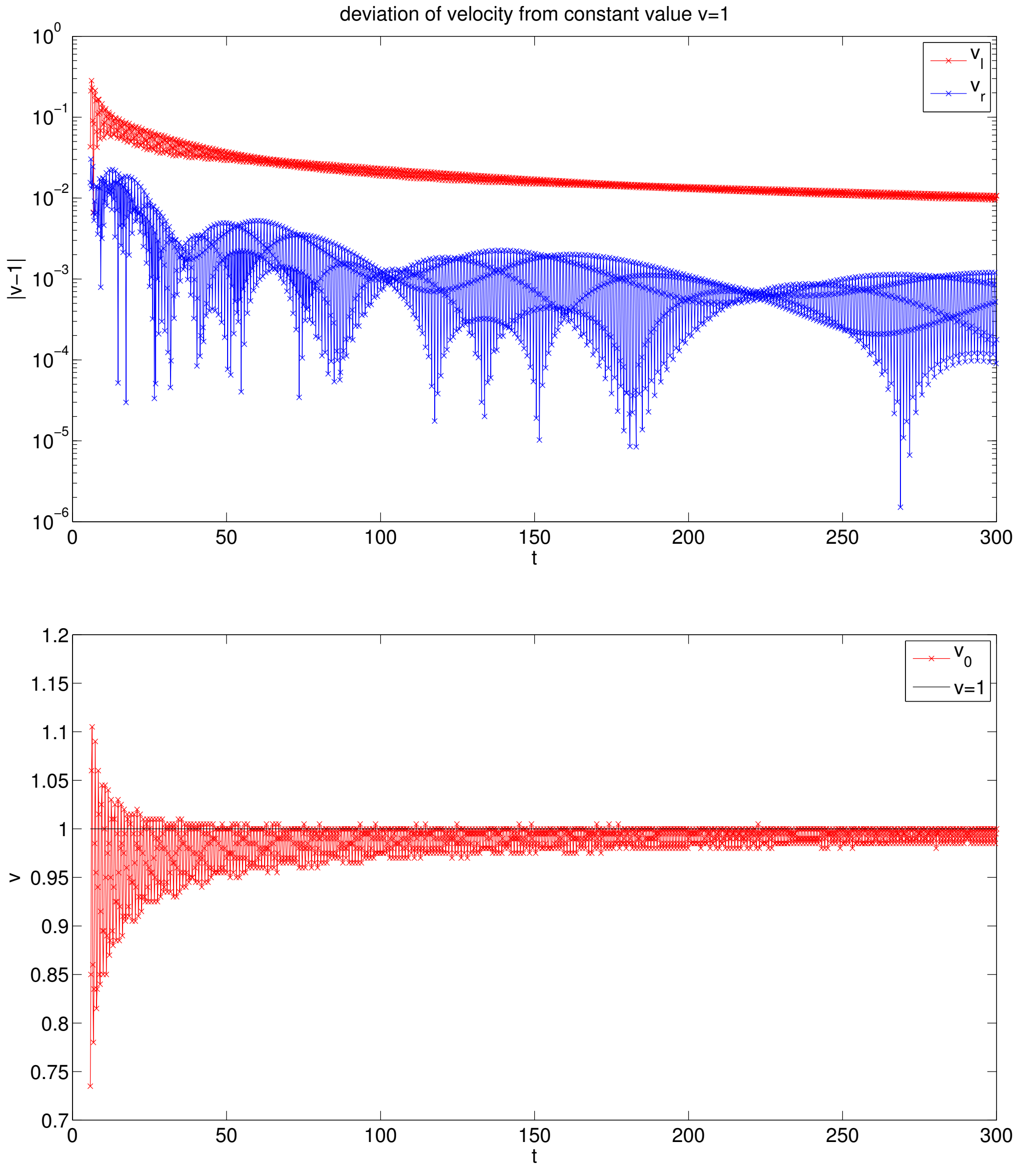

Figure 6.7.: Deviations of the individual velocities of the 3 characteristic points of the signal front from the constant value $v = 1$. The deviation from the constant value gets smaller the closet the point to the frontmost part of the signal front. The velocity $v_r(t)$ has converged to $v = 1$ better by one order of magnitude as $v_l(t)$ at $t = 300$, which can be seen in the top panel. The position of the maximum of the front shows strong oscillation, which is a relic of the spline interpolation. It is thus plotted separately in the bottom panel. Notice that the small oscillations in $v_l(t)$ and $v_r(t)$ are amplified by the logarithmic plot.

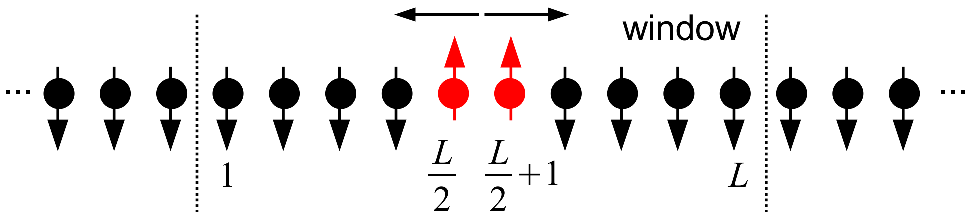

Figure 6.8.: Initial state with a 2-magnon excitation out of the all spin down vacuum state. The two flipped spins induce a signal splitting into a left and a right going branch.

of the Bethe ansatz. They follow a dispersion relation

$$\varepsilon_k = J\left(\Delta - \frac{1}{2\Delta} - \frac{1}{2\Delta}\cos(k)\right). \tag{6.6}$$

The group velocity is then

$$v_g = \frac{d\varepsilon_k}{k} = \frac{J}{2\Delta}\sin(k) = \frac{J^2}{2J^z}\sin(k). \tag{6.7}$$

By the same reasoning as in Section 6.1, the most prominent part of this signal type will travel with momenta $k = \pm\frac{\pi}{2}$ and the maximum velocity $v_b = \frac{J}{2\Delta}$, which now depends on both parameters J and J^z. For a fixed value of $J = 1$, the velocity is inversely proportional to the particle-particle interaction parameter J^z via $v_b = \frac{1}{2J^z}$. According to the Bethe ansatz, solutions only exist for $\cos(k) < 2\Delta^2 - 1$. However the dispersion is only linear around $k = \pm\frac{\pi}{2}$, i.e. the states around these momenta are required to form stable signals, which do not decay. This requires $\cos(k) > 0$ and the formation of bound states will only be observed as local magnetization signals if $2\Delta^2 - 1 > 0$ or $\Delta > \frac{1}{\sqrt{2}}$. These signals then have a maximum velocity at $\Delta = \frac{1}{\sqrt{2}}$ of $v_b = \frac{J}{\sqrt{2}}$, which is $\approx 70\%$ of the system's maximum velocity $v_0 = J$ [41, 40, 19]. Timelines for bipartite entanglement entropy $S_{ent}(t)$ (3.40) and magnetization $\langle \hat{S}^z_j(t)\rangle$ for different values of J^z with $J = 1$ up to $t = 100$ can be seen in Figure 6.9.

It has been further investigated, if the formation and propagation of this bound states affects the signal shape and evolution of the front. The same analysis for width and magnitude of the signal front as for single spin flips in Section 6.2.1 has been performed for several values of J^z. The timelines for width and magnitude of the signal fronts for 7 values of J^z from $J^z = 0.1$ to $J^z = 1.9$ can be seen in Figure 6.10. It is clearly evident that the bound states influence the evolution of the signal front, which moves with the system's maximum velocity $v_0 = 1$ always. While the bound states do not influence the width much, they considerably affect the magnitude of the signal front, also at large times. This corresponds to an increasing magnitude in the bound state propagation branch (cf. Figure 6.9). Because the total magnetization S^z (i.e. the total particle number N) is conserved, this necessarily leads to a reduction of intensity in the single particle branch.

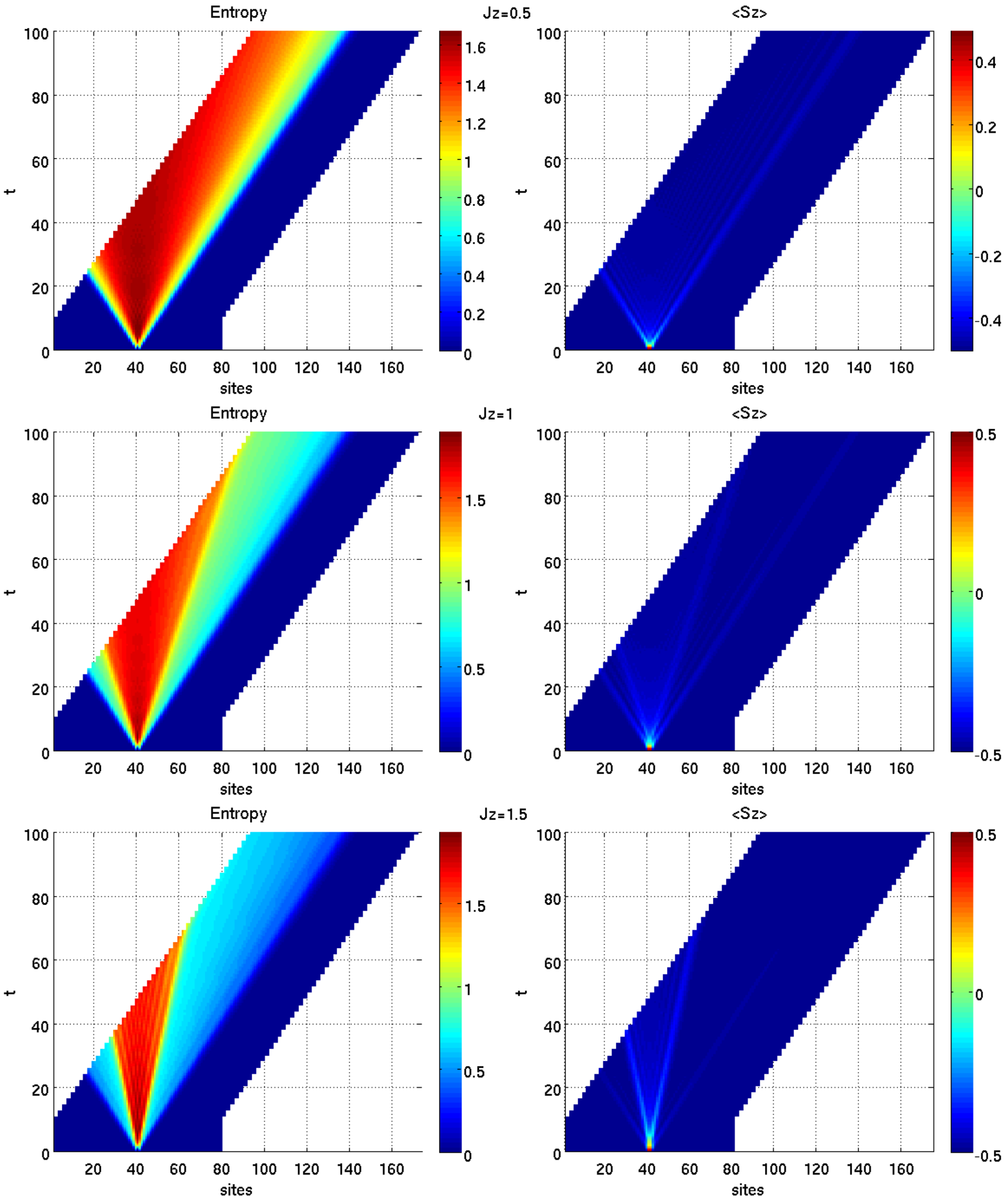

Figure 6.9.: Timelines for bipartite entanglement entropy $S_{ent}(t)$ (cf. (3.40)) and magnetization $\langle \hat{S}^z_j(t) \rangle$ of a double spin flip on the XXZ for $J^z = 0.5, 1, 1.5$. The emergence of bound states with velocity $v_b = \frac{1}{2J^z}$ is evident only for $J^z > \frac{1}{\sqrt{2}}$.

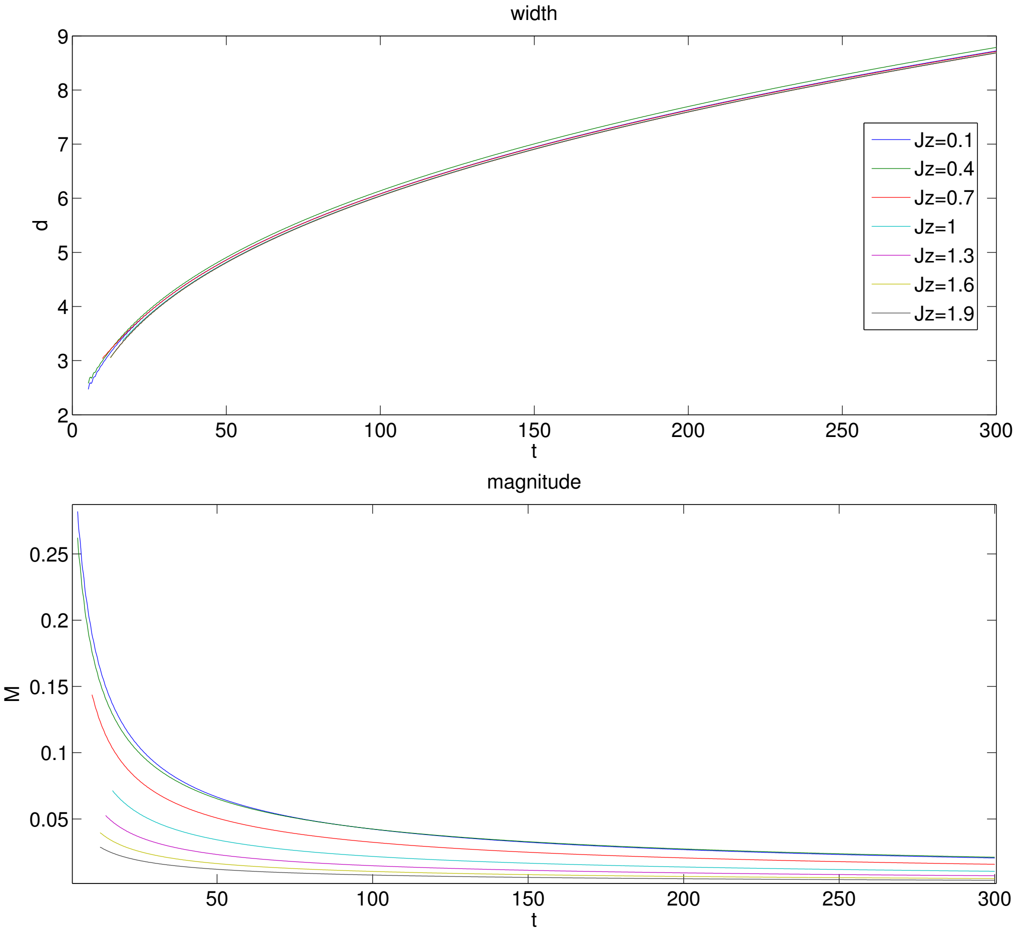

Figure 6.10.: Width and magnitude of the signal front of a double spin excitation on the XXZ chain for 7 values of J^z from $J^z = 0.1$ to $J^z = 1.9$.

To get a better comparison, width and magnitude for many values of J^z from $J^z = 0$ to $J^z = 2.5$ at time $t = 300$ have been plotted against the J^z, which is shown in Figure 6.11. $J^z = 0$ corresponds to the limit of the XX chain, the 2 flipped spins therefore propagate as 2 non interacting 1-magnon signals. With increasing value of J^z it is evident that the bound states cause an increase in both width and magnitude of the signal front at large times, with both maxima at $J^z \approx 0.3$. Both width and maximum then decrease for $J^z > 0.3$ with the width reaching a minimum at $J^z \approx 1.4$, whereas the magnitude decreases monotonically with J^z (at least up to $J^z = 2.5$). The magnitude also has its inflection point near $J^z = \frac{1}{\sqrt{2}}$, where bound states start to emerge as stable signals for $J = 1$. For values of $J^z < \frac{1}{\sqrt{2}}$ the magnetization corresponding to the bound state is delocalized inside the light cone, where the maximum coherence with the signal front apparently occurs around $J^z \approx 0.3$.

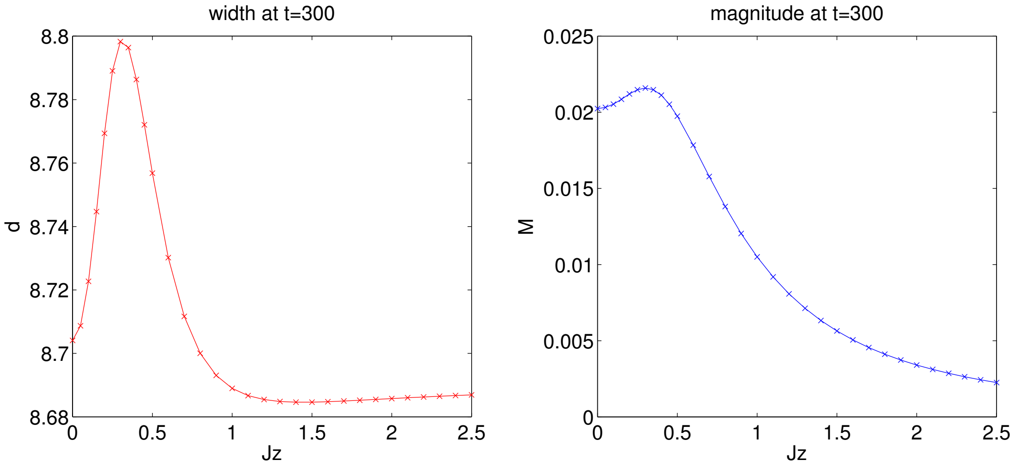

Figure 6.11.: Width and magnitude of the signal front of a double spin flip in the XXZ chain at $t = 300$ versus J^z from $J^z = 0$ (limit of XX chain) to $J^z = 2.5$. Both width and magnitude have a maximum at $J^z \approx 0.3$. Width and magnitude then decrease with the width taking a minimum at $J^z \approx 1.4$, whereas the magnitude continues to decrease monotonically. The magnitude also has its inflection point close to $J^z = \frac{1}{\sqrt{2}}$, where bound states start to emerge as stable signals.

6.2.3. Time Evolution of the AFM Ground State under a Time Dependent Hamiltonian

Simulations have also been attempted for the ground state of the AFM as an initial state, with $J = 1$ and $J^z < 0$. However this state is much more complex than the ground state of the FM (cf. Section 2.4) and cannot be encoded in MPS form in a straightforward way. It has therefore been computed using iDMRG (cf. Section 4.1.1) with a proper convergence criterion (4.34) (cf. Section 4.1.2). The derived ground state however shows a 2-site translational invariance, with both sets of Schmidt values showing degeneracy, thus yielding a 2-site unit cell for the iMPS representation. An example for Schmidt values is given in Table 6.1. AFM ground states have been calculated for $J = 1$ and several values of $J^z < -1$ without magnetic field. Due to the complex structure of the AFM ground state, a very high number of kept states m is required. A canonization of the derived 2-site unit cell according to Section A.1 has been performed.

After filling a CMW of even amount of sites with the derived and canonized 2-site iMPS, the investigation of local signals induced out of the ground state has been attempted. Since the AFM ground state shows magnetization $\langle \hat{S}^x_j \rangle = \langle \hat{S}^z_j \rangle = 0$, spin flip excitations do not result in a signal in magnetizations. Time evolution has therefore been performed under a Hamiltonian with same parameters J and J^z, but now with a local magnetic field $h^z_j > 0$ in z on one or two sites in the center of the CMW. The position of these local field(s) in the overall system is constant over time, i.e. with the CMW shifting to the right, the position of the field(s) shift to the left inside the CMW.

λ^A	λ^B
8.03040E-001	6.63187E-001
3.86052E-001	6.63187E-001
2.97038E-001	2.02015E-001
2.97038E-001	2.02015E-001
1.01061E-001	1.08158E-001
7.24340E-002	1.08158E-001
7.24340E-002	6.75682E-002
6.85304E-002	6.75682E-002
2.74290E-002	4.37654E-002
2.74290E-002	4.37654E-002
2.68884E-002	2.43021E-002
1.97280E-002	2.43021E-002
1.90560E-002	1.49002E-002
1.44738E-002	1.49002E-002
1.44738E-002	1.38727E-002
1.32905E-002	1.38727E-002
1.32905E-002	8.05530E-003
1.31851E-002	8.05530E-003
7.51960E-003	6.51760E-003
7.51960E-003	6.51760E-003

Table 6.1.: Schmidt values of the 2-site unit cell iMPS for the XXZ AFM ground state with $J = 1$ and $J^z = -1.2$. The first 20 Schmidt values for each set are shown, whereas a number of kept states $m = 200$ has been used for the computation. It is clearly evident that both sets of Schmidt values show degeneracy.

Starting at $t = 0$, signals are generated at this position, which travel left and right, where again the right going branch has been followed. Window movement has been performed with a fixed velocity v_f.

Unfortunately however, the time evolution did not yield any viable results. Strong perturbations are induced at the front boundary immediately, constantly propagating into the window and distorting the signal of interest. The reason for this is not yet understood. As of now, it is believed that the degeneracy in Schmidt values is the reason for these perturbations. In fact, the nature of these perturbations is similar to those one would get if no phase convention (cf. Section 5.4) is implemented for the CMW method. However the present perturbations arise despite the use of a proper phase convention. An example of a simulation, where a magnetic field $h^z_j = 5$ has been switched on at $t = 0$ at site $j = \frac{L}{2}$ is shown in Figure 6.12. The CMW has not been moved along during the simulation, the perturbations arise nevertheless and are thus no relic of window movement.

It has been tried to eliminate the perturbations by implementing an additional ordering of Schmidt vectors in the respective degenerate subspaces after each SVD. Otherwise the ordering of Schmidt vectors would be random within their respective subspaces and copying and joining of MPS matrices with different (because random) ordering should generate such perturbations. A unique ordering by position of the coefficient with largest magnitude of Schmidt vectors in each degenerate subspace has been implemented, which however could not solve the problem as the results remained the same. The true cause of the perturbations is thus as of now still unclear and is currently subject of further investigation.

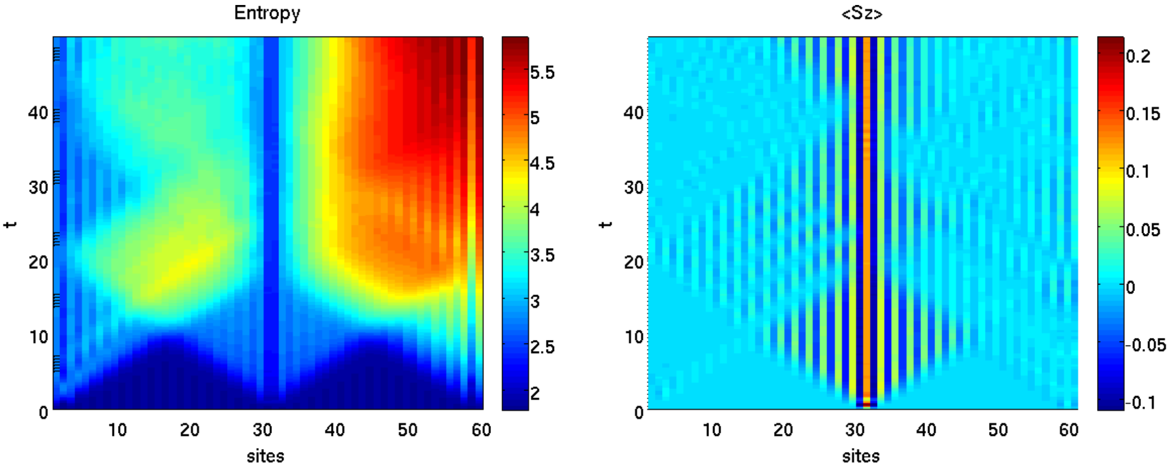

Figure 6.12.: Timelines of bipartite entanglement entropy $S_{ent}(t)$ (cf. (3.40)) and magnetization $\langle \hat{S}_j^z(t) \rangle$ for the evolution of the AFM ground state under a time dependent Hamiltonian. The AFM ground state of the XXZ chain for $J = 1$, $J^z = -1.2$ and $h^z = 0$ has been evolved under a Hamiltonian with the same parameters, but $h_j^z = 5$ for $j = \frac{L}{2}$ with $\tau = 0.01$ and $m = 200$. Unphysical perturbations are induced almost instantly at both boundaries of the CMW, constantly propagating into the CMW and distorting the signal of interest. It is also apparent that the perturbations are not generated symmetrically.

6.3. Transverse Ising Model

As a final application, the CMW has been tested for the TIM (cf. Section 2.3). Out of the thermodynamic limit ground state, various signals have been induced and their propagation has been studied. For the case of a single JW excitation (cf. Section 2.3) the simulated results for the magnetization $\langle \hat{S}_j^z(t) \rangle$ have been compared with the exact result (2.50). Other investigated signals include single spin flips as well as domain walls.

Again, this type of signals decays into a left and right going branch, where the right going branch has been followed by triggering window movement with the relative growth in bipartite entanglement entropy (3.40). The dependence of the signal propagation velocity on the model parameters J and h as well as the evolution of signal shapes over time has been investigated.

Simulations have been performed below the critical point $h < h_c = \frac{J}{2}$ and the Ising interaction parameter J has been kept constant at $J = 1$ at all times and only the transverse field strength h has been varied.[3]

6.3.1. Removing the Degeneracy in the Calculated Thermodynamic Limit Ground State

The thermodynamic limit ground state for the TIM is essentially the vacuum state in terms of Bogoliubov fermions (cf. Section 2.3). As it cannot be encoded in an iMPS in a straightforward way, it has been computed using iDMRG (cf. 4.1.1) with a proper convergence criterion (4.34) of $1 - F < 10^{-14}$ (cf. Section 4.1.2).

The thermodynamic limit ground state below the critical point in fact shows an expectation value $\langle \hat{S}_j^x \rangle = 0$, even though the magnetization in x is the order parameter that goes to 0 with $h \to h_c$. This is due to the Z_2 symmetry around the x-axis present in the system, which causes the ground state to consist of a linear combination of two equivalent states with opposite magnetization in x in the thermodynamic limit, resulting in zero net magnetization. This fact is reflected in the degeneracy of the Schmidt values after iDMRG convergence. To lift this degeneracy, a magnetic interaction $-h^x \hat{S}_j^x$ along x has been included in the model and a small symmetry breaking magnetic field h^x has been applied during the first few steps of the iDMRG run only. This causes the iDMRG algorithm to decide on one of the two possible magnetization directions and to fully converge to the corresponding state with finite magnetization. The ground state energies are identical up to machine precision for both cases. An example for Schmidt values for a TIM ground state with and without symmetry breaking field h^x for transverse field strength $h = 0.2$ is given in Table 6.2.

This behavior of the ground state can also be seen for the finite size case. Due to boundary effects the symmetry is only broken if the system is sufficiently large, below this critical size the magnetization along x vanishes *despite* the small symmetry breaking field, whereas the magnetization along z is always finite, showing boundary effects. This critical size depends on the value of h^x, but also on the transverse field strength h as the

---

[3] This is sufficient with the same argument as for the XXZ chain (cf. Section 6.2).

$h_x = 10^{-4}$	$h_x = 0$
9.99941E-001	7.07065E-001
1.08947E-002	7.07065E-001
1.18702E-004	7.70373E-003
1.29331E-006	7.70373E-003
1.29330E-006	8.39349E-005
1.41003E-008	8.39349E-005
1.40909E-008	9.14501E-007
1.57834E-010	9.14501E-007
1.53711E-010	9.14501E-007
1.53425E-010	9.14501E-007

Table 6.2.: Schmidt values for the thermodynamic limit ground state of the TIM for $h = 0.2$ and $m = 30$, where only the first 10 Schmidt values are shown. For $h_x = 0$ the Schmidt values are clearly degenerate and decay much slower than for the symmetry breaking case, where a small field $h^x = 10^{-4}$ has been applied during the first few iDMRG steps.

correlation length increases dramatically with h close to h_c. An example of boundary effects for the finite size TIM with $L = 80$ sites is given in Figure 6.13, where the ground state and magnetizations have been calculated using regular finite size DMRG (cf. Section 4.1.3). Symmetry breaking fields have again been applied during the first few iDMRG steps for growing the initial L-site system only.

The fact that boundary effects already reach very far into a finite system for transverse field strengths not so close to h_c shows, that it is indeed best to study the propagation of local signals on an infinite system. The CMW method is therefore an excellent tool to study signal propagation in the bulk of a Transverse Ising chain.

After computing the thermodynamic limit ground state with broken symmetry to get finite positive magnetization in x, the derived 2-site unit cell has been canonized according to Section A.1. An L-site CMW has then been filled with the canonized unit cell in order to induce local signals in the center.

6.3.2. Time Evolution of JW Excitations

In order to be able to compare the simulated data to exact results, the first signal to be investigated was a JW excitation to the ground state (cf. Section 2.3), which has been induced according to (A.20). *The initial state therefore has the character of a single spin flip in z and a domain wall in x.*

Simulations have been performed for various transverse field strengths $h < h_c$ up to $t = 300$. Attention has to be paid to the case h close to h_c. In order to avoid perturbations at the front boundary, which are caused by broken translational invariance due to long range correlations, the size of the CMW and the margin between signal and front boundary has been increased as h gets closer to h_c. Magnetization timelines for

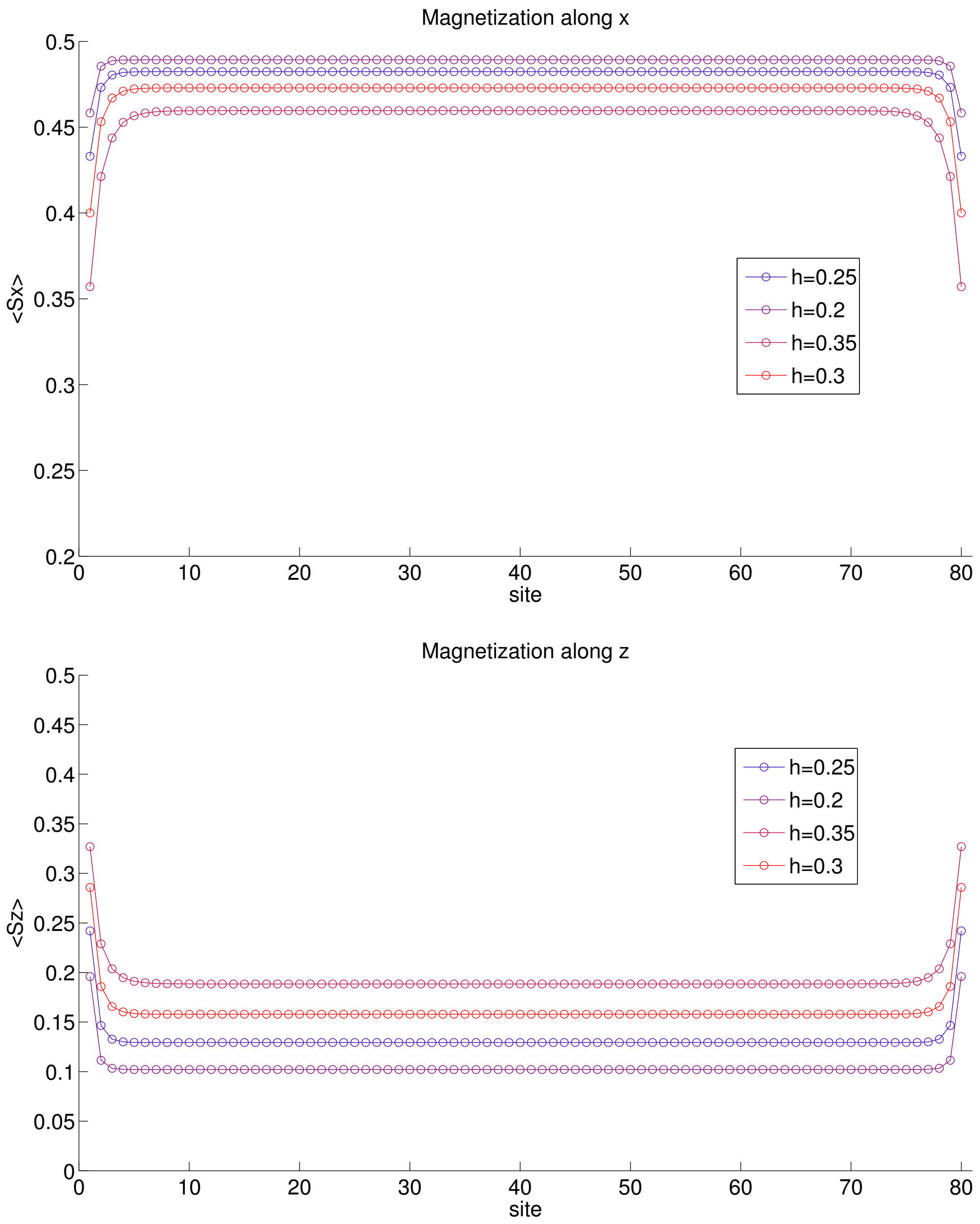

Figure 6.13.: Boundary effects for the finite size TIM for $L = 80$ sites and symmetry breaking field $h_x = 10^{-4}$, which has been applied during the first few steps of iDMRG only. Shown are magnetizations $\langle \hat{S}^x_j \rangle$ and $\langle \hat{S}^x_j \rangle$ for transverse field strengths $h = 0.2, 0.25, 0.3, 0.35$. Whereas $\langle \hat{S}^z_j \rangle$ increases with h, $\langle \hat{S}^x_j \rangle$ decreases. If h is too close to h_c, $\langle \hat{S}^x_j \rangle$ vanishes due to boundary effects despite the symmetry breaking field, which would e.g. already be the case for $h \approx 0.4$ here.

$\langle \hat{S}^x_j(t) \rangle$ and $\langle \hat{S}^x_j(t) \rangle$ can be seen in Figure 6.14. The watched bond j inside the CMW for triggering the window movement has been chosen as $j = \frac{2L}{3}, \frac{2L}{3}, \frac{3L}{5}$ for $h = 0.2, 0.3, 0.4$. This choice also holds for all subsequently investigated signal types.

The simulations show that the CMW method is indeed able to efficiently remove finite size boundary effects up to very large simulation times, which would clearly be present in a finite size system. However, with h getting close to h_c it becomes more difficult to eliminate perturbations at the front boundary at all times, as window size and margin between the signal and the front boundary have to become very large.

Signal Velocity

Both the domain wall in x and the single spin flip in z decay and propagate with a characteristic signal velocity v_h, which depends on the transverse field strength h. Since window movement has again been triggered with the rise in bipartite entanglement entropy (3.40), the signal velocity has been identified with the velocity of the window.

v_h has therefore been calculated as

$$v_h = \frac{x_d}{t_d} = \frac{nN_s}{t_N - t_1}, \tag{6.8}$$

where N_s is the number of sites in a unit cell, n is the total number of CMW shifts during the simulation and t_j is the time of the j^{th} shift. For the uncertainty of v_h we get

$$\Delta v_h = v_h \sqrt{\frac{(\Delta x_d)^2}{x_d^2} + \frac{(\Delta t_d)^2}{t_d^2}}, \tag{6.9}$$

where $\Delta x_d = N_s$ and $\Delta t_d = \tau N_{meas}$ are the uncertainties of x_d and t_d and N_{meas} is the number of time evolution steps between measurements.

The simulated data shows a linear dependence of the velocity $v_h = h$, as can be seen in Table 6.3, where velocities for 6 different values of h from $h = 0.2$ to $h = 0.45$ have been estimated. This relation has been found to also hold for all other signal types investigated for the TIM, which agrees with the results in [12]. A surface plot of the bipartite entanglement entropy (3.40) for $h = 0.3$ can be seen in Figure 6.17.

Comparison to Exact Results

As a next step, the simulated data has been compared to the exact result (2.50) for the magnetization $\langle \hat{S}^z_j(t) \rangle$ for different transverse field strengths h and times t. Comparisons for $h = 0.2, 0.4$ and $t = 100, 150, 200$ can be seen in Figures 6.15 and 6.16. Again, the simulated data and the exact results are in very good agreement, also at large simulation times. For both field strengths, largest relative deviations again arise at the rear boundary after the impact of the left going signal branch, where they are of the order $\mathcal{O}(10^{-2})$ at worst. These perturbations are again restricted to the first few sites into the window at all times.

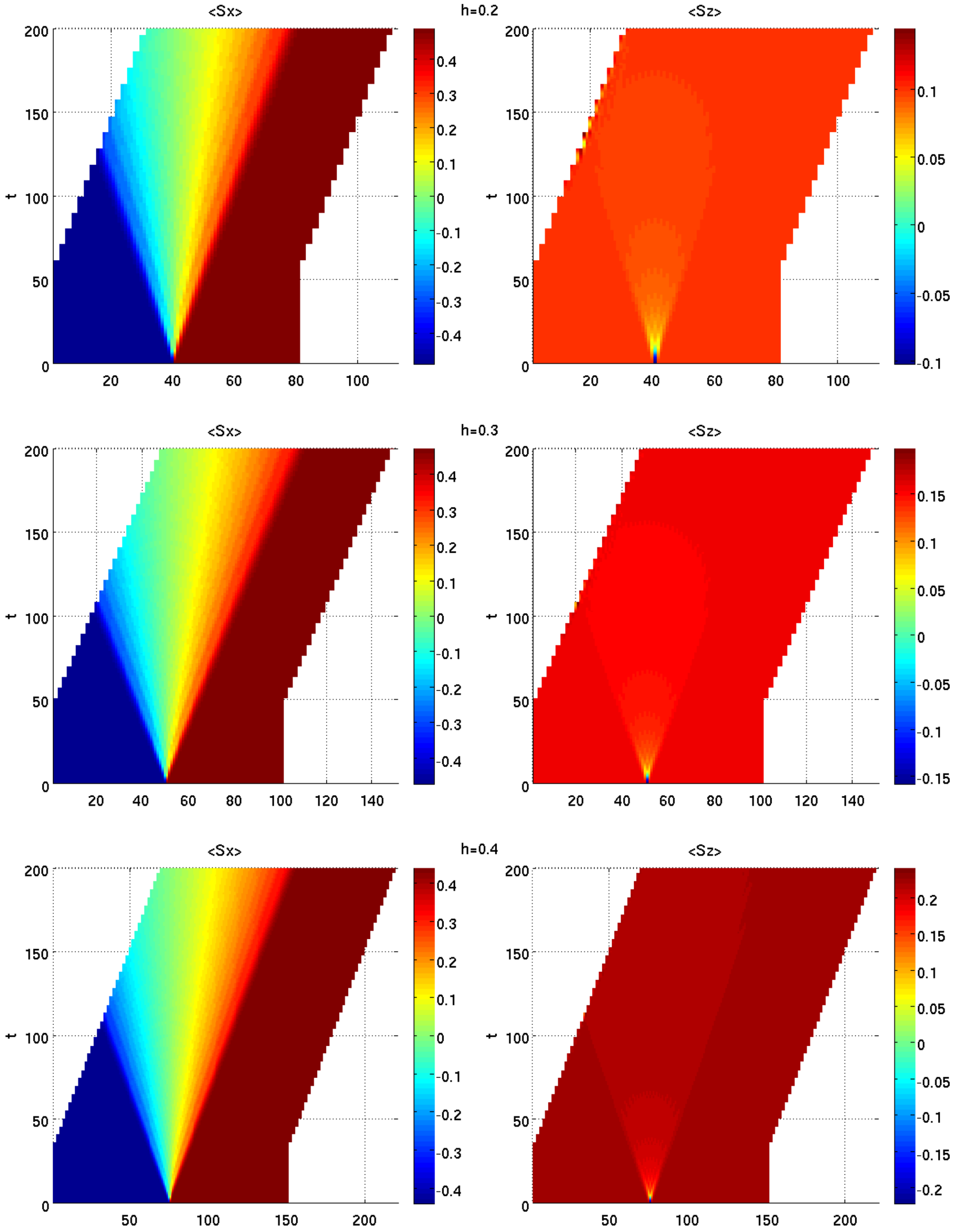

Figure 6.14.: Magnetizations $\langle \hat{S}_j^x(t) \rangle$ and $\langle \hat{S}_j^z(t) \rangle$ of a JW excitation to the TIM for transverse field strengths $h = 0.2, 0.3, 0.4$ with $\tau = 0.01$ and $m = 12, 12, 24$ up to $t = 200$. Both the domain wall in x and the spin flip in z decay with a characteristic signal velocity v_h dependent on h.

h	v_h
0.20	0.21 ± 0.01
0.25	0.25 ± 0.01
0.30	0.31 ± 0.01
0.35	0.36 ± 0.01
0.40	0.41 ± 0.01
0.45	0.46 ± 0.01

Table 6.3.: Velocity of the signal front for a JW excitation for different transverse field strengths h. The linear dependence of $v_h = h$ is clearly evident. The slightly higher values of v_h are again due to the exponentially suppressed tails of bipartite entanglement entropy reaching beyond the light cone.

For $h = 0.2$ relative deviations everywhere inside the window are as small as $\mathcal{O}\left(10^{-6}\right)$ at all times, even at the front boundary. For $h = 0.4$ correlations already cause very slight perturbations at the front boundary, where translational invariance gets slightly disturbed at larger simulation times. These perturbations however don't stack up as they travel into the window, relative deviations therefore never rise above $\mathcal{O}\left(10^{-4}\right)$ and the signal front remains basically unperturbed. To minimize these perturbations, one needs to use very large window sizes and signal-boundary margins.

Comparisons to exact results have only been made for $\langle \hat{S}_j^z(t) \rangle$, as an analytic expression for $\langle \hat{S}_j^x(t) \rangle$ could not have been derived. This due to a complicated product structure arising from JW phase factors.

Signal Shape: Scaling

The shape of the rise in magnetization at the domain wall in x has been further investigated. A plot of the magnetizations at different times t_i from $t = 50$ to $t = 300$ for $h = 0.3$ can be seen in Figure 6.18, where the times t_i are the times immediately after CMW shifts. There is a characteristic drop/rise of magnetization at the boundaries of the light cone, whereas inside the light cone the magnetization depends almost linearly on the position.

Figure 6.18 shows that the width of the domain wall increases linearly with time. In order to compare its shape at different times, the position axis inside the window has been rescaled accordingly with time. For the magnetizations to maximally overlap, scaling has been centered around the center of the light cone, which is at $x_0 = \frac{L}{2} + \frac{1}{2}$ for the domain wall. The rescaled positions $x_j(t_i)$ at time t_i is then

$$x_j(t_i) = \frac{x_j(t_0) - x_0}{t_i}, \tag{6.10}$$

where $x_j(t_0)$ is the unscaled position at time $t_0 = 0$. The scaled positions are now centered around the origin.

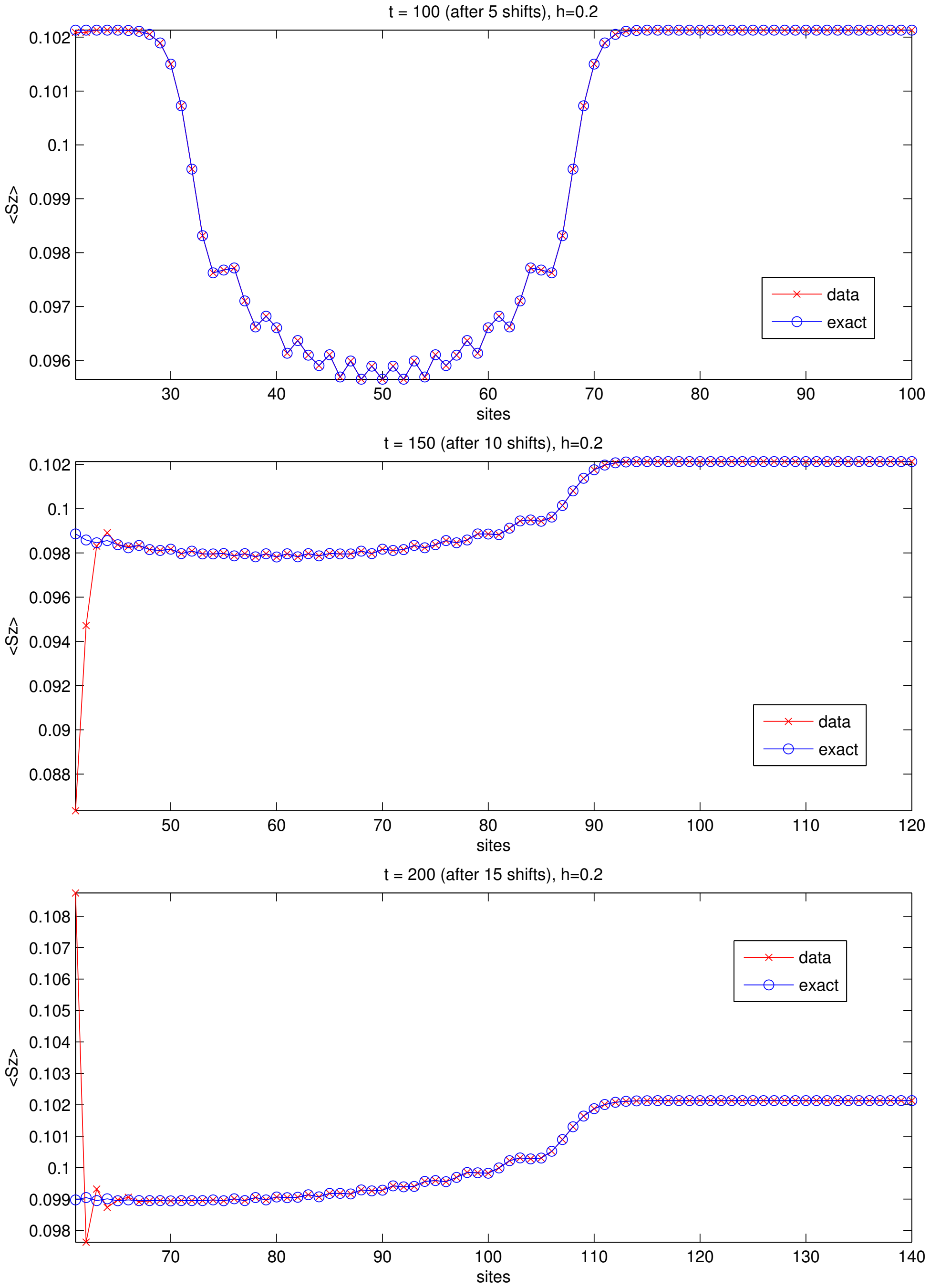

Figure 6.15.: Comparison of the magnetization $\langle \hat{S}_j^z(t) \rangle$ of a JW excitation to exact results (2.50) for $h = 0.2$ at $t = 100, 150, 200$. The comparison shows very good agreement, even for large times. Largest relative deviations arise at the rear boundary and are of the order $\mathcal{O}\left(10^{-2}\right)$. These perturbations are restricted to the first few sites into the window at all times. Everywhere else relative deviations never rise above $\mathcal{O}\left(10^{-6}\right)$.

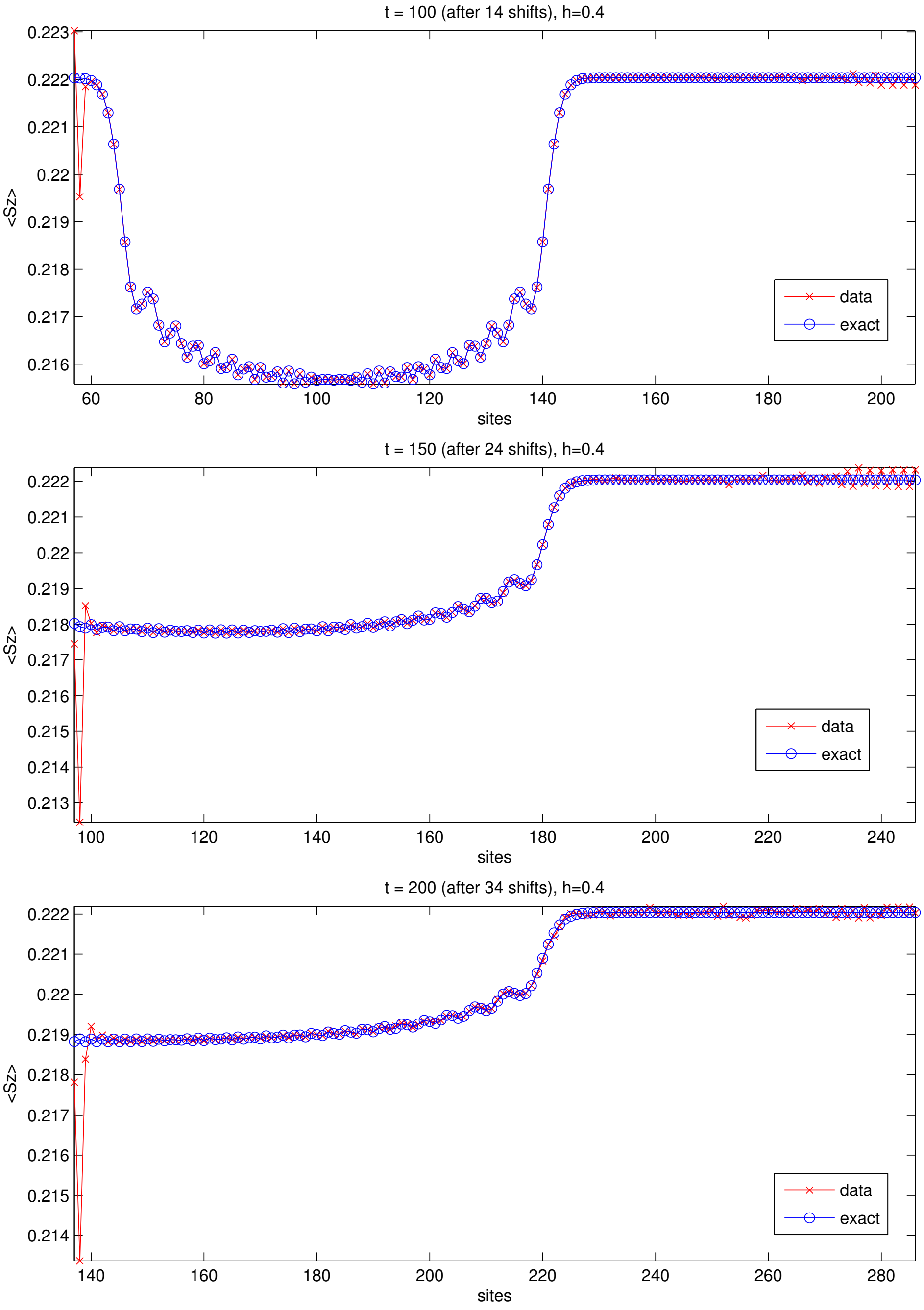

t = 100 (after 14 shifts), h=0.4

t = 150 (after 24 shifts), h=0.4

t = 200 (after 34 shifts), h=0.4

Figure 6.16.: Comparison of the magnetization $\langle \hat{S}_j^z(t) \rangle$ of a JW excitation to exact results (2.50) for $h = 0.4$ at $t = 100, 150, 200$. The comparison again shows good agreement. Largest relative deviations arise at the rear boundary and are of the order $\mathcal{O}\left(10^{-2}\right)$. These perturbations are restricted to the first few sites into the window at all times. At large times, long range correlations have caused small perturbations at the front boundary, which constantly propagate into the window, but are negligible as relative deviations never rise above $\mathcal{O}\left(10^{-4}\right)$ there.

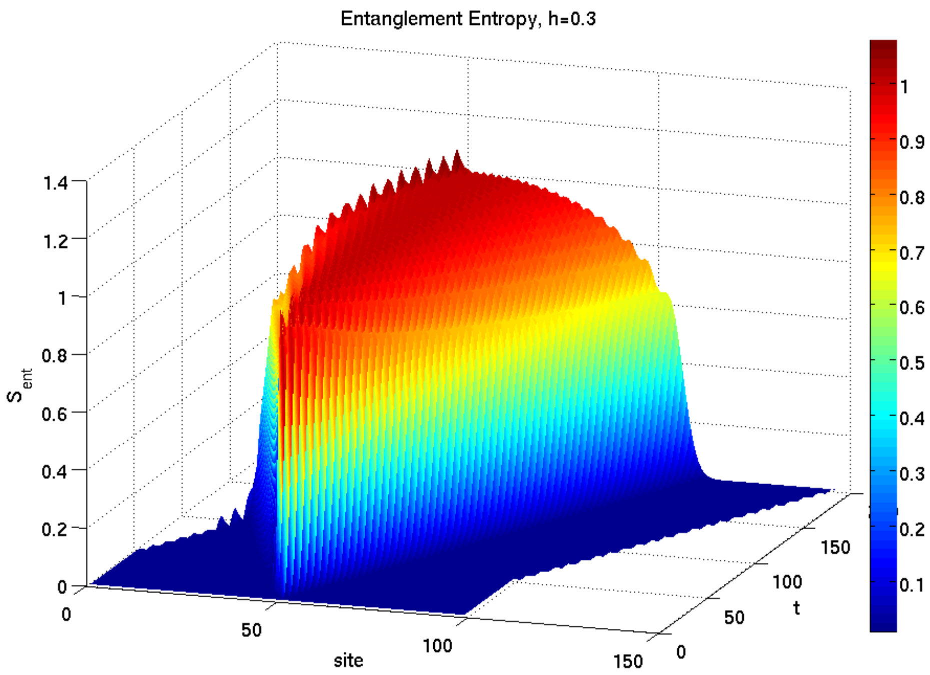

Figure 6.17.: Bipartite entanglement entropy (3.40) for a JW excitation to the TIM for $h = 0.3$. The initial JW excitation causes an almost immediate jump of entanglement entropy at the center of excitation to $S \approx 1$. The entanglement then spreads with the signal velocity, while entanglement entropy in the center stays almost constant. The exponentially suppressed tails reaching beyond the effective light cone can be seen, especially for larger times. This entanglement entropy structure is characteristic also for all other investigated signal types.

The scaled time slices overlap indeed very nicely. However the characteristic drops in magnetization do not scale linearly and the shape as well as the magnitude of the drop vary over time. This can be seen in Figure 6.18. The evolution of the scaled width and magnitude of these drops over time has been further investigated. To define the width of the drop, a starting point where magnetization starts to drop below the magnetization outside the light cone, needs to be identified. This has been done by identifying the points, where magnetization drops by a certain relative threshold amount $\epsilon = 10^{-3}$ below the magnetization outside the light cone. As end point of the drop, the first local minimum in magnetization after the drop has been identified. Notice that for the right going signal front, the starting points are thus to the right of the end points (cf. also Figure 6.19, where starting and end points are marked as upper and lower triangles).

The scaled position $x_{s,e}(t_i)$ of both end point and starting point, as well as the magnetization $M(t_i) = \langle \hat{S}^x(x_e(t_i), t_i) \rangle$ at the end point have been estimated by using cubic spline interpolations. From these points the scaled width $d(t_i) = x_s(t_i) - x_e(t_i)$, as well

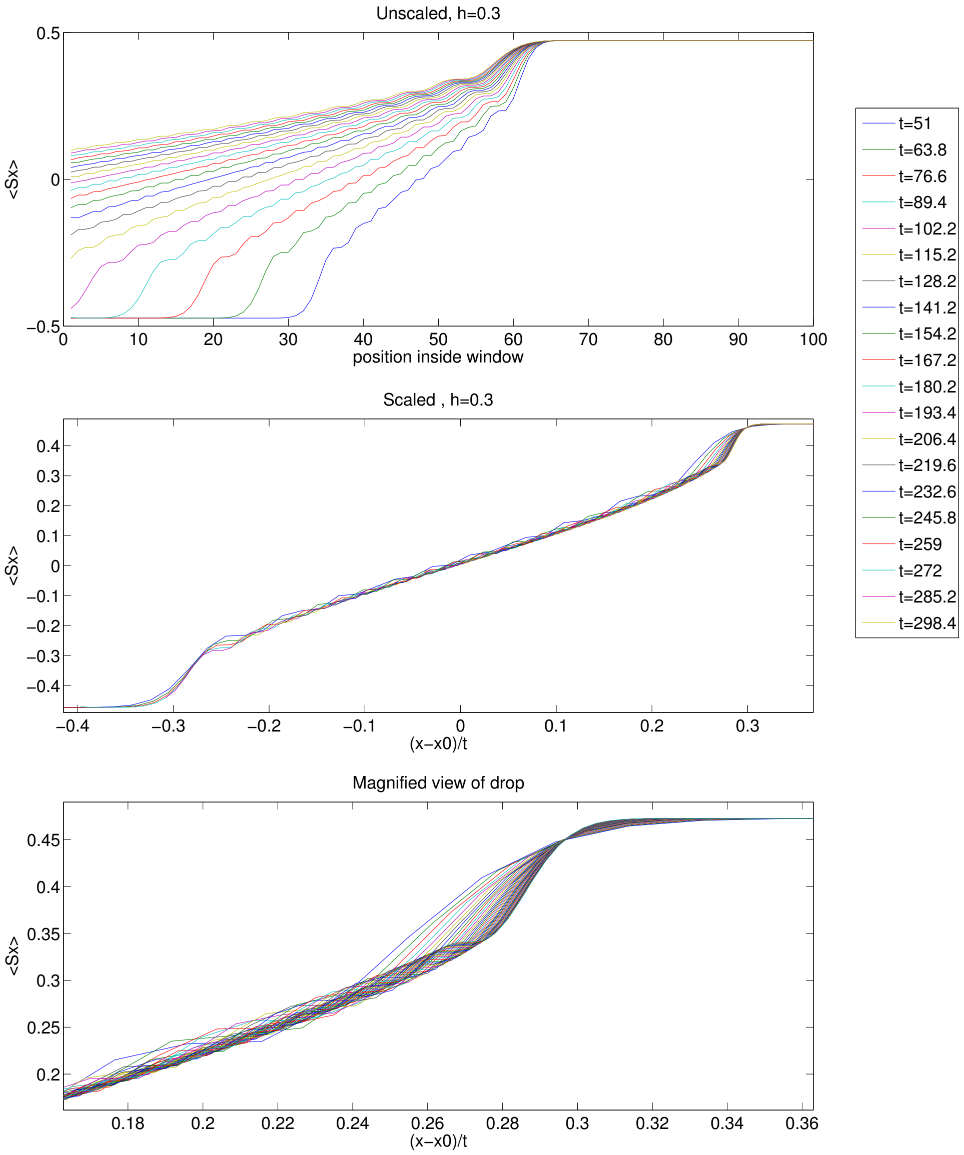

Figure 6.18.: Magnetization profiles $\langle \hat{S}^x_j(t)\rangle$ of a JW excitation on the TIM for $h = 0.3$ at different times t. The top panel shows the unscaled magnetizations at different times. Here the horizontal axis marks position inside the CMW. The middle panel shows the scaled time slices, where the position axis has been scaled according to (6.10) with $x_0 = \frac{L}{2} + \frac{1}{2}$. Whereas the region of linear rise in magnetization as well as the total width of the rise scale linearly with time and thus overlap well, the characteristic drops at the light cone boundaries do not. They vary over time in scaled width and magnitude. The bottom panel shows a magnified view of the characteristic drops.

as the magnitude $\Delta M(t_i) = M_0 - M(t_i)$, with M_0 the magnetization outside the light cone, have been determined for each time t_i. The spline interpolations with starting and end points, as well as the scaled width, magnitude and scaled starting point for each time t_i can be seen in Figure 6.19, where now 24 time slices from $t = 50$ to $t = 300$ have been used to get a better analysis. It is clearly evident that neither the scaled width nor the magnitude of the drops scale linearly with time. This explains the different shapes in the scaled comparison in Figure 6.18. It appears however, that all quantities converge to a constant value for very large times. A power law fit to the model function

$$y(t) = at^{\alpha} + c \tag{6.11}$$

indeed yield negative exponents $\alpha_d = -0.67 \pm 0.01$ and $\alpha_M = -0.359 \pm 0.002$ for width and magnitude, suggesting convergence of both quantities to constant values $d_\infty = 0.001 \pm 0.001$ and $\Delta M_\infty = 0.008 \pm 0.001$, i.e. they (almost) vanish with $t \to \infty$. The starting point x_s of the drop also shows convergence to the constant value $x_{s\infty} = 0.299 \pm 0.001$ with a negative exponent $\alpha_{x_s} = -0.65 \pm 0.01$. These results suggest, that the drop vanishes both in width and magnitude, with the scaled starting point of the signal itself converging to a value corresponding to the signal velocity $v_h = h = 0.3$ as expected (remember that x_s is scaled with t, effectively being a velocity).

The above results lead to the conjecture that the scaled signal shape converges for $t \to \infty$. The asymptotic shape of the signal front with has therefore been estimated by extrapolating the scaled positions of magnetization values in a certain interval from $\langle \hat{S}^z \rangle = 0.35$ to $\langle \hat{S}^z \rangle = 0.45$ for $t \to \infty$ from fits according to the above model function (6.11). This limiting shape can be seen in Figure 6.19 for magnetization values between as a red dashed curve.

6.3.3. Time Evolution of Single Spin Flips

As next signal type, single spin flips in x and z have been studied. Due to the attached JW phase factor for the spin flip operators (A.18) and (A.16), the derivation of an analytic expression for the magnetizations $\langle \hat{S}^x_j(t) \rangle$ and $\langle \hat{S}^z_j(t) \rangle$ would be much more difficult and was therefore not performed here. Simulations have been performed for both signal types for various transverse field strengths h.

A *spin flip in x* causes the formation of a region with effectively lowered magnetization in x. The boundaries of this region propagate to both directions with the signal's velocity v_h. The excitation in magnetization $\langle \hat{S}^x_j(t) \rangle$ is therefore like the propagation of two effective domain walls.

The nature of the TIM Hamiltonian also causes a coupling to magnetization in z, resulting in magnetization oscillations within the signal's light cone, even though nothing has been induced there. Notice that this excitation doesn't reach its maximum until $t \approx 2$, whereas for the excitation in x the maximum occurs at $t = 0$, i.e. the initial excitation. Results for magnetizations $\langle \hat{S}^x_j(t) \rangle$ and $\langle \hat{S}^z_j(t) \rangle$ can be seen in Figure 6.20.

A *spin flip in z* causes a similar type of oscillation in the magnetization $\langle \hat{S}^z_j(t) \rangle$ as a spin flip in x, however its maximum is now at $t = 0$. Notice, that a spin flip in z is also

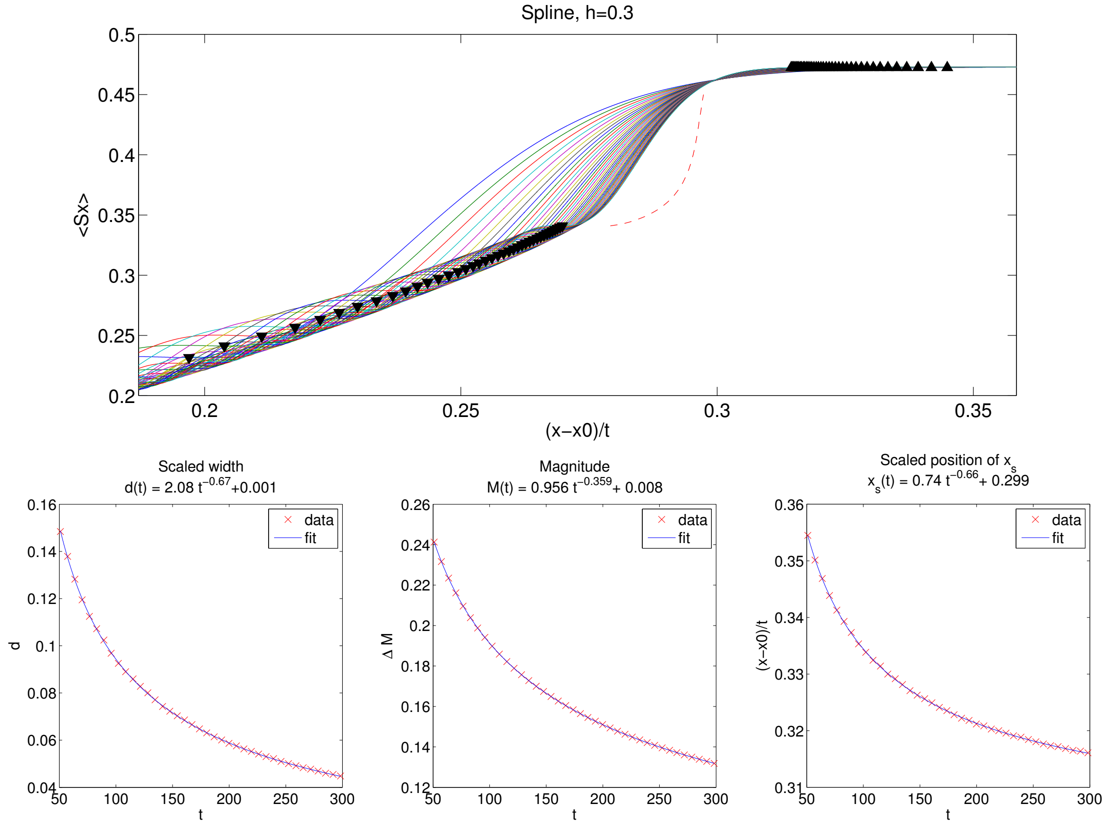

Figure 6.19.: Spline interpolations of the characteristic drop in magnetization in x for 24 time slices from $t = 50$ to $t = 300$ for a JW excitation on the TIM at $h = 0.3$. The first local minima of magnetization after the initial drop are taken to be the end point of the drop at each time, they are marked as lower triangles in the plot. The starting point at each time is taken to be the points where magnetization drops by a threshold amount $\epsilon = 10^{-3}$ below the value outside the light cone, they are marked as upper triangles. Notice that for right going signal fronts, the starting points are to the right of the ending points. It can be seen that the position where magnetization $\langle \hat{S}^x \rangle \approx 0.46$ scales almost linearly with time, as all magnetization profiles intersect around this point. The scaled width, magnitude and scaled starting point of the drop over time can be seen in the bottom panel. They seem to follow a power law, fits to the model function $y(t) = at^\alpha + c$ indeed suggest convergence of all three quantities to constant values. The shape of the drop in the limit $t \to \infty$ has been estimated by extrapolating the scaled positions of magnetization values in a certain interval. This is shown in the top panel as a red dashed curve.

part of a JW excitation, however without the initial domain wall in x. The resulting timeline for $\langle \hat{S}^z_j(t) \rangle$ therefore looks much different, as there were no oscillations for the JW excitation. Again, an excitation is also caused for $\langle \hat{S}^x_j(t) \rangle$, which looks very similar to a spin flip in x, even though nothing has been induced there. However in this case the effective drop in magnetization is much smaller than for a spin flip in x. Results can be seen in Figure 6.21.

Signal Shape: Scaling

The region of effective drop in magnetization in x for both types of spin flips shows a similar linear scaling behavior in time as the domain wall in x for a JW excitation. It has thus been investigated the same way (cf. Section 6.3.2). The magnetization timelines for spin flips in z were however not used for scaling analysis, due to a bad signal to noise ratio. Therefore only spin flips in x were investigated. The position axis has again been rescaled around the center of the light cone according to (6.10), which lies at $x_0 = \frac{L}{2}$. The general shape of the excitation scales linearly with time also for this signal type, while the characteristic drops around the light cone boundaries do not. The unscaled time slices as well as the scaled time slices and a magnified view of the characteristic drop for $h = 0.4$ can be seen in Figure 6.22.

The scaled width, magnitude and scaled starting point of the drop over time have been determined as described in Section 6.3.2 for 24 different times from $t = 50$ to $t = 300$. The results are shown in Figure 6.23. Again, all three quantities seem to follow a power law. Indeed, fits to the model function (6.11) again yield negative exponents $\alpha_d = -0.67 \pm 0.04$, $\alpha_M = -0.17 \pm 0.03$ and $\alpha_{x_s} - 0.73 \pm 0.02$. Again, the drop's width vanishes with $d_\infty = 0.0 \pm 0.1$ whereas the magnitude converges to a large finite jump $\Delta M_\infty = 0.2 \pm 0.1$. The scaled position of the jump converges to $x_{s\infty} = 0.400 \pm 0.001$, complying with $v_h = h = 0.4$. Notice however that the timelines show oscillations and the fits are of limited quality.

Again the above results from the fits suggest a convergence of the signal shape for $t \to \infty$. The asymptotic shape of the drop has been estimated by extrapolation as for the JW excitations (cf. Section 6.3.2) for magnetization values from $\langle \hat{S}^x \rangle = 0.22$ to $\langle \hat{S}^x \rangle = 0.37$ and can be seen in Figure 6.23 as a red dashed curve.

6.3.4. Time Evolution of Domain Walls

As a last signal type, the time evolution of simple domain walls in x have been investigated. A domain wall at bond $j, j+1$ can be induced by starting with the homogeneous ground state and flipping all spins in x left of site $j+1$. In terms of the spin flip operator (A.18) one can write for the operator generating a domain wall

$$\hat{F}_j^w = \prod_{n=1}^{j} \hat{F}_n^x = \prod_{n=1}^{j} \left(2\hat{S}_n^z \right) . \tag{6.12}$$

Notice that this excitation is also part of a JW excitation up to a sign. As for single spin flips, a straightforward analytic expression for the magnetizations $\langle \hat{S}_j^x(t) \rangle$ and $\langle \hat{S}_j^z(t) \rangle$ could not be derived, due to the product structure of $\hat{F}_j^w$.

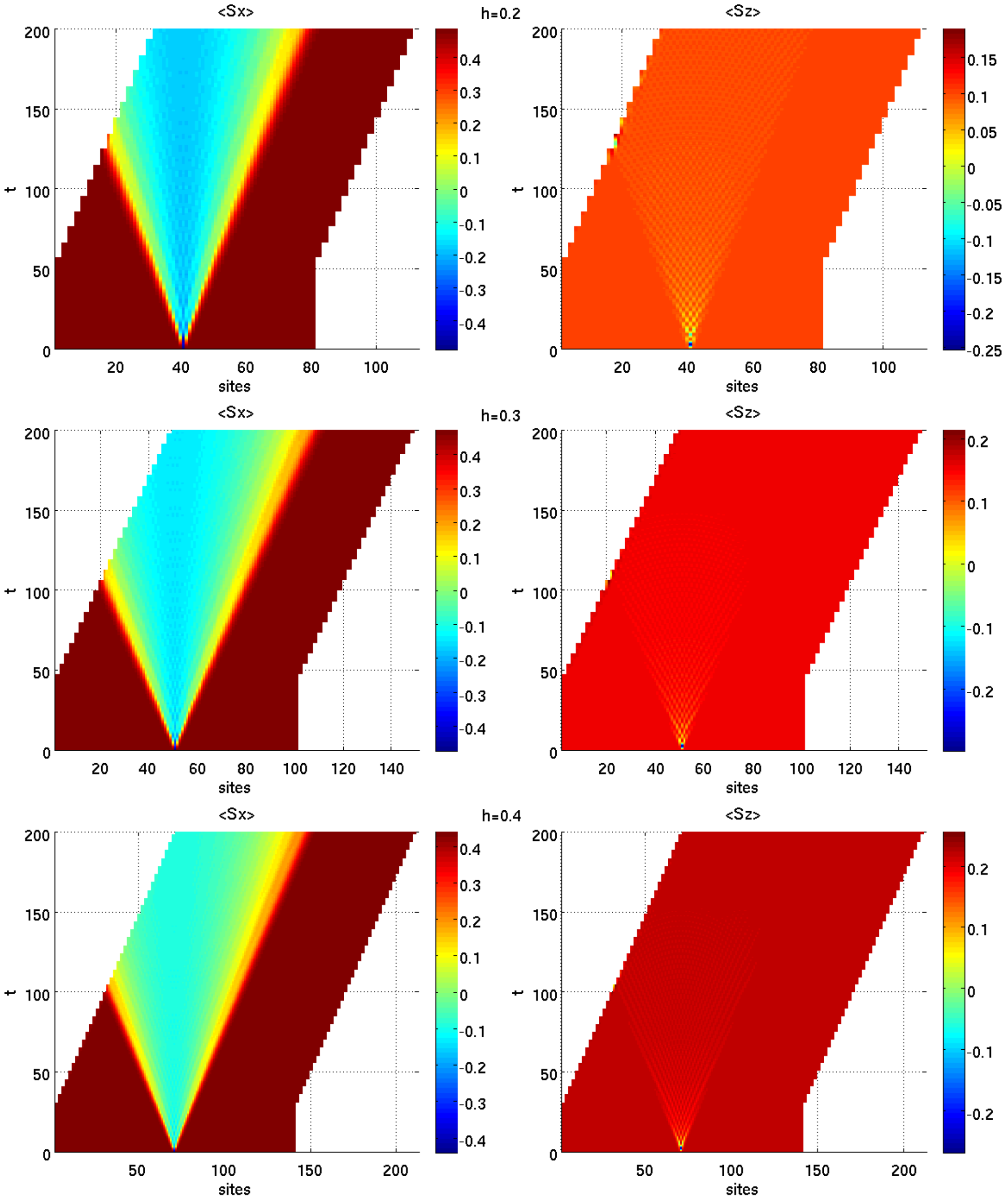

Figure 6.20.: Magnetizations $\langle\hat{S}_j^x(t)\rangle$ and $\langle\hat{S}_j^z(t)\rangle$ for a single spin flip excitation in x on the TIM for $h = 0.2, 0.3, 0.4$ with $\tau = 0.01$ and $m = 14, 14, 26$ up to $t = 200$. Although no excitation in z has been induced, the spin flip in x also causes a considerable excitation in z. In x, the spin flip causes an effective drop of magnetization in a region, whose boundaries spread like two domain walls. In z, the magnetization oscillates within the signal's light cone.

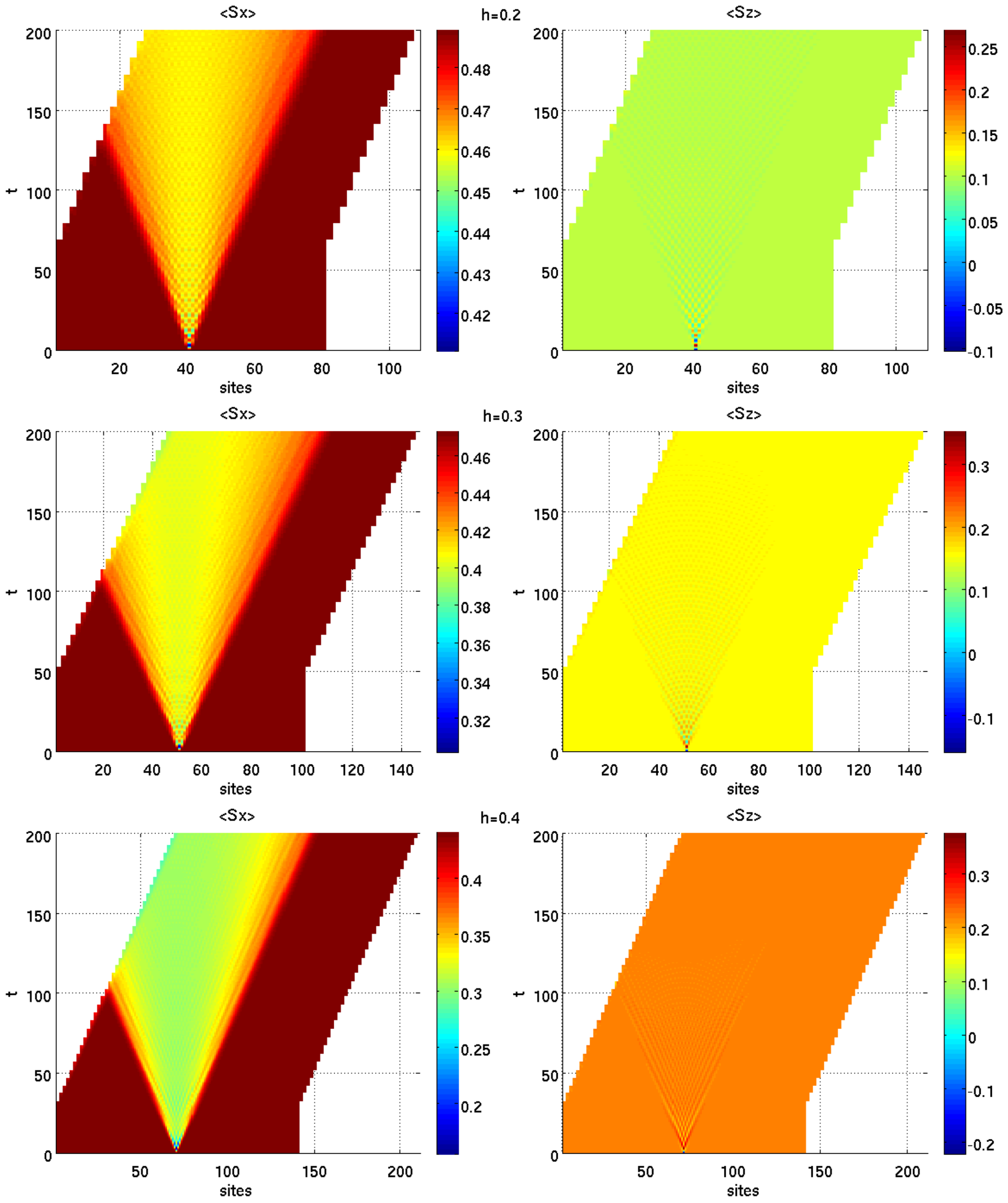

Figure 6.21.: Magnetizations $\langle \hat{S}^x_j(t) \rangle$ and $\langle \hat{S}^z_j(t) \rangle$ for a single spin flip excitation in z on the TIM for $h = 0.2, 0.3, 0.4$ with $\tau = 0.01$ and $m = 14, 14, 26$ up to $t = 200$. Although no excitation in x has been induced, the spin flip in z also causes a considerable excitation in x. In x, the spin flip causes an effective drop of magnetization in a region, whose boundaries spread like two domain walls. In z, the magnetization oscillates within the signal's light cone.

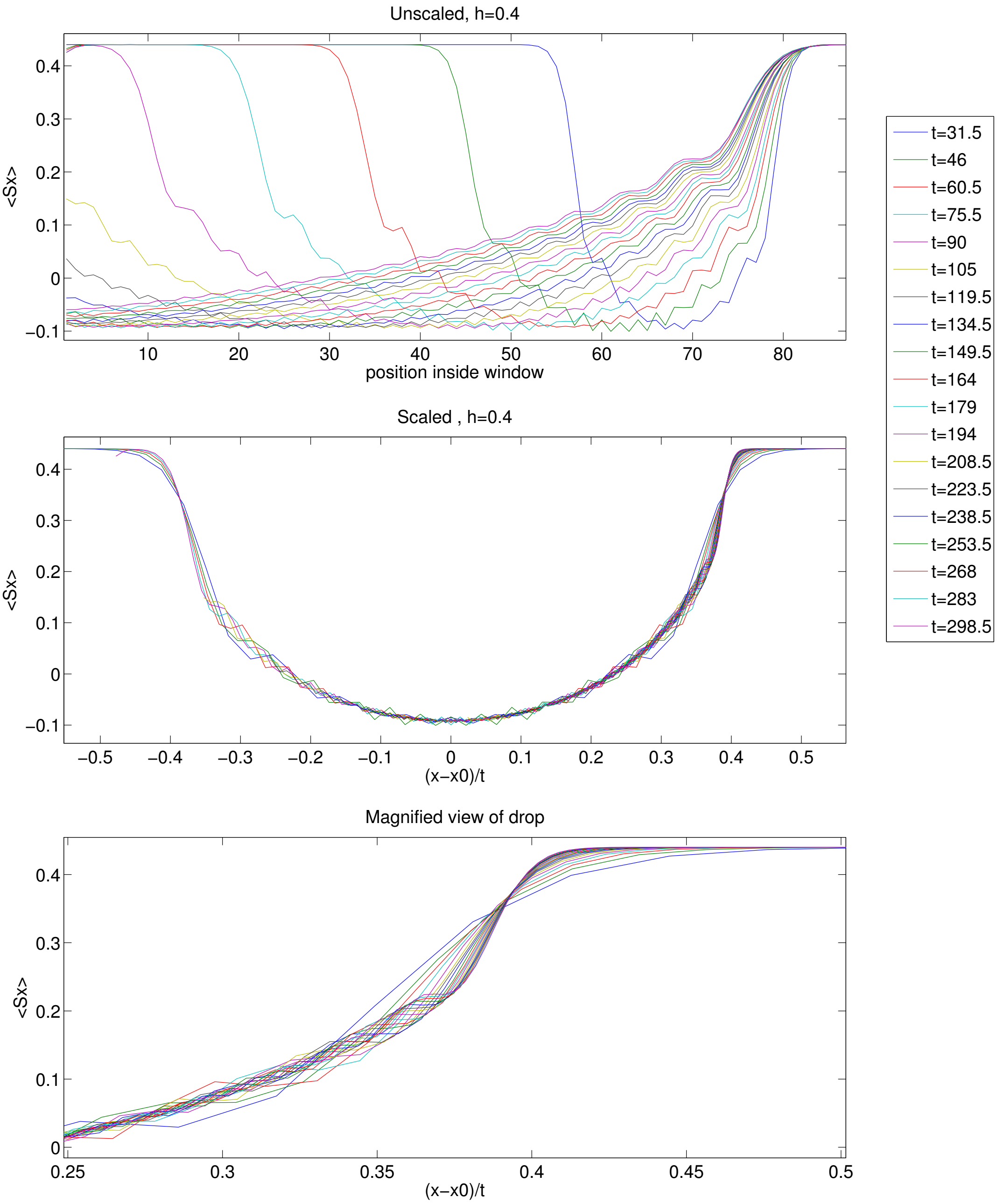

Figure 6.22.: Magnetization time slices in x of a spin flip in x on the TIM for $h = 0.4$. The top panel shows the unscaled magnetizations time slices at different times, the horizontal axis marks position inside the CMW. The middle panel shows the rescaled time slices, where the position axis has been scaled according to (6.10) with $x_0 = \frac{L}{2}$. Whereas the general shape, as well as the total width of the signal scale linearly with time and thus overlap well, the characteristic drops at the light cone boundaries do not. They vary over time in scaled width and magnitude. The bottom panel shows a magnified view of the characteristic drops.

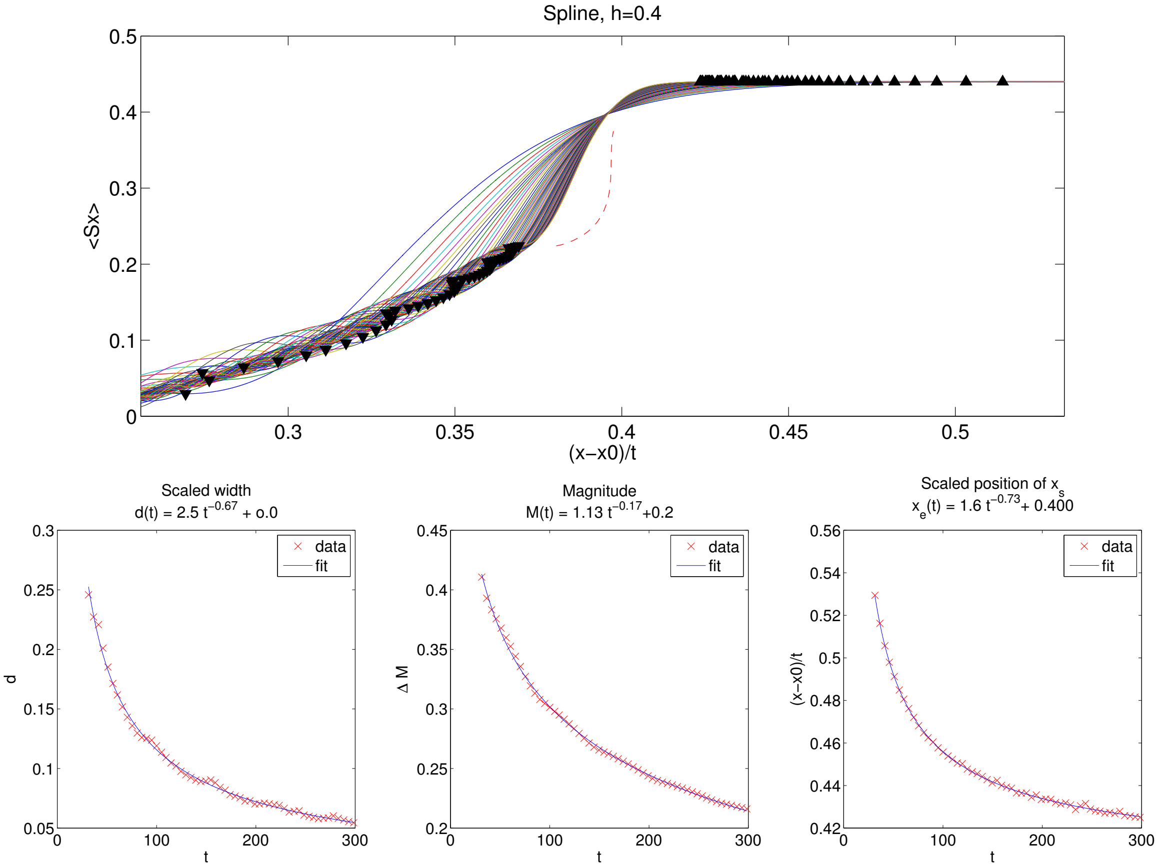

Figure 6.23.: Spline interpolations of the characteristic drops in magnetization for 24 time slices from $t = 50$ to $t = 300$ for a spin flip in x on the TIM at $h = 0.4$. The first local minima of magnetization after the initial drop in magnetization are taken to be the end points of the characteristic drops, they are marked as lower triangles. The starting points are taken to be the points where magnetization drops by a threshold amount $\epsilon = 10^{-3}$ below the magnetization outside the light cone, they are marked as upper triangles. Notice, that for a right going signal front, the starting points are to the right of the end points. As for the JW excitation, there is a value of magnetization $\langle \hat{S}^x \rangle \approx 0.4$, around which all magnetization profiles intersect. The scaled width, magnitude and scaled starting point of the drop over time can be seen in the bottom panel. They do not depend on time linearly, but seem to follow a power law. Fits to the model function $y(t) = at^{\alpha} + c$ indeed suggest convergence of all three quantities to constant values. The shape of the drop in the limit $t \to \infty$ has been estimated by extrapolating the scaled positions of magnetization values in a certain interval. This is shown in the top panel as a red dashed curve.

Simulations have again been performed for several values of h. Results for the magnetization timelines $\langle \hat{S}^x_j(t) \rangle$ and $\langle \hat{S}^z_j(t) \rangle$ can be seen in Figure 6.24. For the magnetization in x one can see that the initial instant jump decays into a nearly linear rise of the magnetization in a region whose boundaries are the light cone of the signal. The domain wall gets “stretched apart”, just as for a JW excitation.

In z, an excitation similar to the above single spin flips gets induced, although the initial oscillation in the center of the light cone decreases and oscillations remain around the light cone boundaries. These oscillations are of small relative magnitude of $\approx 10\%$ of the initial magnetization.

Since the domain wall as a signal is also part of a JW excitation, the magnetization in x with time shows similar scaling behavior with time and has thus been investigated the same way as in Section 6.3.2. We should therefore also expect similar results. Scaling has been performed around $x_0 = \frac{L}{2} + \frac{1}{2}$ like for the domain wall of the JW excitation. The unscaled time slices, as well as the scaled time slices and a magnified view of the characteristic drops can be seen in Figure 6.25. The results of scaling are qualitatively the same as for the domain wall in the JW excitation (cf. Figures 6.18).

The scaled width, magnitude and scaled starting point of the drop over time have been determined as described in Section 6.3.2, now for 25 different times from $t = 50$ to $t = 300$. The results are shown in Figure 6.26. Again, all three quantities show convergence according to a fit to the model function (6.11), yielding negative exponents of $\alpha_d = -0.67 \pm 0.02$, $\alpha_M = -0.32 \pm 0.01$ and $\alpha_{x_s} = -0.76 \pm 0.01$. Both scaled width and magnitude vanish to $d_\infty = -0.001 \pm 0.002$ and $\Delta M_\infty = -0.01 \pm 0.01$, whereas the scaled starting point of the signal itself converges again to $x_{s\infty} = 0.3000 \pm 0.0004$, complying again with $v_h = 0.3$. An extrapolation of the signal shape for $t \to \infty$ did not yield a viable result.

Overall, the same behavior for the characteristic drop as for a JW excitation is recovered qualitatively, however there are quantitative differences in magnitude, which can be seen in Figure 6.27. Whereas the scaled width for the JW excitation and a simple domain wall are basically the same at all times, the drop's magnitude for the JW excitation is always smaller. This difference must arise from the additional spin flip in z induced for a JW excitation.

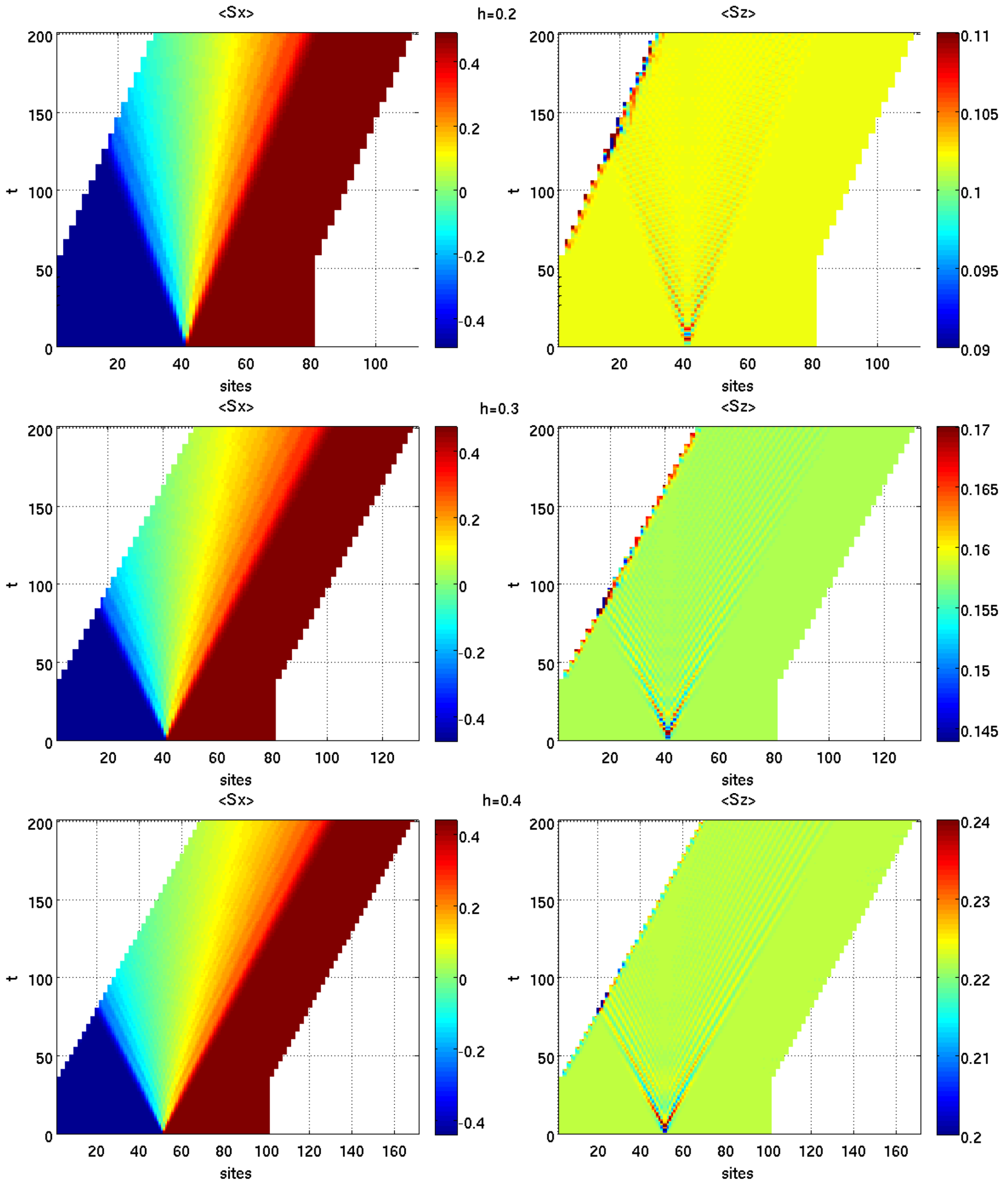

Figure 6.24.: Magnetization timelines $\langle \hat{S}^x_j(t) \rangle$ and $\langle \hat{S}^z_j(t) \rangle$ for the evolution of a domain wall in x on the TIM with $h = 0.2, 0.3, 0.4$, $\tau = 0.01$ and $m = 20, 20, 24$ up to $t = 200$. The domain wall decays into a region where the magnetization rises almost linearly. This region widens with the signal's velocity $v_h = h$. For $\langle \hat{S}^z_j(t) \rangle$, small oscillations are induced, which remain around the signal front and decrease again over time in the center of the excitation.

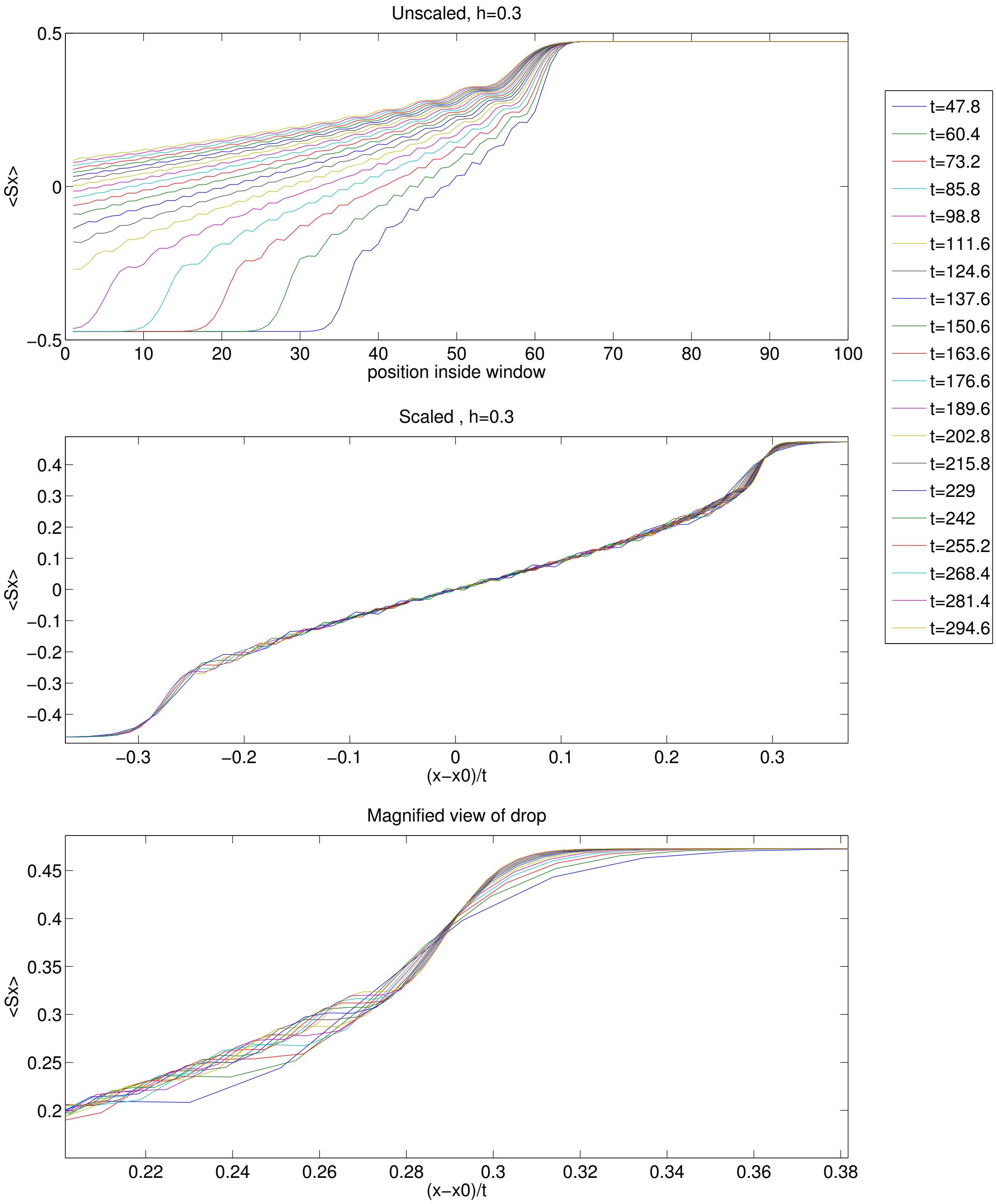

Figure 6.25.: Magnetization time slices in x for a domain wall on the TIM for $h = 0.3$. The top panel shows the unscaled magnetizations at different times, the horizontal axis marks position inside the CMW. The middle panel shows the scaled time slices, where the position axis has been scaled according to (6.10) with $x_0 = \frac{L}{2} + \frac{1}{2}$. The result after scaling is qualitatively the same as for the domain wall of a JW excitation (cf. Section 6.3.2). The bottom panel shows a magnified view of the scaled characteristic drop.

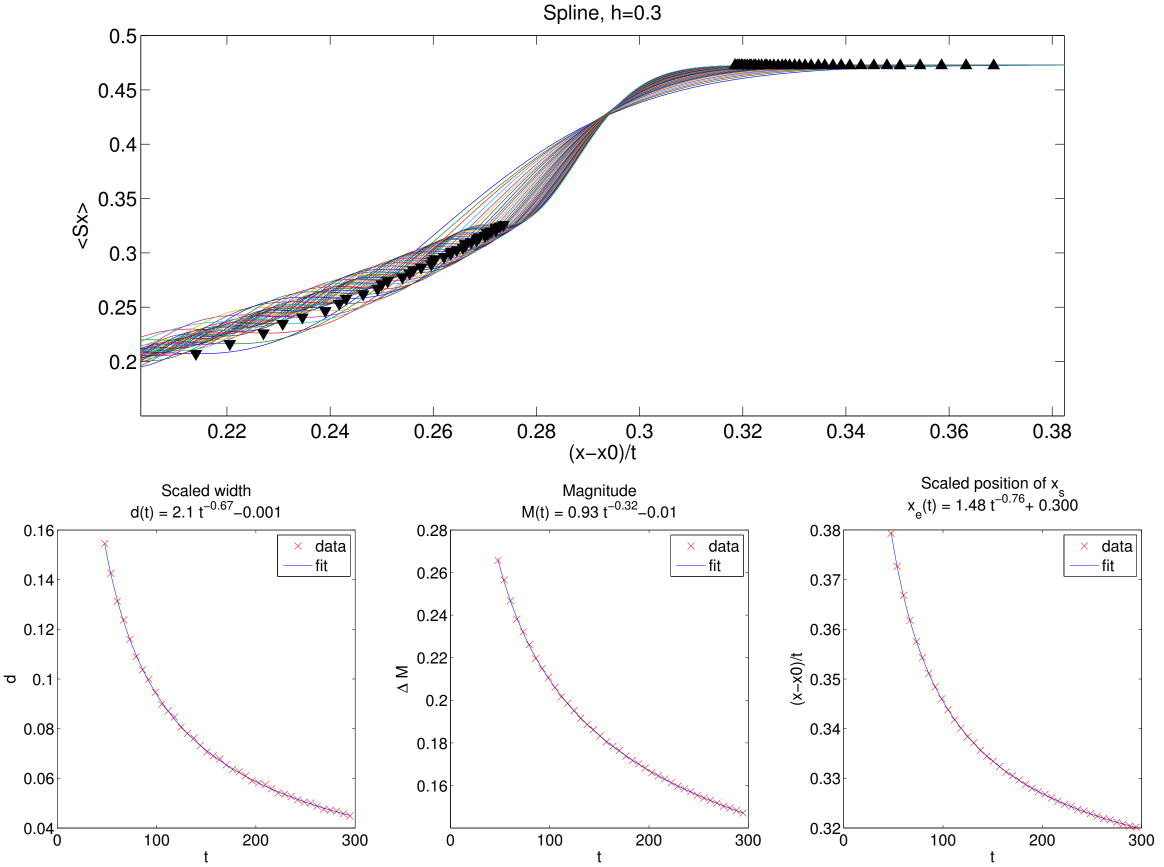

Figure 6.26.: Spline interpolations of the characteristic drop in magnetization for 25 time slices from $t = 50$ to $t = 300$ of a domain wall on the TIM at $h = 0.3$. The first local minima of magnetization after the initial drop in magnetization are taken to be the end point of the characteristic drop at different times, they are marked as lower triangles. The starting point at each time is taken to be the point where magnetization drops by a threshold amount $\epsilon = 10^{-3}$ below the value outside the light cone, they are marked as upper triangles. Notice, that for a right going signal front, the starting points are to the right of the end points. Again there is a value of magnetization $\langle \hat{S}^x \rangle \approx 0.42$, around which all magnetization profiles intersect. The scaled width, magnitude and scaled starting point of the drop over time can be seen in the bottom panel. They do not depend on time linearly, but seem to follow a power law. Fits to the model function $y(t) = at^{\alpha} + c$ indeed suggest convergence of all three quantities to constant values.

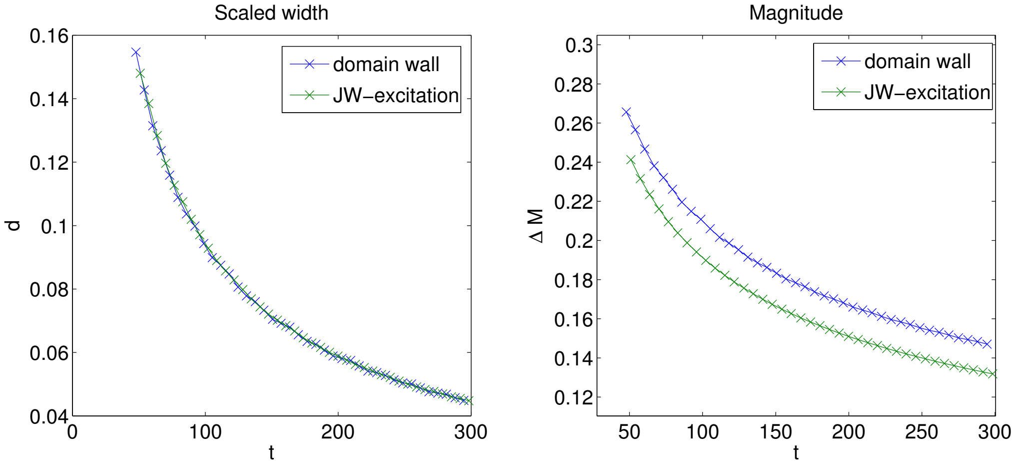

Figure 6.27.: Comparison of scaled width and magnitude over time of a single domain wall and a domain wall as part of a JW excitation on the TIM at $h = 0.3$. The scaled width for a JW excitation and a simple domain wall is basically the same at all time, whereas the magnitude of the drop is always higher for a simple domain wall. The cause for this slight difference must be the additional spin flip in z for the JW excitation.

7. Conclusion

The propagation of locally induced signals on infinite one-dimensional systems cannot be simulated by current methods of MPS time evolution. The Comoving Window (CMW) method has been introduced in Chapter 5 as an extension to MPS time evolution methods, which is able to achieve this task. The method has been formulated in terms of the canonical MPS representation, which is natural to the TEBD method (cf. Section 3.4). A generalization to other MPS language is straightforward.

It has been shown by application to various spin chain models, that this method is able to efficiently remove finite size effects present in simulations on finite systems. To begin with, the method has been tested by simulating the propagation of single spin flip signals on an XX spin chain of infinite size (cf. Section 6.1), where it has been shown, that the CMW is able to follow a signal's propagation front efficiently and thus enable simulations up to very large times with significantly reduced computational effort. The simulated data has been compared to exact results derived in Section 2.2 and shows very good agreement, also for large simulation times.

The CMW has then been tested on single and double spin flip signals propagating on an infinite size XXZ chain with ferromagnetic coupling. The shape and magnitude of the signal front has been studied up to very large simulation times. It has been found that for double spin flips the particle-particle interaction parameter J^z influences the evolution of the signal shape due to the emergence of slower bound state signals.

As a final successful test, the CMW has been used to follow three types of signals induced onto the thermodynamic limit ground state of the Transverse Ising model (TIM) (cf. Section 6.3). The ground state has been derived using infinite size DMRG (iDMRG) and has been properly canonized before initializing the CMW and inducing the signals. It has been shown that the CMW method is indeed able to also remove boundary effects that would clearly be present in a finite system simulation for this model. The scaling of the signal's shape with time has been investigated for all three signal types.

Simulations have also been attempted for signals induced onto the ground state of the antiferromagnetic XXZ chain of infinite size, which has again been derived by means of iDMRG and canonization. The CMW method however could not yield viable results, as perturbations are instantly generated at the window's boundaries and constantly propagate into the window, distorting the signal of interest. The failure of the method in this case is believed to arise from the degeneracy in Schmidt values of the ground state. Ways of addressing this problem that were attempted, but to no avail, are described in Chapter 6.2.3.

Overall, it has been shown that the CMW works well for simulating the propagation of signal fronts of locally induced signals on systems with finite correlation lengths, where signal fronts can be followed unperturbed up to very large simulation times. The method can also be used to follow slower parts of the signal or not move along with the signal front at all, where finite size effects are removed until the signal front hits the window boundaries, depending on the correlation length of the system.

Furthermore, as of now, the initial state must be non degenerate in Schmidt values for the method to succeed. An extension of the presented method towards this end is subject of current research, as well as the application to other models and initial conditions. What will the future hold? The answer to this question is, if anything, of course [42].

A. Addendum on MPS

A.1. Canonization of an iMPS

Consider a normed iMPS in canonical form (cf. Section 3.4), represented by the a 1-site unit cell $\{\Gamma, \lambda\}$ with MPS dimensions m, where the MPS matrices not necessarily fulfill the proper normalization conditions (3.49) and (3.50), i.e. the iMPS is not canonized.

Orús and Vidal have proposed a method to canonize an arbitrary, non-canonized iMPS, exploiting the gauge freedom of MPS matrices [43]. Another interpretation of this method in terms of mixed canonical MPS can be found in [30]. The following explanation closely follows [43], further details and proofs can be found therein.

The method relies on inserting the identity $\mathbb{1} = XX^{-1} = Y^{-1}Y$ for yet to be determined square matrices X and Y on the tensor network bonds between MPS matrices Γ and Schmidt values λ

$$\dots \lambda\Gamma\lambda\Gamma\lambda \dots = \dots \lambda X \underbrace{X^{-1}\Gamma Y^{-1}}_{:=\tilde{\Gamma}} \underbrace{Y\lambda X}_{:=\tilde{\lambda}} \underbrace{X^{-1}\Gamma Y^{-1}}_{:=\tilde{\Gamma}} Y\lambda \dots \tag{A.1}$$

such that the newly defined unit cell $\{\tilde{\Gamma}, \tilde{\lambda}\}$ is properly canonized. Since only identities were inserted, the new iMPS unit cell describes the same quantum state.

To determine X and Y, consider the transfer operators

$$R(Z) = \sum_{\sigma} (\Gamma^{\sigma}\lambda) Z (\Gamma^{\sigma}\lambda)^{\dagger} \tag{A.2}$$

$$L(Z) = \sum_{\sigma} (\lambda\Gamma^{\sigma})^{\dagger} Z (\lambda\Gamma^{\sigma}) \tag{A.3}$$

acting on $m \times m$ matrices Z. Notice, that for $Z = \mathbb{1}$ (A.2) and (A.3) correspond to the simple normalization conditions for the iMPS matrices, i.e. if the unit cell is properly canonized, both transfer operators have the unit matrix as their eigenmatrix with eigenvalue 1. This will in general however not be fulfilled for a non-canonized iMPS. To canonize a general iMPS, perform the following steps.

(1) Find the dominant eigenmatrices for both operators

$$R(V^r) = \eta^r V^r \qquad\qquad L(V^l) = \eta^l V^l, \tag{A.4}$$

where $\eta^l = \eta^r = 1$ if and only if the original iMPS was normed, i.e. find the transfer operators' fixed points. The eigenmatrices V^r and V^l will be real and hermitian.

(2) Decompose both eigenmatrices

$$V^r = XX^\dagger \qquad\qquad V^l = {Y^T}^\dagger Y^T \tag{A.5}$$

by means of an upper or lower Cholesky decomposition or an eigen decomposition.[1]

(3) Form and decompose via SVD

$$Y\lambda X \overset{SVD}{=} U\tilde{\lambda}V, \tag{A.6}$$

where $\tilde{\lambda}$ already corresponds to the new Schmidt values for the canonized unit cell.

(4) To construct the remaining MPS matrix $\tilde{\Gamma}$, combine the remaining matrices to get

$$\tilde{\Gamma} = VX^{-1}\Gamma Y^{-1}U. \tag{A.7}$$

Inserting the new unit cell $\{\tilde{\Gamma}, \tilde{\lambda}\}$ into the normalization conditions (3.49) and (3.50) indeed shows, that it is now canonized.

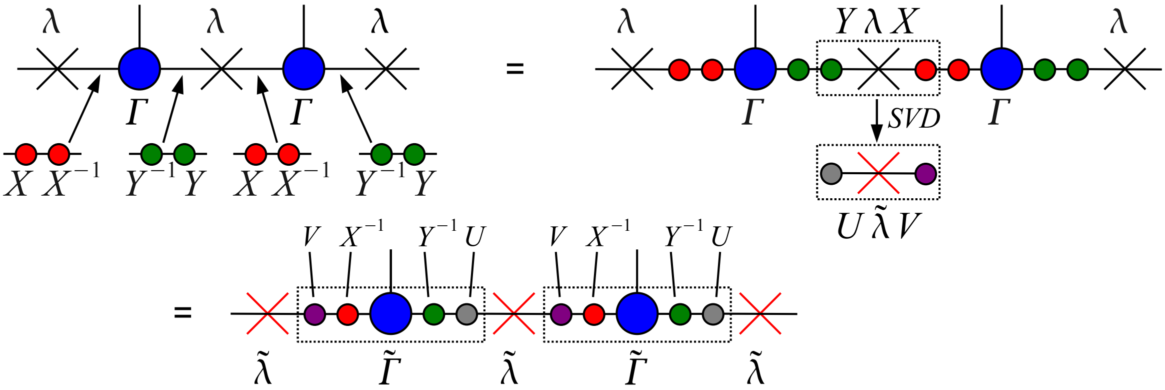

Figure A.1.: Canonization of an iMPS. Insert the identities $\mathbb{1} = XX^{-1}$ and $\mathbb{1} = Y^{-1}Y$ between the MPS-matrices and the Schmidt values. Derive X and Y from (A.5). Combine and apply SVD to get $Y\lambda X = U\tilde{\lambda}V$. Combine U and V with the remaining tensors to get $\tilde{\Gamma} = VX^{-1}\Gamma Y^{-1}U$.

Special attention has to be paid if the resulting iMPS is required to be normed. Due to the nature of the eigen decomposition, the left and right eigenmatrices of the transfer operators can be multiplied with an arbitrary number without changing anything for the normalization conditions. However, after decomposing $M = Y\lambda X = U\tilde{\lambda}V$, the Schmidt values $\tilde{\lambda}$ must fulfill $\sum_\alpha \tilde{\lambda}_\alpha^2 = 1$ for the resulting iMPS to be normed. This can be

---

[1] Even though Orús and Vidal [43] and also McCulloch [30] recommend an eigen decomposition, we have found that a Cholesky decompositions yields numerically more stable results, if the MPS matrices are already close to being canonized, i.e. the eigenmatrices of the transfer operators are not far from being diagonal.

ensured, by calculating the matrix norm $w = \|M\| = \mathrm{Tr}\left(M^\dagger M\right)$ and replacing $U \to \frac{U}{\sqrt{w}}$ and $V \to \frac{V}{\sqrt{w}}$, which automatically norms the resulting $\tilde{\lambda}$ to 1.

The above procedure canonizes a 1-site unit cell iMPS. To canonize a 2-site unit cell $\{\Gamma^A, \lambda^{(A)}, \Gamma^B, \lambda^{(B)}\}$, one can slightly modify the above procedure by coarse graining the 2-site unit cell first to give an initial pair $\{\Gamma, \lambda\}$

$$\Gamma = \Gamma^A \lambda^{(A)} \Gamma^B \qquad\qquad \lambda = \lambda^{(B)}, \tag{A.8}$$

so that $\Gamma^A\lambda^{(A)}\Gamma^B\lambda^{(B)} = \Gamma\lambda$. Notice that the coarse grained Γ has now physical dimension d^2, with d the Hilbert space dimension for one site. Now use the above procedure to get a canonized pair $\{\tilde{\Gamma}, \tilde{\lambda}\}$. We can instantly identify $\tilde{\lambda}^{(B)} = \tilde{\lambda}$, but to extract the remaining updated elements of the unit cell we need to combine $\tilde{\Gamma}$ with $\tilde{\lambda}$ and decompose

$$\tilde{\lambda}\tilde{\Gamma}\tilde{\lambda} \overset{SVD}{=} A\tilde{\lambda}^{(A)}B. \tag{A.9}$$

Notice that the decomposed matrix $\tilde{\lambda}\tilde{\Gamma}\tilde{\lambda}$ has the form of a 2-site wave function. Thus we can extract the now canonized $\tilde{\lambda}^{(A)}$ immediately, the canonized MPS-matrices can be extracted as usual

$$\tilde{\Gamma}^A = \tilde{\lambda}^{-1}A \qquad\qquad \tilde{\Gamma}^B = B\tilde{\lambda}^{-1}. \tag{A.10}$$

The 2-site unit cell is now properly canonized and fulfills the normalization conditions for canonized MPS-matrices over *two sites*, i.e. the unit matrix is the eigenmatrix for the extended transfer operators over two sites

$$R_2(Z) = \sum_{\sigma_A\sigma_B} \Gamma^{\sigma_A}\lambda^{(A)}\Gamma^{\sigma_B}\lambda^{(B)} Z (\Gamma^{\sigma_A}\lambda^{(A)}\Gamma^{\sigma_B}\lambda^{(B)})^\dagger \tag{A.11}$$

$$L_2(Z) = \sum_{\sigma_A\sigma_B} (\lambda^{(B)}\Gamma^{\sigma_A}\lambda^{(A)}\Gamma^{\sigma_B})^\dagger Z \lambda^{(B)}\Gamma^{\sigma_A}\lambda^{(A)}\Gamma^{\sigma_B}. \tag{A.12}$$

The extraction of $\tilde{\Gamma^A}$ and $\tilde{\Gamma^B}$ by SVD ensures the proper canonization of both MPS-matrices in the usual 1-site way.

When using 2-site unit cells, this procedure is required, so that the left and right end of the unit cell is in the same gauge and one can freely arrange the unit cell in an arbitrary repetition, e.g. to initialize an L-site CMW or to use it as an initial state for real or imaginary time evolution using iTEBD.

A.2. Inducing Local Signals on MPS

In this section we will shortly derive how to induce a local signal on a general MPS by applying one or more unitary operators onto it. As shown in [2], the application of a unitary 1-site operator onto an MPS only involves updating the MPS matrix of the corresponding site.

Since all simulated signals are induced by spin operators, we will derive how to apply single site spin operators such as $\hat{S}^x_j$ and $\hat{S}^z_j$ onto a finite size MPS. Spin operators are used in their z basis representation as $\hat{S}^\alpha = \frac{1}{2}\sigma^\alpha$, with σ^α the Pauli matrices in (2.6). We will also use the spin ladder operators $\hat{S}^\pm = \hat{S}^x \pm i\hat{S}^y$ in the z basis

$$S^+ = \begin{pmatrix} 0 & 1 \\ 0 & 0 \end{pmatrix}, \qquad S^- = \begin{pmatrix} 0 & 0 \\ 1 & 0 \end{pmatrix}. \tag{A.13}$$

The inverse transformation is then

$$\hat{S}^x = \frac{1}{2}\left(\hat{S}^+ + \hat{S}^-\right) \qquad \hat{S}^y = \frac{1}{2i}\left(\hat{S}^+ - \hat{S}^-\right). \tag{A.14}$$

As can be seen, S^x corresponds to a spin flip in z. Conversely, S^z acts as a spin flip in x.

Using $\hat{S}^\alpha_j = \sum_{\sigma_j\sigma'_j} S_j^{\alpha,\sigma_j\sigma'_j} |\sigma_j\rangle\langle\sigma'_j|$ with $\alpha = \{x, y, z\}$ one gets

$$\hat{S}^\alpha_j |\psi\rangle = \sum_{\{\sigma\}} \Gamma^{\sigma_1} \ldots \lambda^{(j-1)} \underbrace{\Big(\sum_{\sigma'_j} S_j^{\alpha,\sigma_j\sigma'_j} \Gamma^{\sigma'_j}\Big)}_{:=\tilde{\Gamma}^{\sigma_j}} \lambda^{(j)} \ldots \Gamma^{\sigma_L} |\sigma_1 \ldots \sigma_L\rangle, \tag{A.15}$$

where $\tilde{\Gamma}^{\sigma_j}$ is still properly normalized. The state itself however, is in general not normed anymore.

A special case of induced signals are spin flips, as they also preserve the state norm. Using (A.14) we can write

$$\hat{F}^z := \hat{S}^+ + \hat{S}^- = 2\hat{S}^x \tag{A.16}$$

for the spin flip operator along z on site j. Together with (A.15) we then get for the updated MPS matrix after applying $\hat{F}^z$ to a general MPS

$$\tilde{\Gamma}^{\sigma_j} = \Gamma^{-\sigma_j}, \tag{A.17}$$

i.e. $\Gamma^{\uparrow_j}$ and $\Gamma^{\downarrow_j}$ have now switched places. Similarly, the spin flip operator in x on site j can then be written as

$$\hat{F}^x_j := 2\hat{S}^z_j \tag{A.18}$$

and we get for the updated MPS-matrix

$$\tilde{\Gamma}^{\sigma_j} = \sigma_j \Gamma^{\sigma_j}. \tag{A.19}$$

Another special case is a Jordan-Wigner excitation (cf. Section 2.1), which is essentially a combination of several spin flips. Similar to a spin flip we will define a Jordan-Wigner excitation on site j as

$$\hat{F}^{JW}_j := c_j + c_j^\dagger \overset{(2.2)}{=} \prod_{n<j}\left(-2\hat{S}^z_n\right)\left(\hat{S}^+_j + \hat{S}^-_j\right) = \prod_{n<j}\left(-\hat{F}^x_n\right)\hat{F}^z_j. \tag{A.20}$$

This excitation corresponds to a single spin flip in z on site j and spin flips in x on all sites left of site j, inducing a domain wall.

Acknowledgments

The creation of a master thesis, including many stages of learning and understanding, motivation and the joy of success, but also frustration and perplexity, is a formidable task often challenging and straining but at the same time an excellent chance to grasp deeper knowledge about a special topic of interest. During this process I have had the blessing of outstanding and caring support on so many levels, without which the present work would not have been possible.

First of all I would like to express my gratitude towards my supervisor, Dr. Hans Gerd Evertz, who has been ever caring, patient and supportive, guiding me towards the goal at times when I could not see it. He has always had time for inspiring discussions and fruitful input and has been a great supervisor.

A substantial part of the knowledge gained during the creation of this master thesis is also due to the caring support of Dr. Tomotoshi Nishino at the Department of Physics, Graduate School of Sciences, University of Kobe/Japan, where I had the privilege of a research stay for 5 months in early 2010. Dr. Nishino has not only helped me a lot towards understanding the principles of numerical simulations and the foundations of MPS based algorithms, but has also made my stay in Kobe an experience of dear memory. In this context I would also like to thank all members and students of the Department of Physics of Kobe University for the warm reception, their friendship and utmost patience with my Japanese skills.

I would also like to thank all my colleagues and friends, from Austria or abroad, for long fruitful discussions and advice, great support and friendship, but also for relieving distractions here and there. I would like to give special thanks to Martin Ganahl, who provided essential and crucial insights and has always been a formidable partner in discussions as well as a great office neighbor. I would also like to thank Andreas Hirczy, who has often helped me with computational and programming issues, as well as all the other – also former – members of the Institute of Theoretical Physics for the enjoyable working atmosphere.

I am also very grateful to my parents, Regina and Hans Peter, my sisters Agnes and Dorothea and my brother Maximilian, as well as to the rest of my family, who have always been most supportive and encouraging through all these years. And of course, I would like to thank Mirjam for her warm and supportive love, her patience and for always being there for me.

Bibliography

[1] S. R. White, Phys. Rev. Lett. **69**, 2863 (1992); S. R. White, Phys. Rev. B **48**, 10345 (1993).

[2] G. Vidal, Phys. Rev. Lett. **91**, 147902 (2003); G. Vidal, Phys. Rev. Lett. **93**, 040502 (2004).

[3] S. R. White and A. E. Feiguin, Phys. Rev. Lett. **93**, 076401 (2004); A. J. Daley, C. Kollath, U. Schollwöck, and G. Vidal, J. Stat. Mech. **2004**, P04005 (2004).

[4] S. Östlund and S. Rommer, Phys. Rev. Lett. **75**, 3537 (1995); S. Rommer and S. Östlund, Phys. Rev. B **55**, 2164 (1997).

[5] I. Bloch, J. Dalibard, and W. Zwerger, Rev. Mod. Phys. **80**, 885 (2008).

[6] S. Fölling, S. Trotzky, P. Cheinet, M. Feld, R. Saers, A. Widera, T. Müller, and I. Bloch, Nature **448**, 1029 (2007).

[7] I. Žutić, J. Fabian, and S. Das Sarma, Rev. Mod. Phys. **76**, 323 (2004).

[8] P. Jordan and E. Wigner, Zeitschrift für Physik **47**, 631 (1928).

[9] E. Lieb, T. Schultz, and D. Mattis, Ann. Phys. **16**, 407 (1961).

[10] B. K. Chakrabarti, A. Dutta, and P. Sen, *Quantum Ising Phases and Transitions in Transverse Ising Models* (Springer, 1996), ISBN 3-540-61033-2.

[11] S. Sachdev, *Quantum Phase Transitions* (Cambridge, 1999), ISBN 0-521-58254-7.

[12] L. Amico, A. Osterloh, F. Plastina, R. Fazio, and G. Massimo Palma, Phys. Rev. A **69**, 022304 (2004).

[13] P. G. de Gennes, Solid State Comm. **1**, 132 (1963).

[14] R. Blinc, J. Phys. Chem. Solids **13**, 204 (1960).

[15] P. W. Anderson, Phys. Rev. **112**, 1900 (1958).

[16] P. Pfeuty, Ann. Phys. **57**, 79 (1970).

[17] W. Heisenberg, Zeitschrift für Physik **38**, 411 (1926); P. A. M. Dirac, Proc. R. Soc. Lond. A **112**, 661 (1926).

[18] A. Auerbach, *Interacting Electrons and Quantum Magnetism* (Springer, 1994), ISBN 0-387-94286-6.

[19] B. Sutherland, *Beautiful Models* (World Scientific, 2004), ISBN 981-238-897-4.

[20] H. Bethe, Zeitschrift für Physik **71**, 205 (1931).

[21] M. Karbach and G. Müller, Computers in Physics **11**, 36 (1997), arXiv:cond-mat/9809162; M. Karbach, K. Hu, and G. Müller, Computers in Physics **12**, 565 (1998), arXiv:cond-mat/9809163.

[22] F. Verstraete and J. I. Cirac, arXiv:cond-mat/0407066 (2004).

[23] F. Verstraete and J. I. Cirac, Phys. Rev. Lett. **104**, 190405 (2010).

[24] T. Nishino, J. Phys. Soc. Jpn. **64**, 3598 (1995); T. Nishino and K. Okunishi, J. Phys. Soc. Jpn. **65**, 891 (1996).

[25] U. Schollwöck, Rev. Mod. Phys. **77**, 259 (2005); U. Schollwoeck, Ann. Phys. **326**, 96 (2011).

[26] I. Affleck, T. Kennedy, E. H. Lieb, and H. Tasaki, Phys. Rev. Lett. **59**, 799 (1987).

[27] K. G. Wilson, Rev. Mod. Phys. **47**, 773 (1975); K. G. Wilson, Rev. Mod. Phys. **55**, 583 (1983).

[28] P. W. Anderson, Phys. Rev. **124**, 41 (1961).

[29] R. Bulla, T. A. Costi, and T. Pruschke, Rev. Mod. Phys. **80**, 395 (2008); H. R. Krishna-Murthy, J. W. Wilkins, and K. G. Wilson, Phys. Rev. B **21**, 1003 (1980).

[30] I. P. McCulloch, arXiv:0804.2509 (2008).

[31] T. Nishino and K. Okunishi, J. Phys. Soc. Jpn. **64**, 4084 (1995).

[32] R. Jozsa, J. of Modern Optics **41**, 2315 (1994).

[33] S. R. White, Phys. Rev. Lett. **77**, 3633 (1996).

[34] M. A. Cazalilla and J. B. Marston, Phys. Rev. Lett. **88** (2002).

[35] M. Suzuki, Phys. Lett. A **146**, 319 (1990).

[36] M. B. Hastings, J. Math. Phys. **50**, 095207 (2009).

[37] G. Vidal, Phys. Rev. Lett. **98**, 070201 (2007).

[38] E. H. Lieb and D. W. Robinson, Comm. Math. Phys. **28**, 251 (1972).

[39] S. Bravyi, M. B. Hastings, and F. Verstraete, Phys. Rev. Lett. **97**, 050401 (2006).

[40] M. J. Ganahl, Master's thesis, Graz University of Technology (2010).

[41] M. J. Ganahl, E. Rabel, F. Essler, and H. G. Evertz, in preparation.

[42] D. Adams, *The The Hitch Hiker's Guide to the Galaxy: A Trilogy in Five Parts* (William Heinemann, 1995), ISBN 978-0434003488.

[43] R. Orús and G. Vidal, Phys. Rev. B **78**, 155117 (2008).